nature biotechnology

Article

https://doi.org/10.1038/s41587-024-02431-9

One-step nanoscale expansion microscopy reveals individual protein shapes

Received: 21 December 2023

Accepted: 13 September 2024

Published online: 09 October 2024

Check for updates

Ali H. Shaib[1] ✉, Abed Alrahman Chouaib[2], Rajdeep Chowdhury[1,3], Jonas Altendorf[1], Daniel Mihaylov[4], Chi Zhang[5,6,7,8,9,10], Donatus Krah[1], Vanessa Imani[1], Russell K. W. Spencer[11], Svilen Veselinov Georgiev[1], Nikolaos Mougios[1,12], Mehar Monga[13], Sofiia Reshetniak[1], Tiago Mimoso[14], Han Chen[15], Parisa Fatehbasharzad[1], Dagmar Crzan[1], Kim-Ann Saal[1], Mohamad Mahdi Alawieh[1], Nadia Alawar[2], Janna Eilts[16], Jinyoung Kang[5,6,7,8,9,10], Alireza Soleimani[11], Marcus Müller[11], Constantin Pape[17], Luis Alvarez[18], Claudia Trenkwalder[19,20], Brit Mollenhauer[20,21], Tiago F. Outeiro[22,23,24,25], Sarah Köster[14,26], Julia Preobraschenski[13,26], Ute Becherer[2], Tobias Moser[13,26,27], Edward S. Boyden[5,6,7,8,9,10], A. Radu Aricescu[4], Markus Sauer[16], Felipe Opazo[1,12,28] & Silvio O. Rizzoli[1,12,26] ✉

The attainable resolution of fluorescence microscopy has reached the subnanometer range, but this technique still fails to image the morphology of single proteins or small molecular complexes. Here, we expand the specimens at least tenfold, label them with conventional fluorophores and image them with conventional light microscopes, acquiring videos in which we analyze fluorescence fluctuations. One-step nanoscale expansion (ONE) microscopy enables the visualization of the shapes of individual membrane and soluble proteins, achieving around 1-nm resolution. We show that conformational changes are readily observable, such as those undergone by the ~17-kDa protein calmodulin upon Ca^{2+} binding. ONE is also applied to clinical samples, analyzing the morphology of protein aggregates in cerebrospinal fluid from persons with Parkinson disease, potentially aiding disease diagnosis. This technology bridges the gap between high-resolution structural biology techniques and light microscopy, providing new avenues for discoveries in biology and medicine.

Several recent studies have improved the localization precision of fluorescence microscopy to the 1-nm range or even below this value[1–4]. Nevertheless, the application of such techniques to biological samples has been limited by two fundamental problems. First, the achievable structural resolution depends on the labeling density because fluorescent proteins or chemical fluorophores cannot be packed closer than their molecular size (typically 1 nm or larger[5]) allows. This could be alleviated by having only one functional fluorophore physically present at one time point at the respective location[3,4]. Second, fluorophores can interact through energy transfer at distances below 10 nm, resulting in accelerated photoswitching (blinking) and photobleaching and, thus, in lower localization probabilities[6].

A simple solution would be to separate the labeling sites by the physical expansion of the specimen, in what is termed expansion microscopy (ExM)[7]. In addition, the samples can be labeled fluorescently after expansion, at a time point at which the fluorophore size becomes negligible and, therefore, no longer hinders the labeling density, while lowering the displacement error. To then reach molecular-scale imaging, one would combine ExM with optics-based super-resolution. This has been attempted numerous times[8–10] but

A full list of affiliations appears at the end of the paper. ✉e-mail: ali.shaib@med.uni-goettingen.de; srizzol@gwdg.de

the resulting performance typically reached only ~10 nm. ExM gels are dim because the fluorophores are diluted by the third power of the expansion factor, thus limiting optics techniques that prefer bright samples, such as stimulated emission depletion (STED), or saturated structured illumination. In addition, ExM gels need to be imaged in distilled water because the ions in buffered solutions shield the charged moieties of the gels and diminish the expansion factor. The use of distilled water reduces the performance of techniques that rely on special buffers, such as single-molecule localization microscopy[7]. A third class of optical super-resolution approaches is based on determining the higher-order statistical analysis of temporal fluctuations measured in a video, using algorithms applied to these images to generate super-resolution images, such as super-resolution optical fluctuation imaging (SOFI)[11] or super-resolution radial fluctuations (SRRF)[12,13]. The resolution of these approaches is inversely correlated to the distance between the fluorophores[12–14] and they do not require especially bright samples or special buffers, implying that they should benefit from ExM. To test this hypothesis, we combined X10 ExM[15,16] with SRRF[12–14] and established a technique we term one-step nanoscale expansion (ONE) microscopy (Fig. 1a,b). Using this technique, we aim to reveal the shape of single proteins of different sizes with near 1-nm resolution.

Results

Principles and validation of ONE microscopy

We first attached a gel-compatible anchor (Acryloyl-X) to protein molecules, either purified or in a cellular context, and then embedded these samples into a swellable X10 gel[15,16]. Proteins were hydrolyzed (homogenized) by proteinase K or by heating in alkaline buffers, leading to main-chain breaks. This enables a highly isotropic tenfold expansion of the sample, which is achieved by distilled water incubations[15,16]. We then imaged the samples using wide-field epifluorescence or confocal microscopy, acquiring series of hundreds to thousands of images as videos (ideally 1,500–2,000) in which the fluorescence intensity of the fluorophores fluctuates (Fig. 1b and Supplementary Fig. 1). Each pixel of a frame was then magnified into a large number of subpixels and the local radial symmetries of the frame (which are because of the radial symmetry of the microscope's point spread function (PSF)) were measured. This parameter, termed 'radiality' was analyzed throughout the image stack, by higher-order temporal statistics, to provide the final, fully resolved image[12–14]. To aid in the implementation of this procedure, we generated an ONE software platform as a plugin for the popular freeware ImageJ (Fiji) (Supplementary Fig. 2 and Supplementary Software).

In theory, the precision of the SRRF technique should reach values close to 10 nm (ref. 12). SRRF should, therefore, be able to separate fluorophores found at 20 nm from each other, provided the signal-to-noise ratio (SNR) is sufficiently high. We found this to be the case, using nanorulers (provided by GATTAquant[17]) of precisely defined size (Supplementary Figs. 4 and 5).

In practice, most previous implementations of SRRF have reached ~50–70 nm. This is partly because of the fact that the presence of overlapping fluorophores reduces radiality in conventional samples[12,13] and partly because of the aims of the respective SRRF implementations, which did not target ultimate performance in terms of resolution and, therefore, did not optimize a number of parameters. First, the highest resolutions are obtained by analyzing higher-order statistical correlations, whose precision is dependent on the number of frames acquired, as discussed not only for SRRF but also for SOFI[11]. While most publications used less than 300 frames, we found that results were optimal when using 1,500–2,000 frames (Supplementary Fig. 5). Working with low frame numbers reduces the achievable resolution, even when working with ExM gels[18,19]. Second, the SNR needs to be optimized carefully (Supplementary Fig. 6).

These limitations are alleviated by ExM (see Supplementary Discussion for more details). As the distance between the fluorophores increases, it enables the study of intensity fluctuations from individual dye molecules independently. The SNR also increases even for idealized samples consisting only of fluorescently conjugated nanobodies (Nbs) in solution (Supplementary Fig. 3a,b). This approach should, therefore, allow an optimal SRRF performance, which, divided by the expansion factor, should bring the resulting imaging precision to the molecular scale, as long as the gel expands isotropically in all dimensions. The X10 gel, based on *N,N*-dimethylacrylamide acid (DMAA), rather than the acrylamide used in typical ExM protocols, has a more homogeneous distribution of crosslinks[20], thus leading to fewer errors in expansion (a further discussion on gel homogeneity was provided in a previous study[21]). However, the use of gels with large expansion factors is prone to inducing imaging drift, which was only eliminated after we introduced specially designed imaging chambers (Supplementary Fig. 7). For correcting residual drifts, the ONE plugin automatically applies drift correction before computation (Supplementary Fig. 8). Drift compensation is explained in more detail in the Supplementary Information.

ONE microscopy reveals protein shapes

To reveal protein molecules, we labeled their peptide chains using *N*-hydroxysuccinimide ester (NHS-ester) fluorescein[22,23], which maintains a signal intensity of ~50% by the end of the video acquisition, under our imaging conditions, for this type of experiment (Supplementary Fig. 3c,d). This is possible because proteins are broken during homogenization at multiple main-chain positions and each resulting peptide has an exposed amino-terminal group that can be efficiently conjugated with NHS-ester-functionalized fluorophores. For an initial visualization, we applied this labeling method to a membrane protein, the full-length β3 human γ-aminobutyric acid receptor ($GABA_AR$) homopentamer, a ligand-gated chloride channel[24]. We analyzed purified receptors in solution and produced images that resembled 'front' and 'side' views of the receptor, similar to its structure, as derived from crystallography and single-particle cryogenic electron microscopy (cryo-EM) structures (Fig. 1b,c and Supplementary Fig. 9). It is worth noting that the particles observed by ONE microscopy are indeed single molecules and no averaging or classification was performed on these datasets.

We next applied this approach to antibody molecules and we could observe immediately recognizable outlines for immunoglobulins (IgGs, IgAs and IgMs) (Fig. 2a and Supplementary Fig. 10). Fluorescent labels attached to secondary IgG antibodies could also be observed in the same images (Fig. 2a) and in complexes between fluorescently conjugated primary and secondary antibodies or Nbs (Supplementary Fig. 10b).

We next investigated a protein of unknown structure, the ~225-kDa otoferlin, a Ca^{2+} sensor molecule that is essential for synaptic sound encoding[25]. The outlines provided by ONE microscopy imaging strongly resemble the AlphaFold[26] prediction for this protein (Fig. 2b and Supplementary Fig. 11). At the opposite end of the Ca^{2+} sensor size spectrum, we sought to visualize the small (~17 kDa) protein calmodulin, expressed as a green fluorescent protein (GFP) chimera. GFP itself was visualized as a small and compact structure, as expected (Fig. 2c and Supplementary Fig. 12). Calmodulin–GFP exhibited an elongated shape, as expected from its known structure (Fig. 2d). To our surprise, even for such small particles, it was possible to observe changes in their shape upon Ca^{2+} binding (Fig. 2d). We applied both heat denaturation and proteinase K treatments for the homogenization of calmodulin, to test whether these methods would lead to different results. The proteinase K presumably removes most of the amino acids that are not anchored into the gel and is, therefore, more aggressive than the heat denaturation[27]. However, both methods resulted in similar observations for calmodulin, implying that both can be used for observing the shape of purified proteins (Fig. 2d and Supplementary Fig. 13).

To validate our procedures, we proceeded to test the organization of a number of samples that were analyzed in the past using methods

https://doi.org/10.1038/s41587-024-02431-9

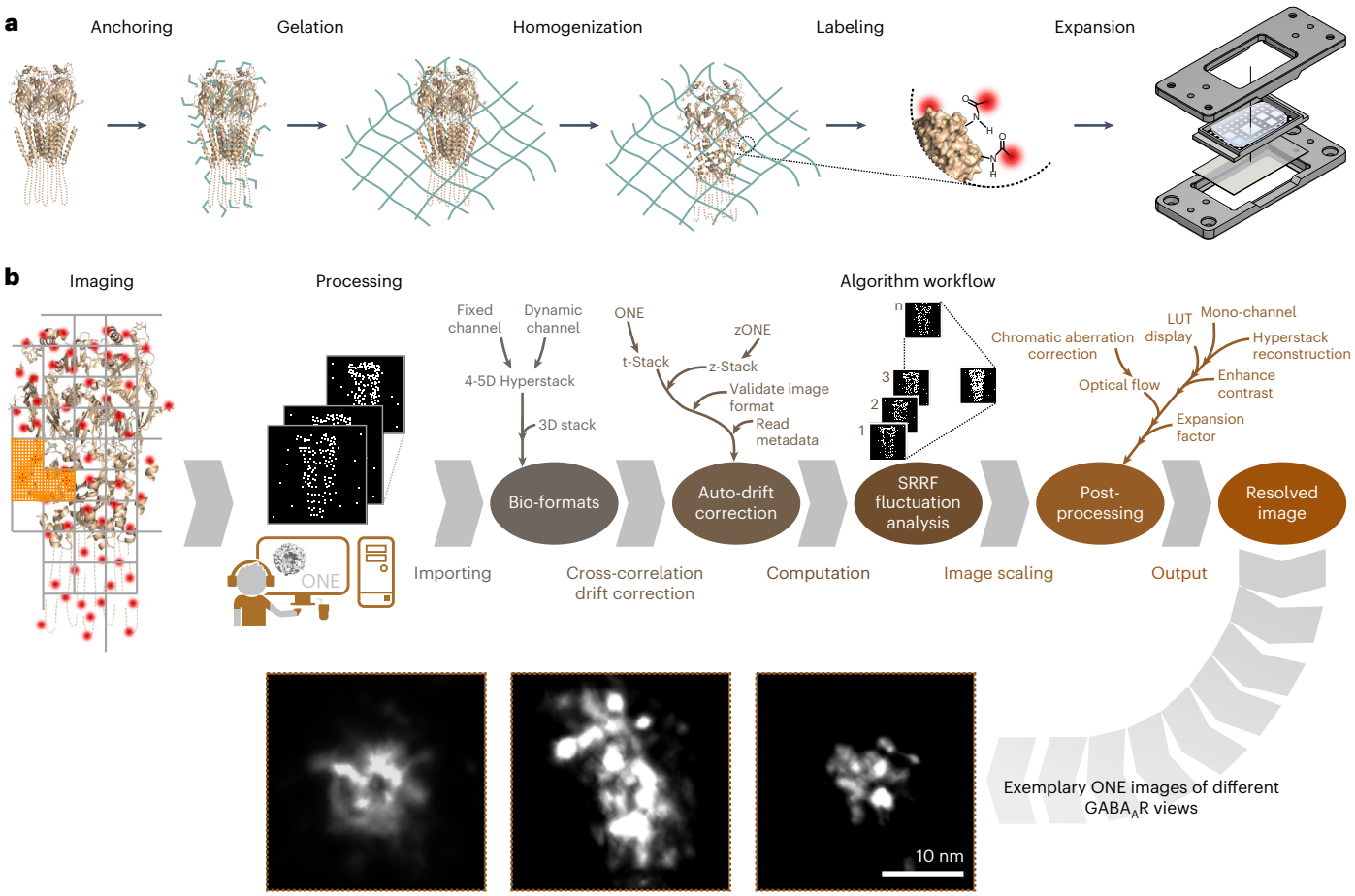

Fig. 1 | ONE microscopy concept. a, Biological samples are linked to gel anchors, relying on Acryloyl-X, followed by X10 gel formation and homogenization, which is achieved either by proteinase K digestion or by proteolysis induced by autoclaving in alkaline buffers. Full expansion is achieved by repeated washes with distilled H_2O and is followed by mounting gel portions in a specially designed chamber. **b**, Expansion separates the fluorophores spatially, allowing them to fluctuate independently[6]. Repeated imaging is performed (up to 3,000 images) in any desired imaging system (confocal, epifluorescence, etc.) to detect signal fluctuations, which are then computed through an open-source JAVA plugin (ONE platform) based on the SRRF algorithm, before assembling the final super-resolved exemplary images (here, GABA$_A$Rs). The analysis routine is explained in Supplementary Fig. 1 and a flowchart of the software implementation is shown in Supplementary Fig. 2. Further details on image acquisition and image processing can be found in the Methods. **c**, Superimposition of ONE microscopy images and cryo-EM data. A cartoon view of a complex consisting of a GABA$_A$R bound simultaneously by five Nbs (GABA$_A$R–Nb, PDB 5OJM). The red dots represent the two fluorophores on each Nb. The four cryo-EM images are representative 2D classes of the GABA$_A$R–Nb complexes, derived from the same samples as used for ExM. The overview panel shows an exemplary ONE image (from a total 648 ONE images, acquired from at least six gels) of GABA$_A$R–Nb that are postexpansion labeled with NHS-ester dyes described in Supplementary Fig. 3, followed by a magnified region of a single receptor. The last panel shows a cryo-EM–ONE overlay.

with very high resolution, such as MINFLUX. As shown in Supplementary Fig. 14, ONE microscopy could reproduce the expected signal patterns on isolated Nbs in vitro (Supplementary Fig. 14a–e). Moreover, the signals observed by immunostaining cultured neurons with a postsynaptic density protein 95 (PSD95) Nb (initially indicated in a previous study[28]) are very similar to results obtained more recently by MINFLUX microscopy[29] (Supplementary Fig. 14f). Lastly, microtubule images were also similar to their MINFLUX counterparts (Supplementary Fig. 14g).

For additional validation purposes, we evaluated a purified ALFA-tagged enhanced GFP (EGFP) construct bound simultaneously by two anti-GFP Nbs[30] and by an anti-ALFA Nb[31]. This results in a triangular semiflexible arrangement, which we termed a 'triangulate smart ruler' (TSR; Supplementary Fig. 15a–c). The TSR aspect observed in

ONE microscopy was consistent with crystal structures of Nb–EGFP and Nb–ALFA complexes (Supplementary Fig. 15d,e). The fluorophore positions on the individual Nbs were also consistent with their known size (Supplementary Fig. 16a,e). However, Nbs are 4–5 nm in length, implying that the fluorophores they carry are separated by relatively large distances. To test the performance of ONE microscopy on smaller structures, we turned to a polypeptide consisting of nine amino acids, termed membrane-binding fluorophore-cysteine-lysine-palmitoyl group (mCLING)[32]. mCLING contains seven lysines, thereby offering many anchor points for ExM, and can also carry on its C-terminal cysteine residue an additional Atto 647N moiety, resulting in a total molecular weight of 2,056 Da (Supplementary Fig. 17a). The whole length of mCLING is ~3 nm (according to our simulations; Supplementary Fig. 17d) and its expansion should place fluorophores at subnanometer distances. As expected, we indeed observed fluorophores separated by ~1 nm or below (Supplementary Fig. 17e–g).

We also sought to verify whether such analyses could be performed using a natural system rather than purified proteins. To test this, we turned to cell cultures subjected to detergent extraction during fixation. This procedure results in the preservation of actin filaments at the cell–glass interface, which could then be analyzed in ONE microscopy. We performed a simple manual averaging analysis on ~50 filaments and we obtained images that reproduce the known size of the actin filaments and the distance between the actin subunits, as well as providing views of the filament pitch (Supplementary Fig. 18).

Three-dimensional (3D) analysis of ONE images validates our imaging precision

The ability of ONE microscopy to reveal images of individual molecules opens a strong possibility of user bias. Users are naturally impressed by images showcasing the expected protein shapes, implying that such images would tend to be over-reported (akin to the 'Einstein from noise' problem known in single-particle cryo-EM[33]). Such bias is difficult to quantify and affects our understanding of the precision of the ONE technology. In principle, most ONE images may suffer from various degrees of distortion, from uneven expansion to inhomogeneous labeling, which a user-biased qualitative analysis would fail to report.

To address this, one could image the size and organization of known molecular structures, such as the nuclear pore complex (NPC; as performed in several recent studies, including our characterization of the X10 gels[27]), which would serve as molecular rulers to validate the ONE procedure. However, the NPC size (>100 nm) is far too large for ONE microscopy and we, therefore, applied this procedure on smaller molecules or assemblies, whose size is known or can be estimated from structural biology techniques, including Nbs, GFP, actin, $GABA_A$Rs, otoferlin, IgG, IgA and IgM (Supplementary Fig. 19). As presented in Supplementary Fig. 19, all measured parameters were very similar to the expected values and their variance was limited, suggesting that the expansion and labeling have isotropic, homogeneous performance.

While this approach has been sufficient for validating most super-resolution fluorescence microscopy tools in the past, we would like to point out that structure measurements do not constitute a complete solution to the issue of user bias because the particles measured are still selected by humans. In principle, one could turn to automated techniques of measuring image resolution, such as the Fourier ring correlation (FRC) determination[34]. We applied this approach to our images, relying on the NanoJ-SQUIRREL package[34] with a blockwise implementation, to provide FRC values for different regions within individual images (Supplementary Fig. 20). We obtained values within the low single-digit nanometer range and below 1 nm when suitably small pixels were used. This is in line with our ability to measure distances as low as 0.5 nm within single molecules (Supplementary Fig. 21). However, this remains only a partial solution to the bias issue because only the resolution and not the accuracy of fluorophore placement (that is, the degree of distortion) is measured.

We, therefore, turned to a completely automated analysis, in which the 3D shape of individual proteins is derived from the ONE images. To overcome human bias, ONE images were segmented using an automatic thresholding procedure (based solely on particle intensity) to identify hypothetical molecules. These were processed by deconvolution and normalization steps (Methods) and transferred to cryoFIRE, an unsupervised ab initio autoencoder for complex shape reconstruction with amortized inference[35], which was modified to accommodate fluorescence rather than cryo-EM signals. Importantly, the cryoFIRE algorithm does not place any bias on the expected molecular shape because there is no user input and no correlation to expected structures. The overall approach is illustrated in Supplementary Fig. 22a.

We first applied this procedure to the simple case of an Nb carrying two fluorophores (Fig. 3a). The deep learning analysis of 279 protein molecules resulted in the expected visualization of two fluorescent objects in 3D, spaced by a distance that is fully compatible with the known size of the respective Nbs (Fig. 3a). To proceed to a larger molecule, we targeted GFP (Supplementary Fig. 22a,b). The results, obtained from 885 protein molecules, are shown in Supplementary Fig. 22b. To obtain a numerical estimate for the precision of the 3D shape obtained by ONE, we turned to a Fourier shell correlation analysis[36], comparing the ONE results to the cryo-EM structure. A value of 18 Å was obtained, suggesting that the overall resolution of the ONE procedure, from imaging to 3D reconstruction, is between 1 and 2 nm.

We finally turned to a substantially more complex object, a human $GABA_A$R homopentamer[24].The analysis of 4,938 two-dimensional (2D) views of molecules resulted in the 3D shape depicted in Fig. 3b, in comparison to both AlphaFold[37] predictions and crystallography-derived structures (Fig. 3c). A Fourier shell correlation analysis provided a value of 16 Å, again suggesting that the precision of the technique, in 3D, lies between 1 and 2 nm.

Overall, these results demonstrate that the ONE microscopy images are representative of the respective molecular structures. While the 3D shapes obtained have a substantially lower resolution than structures derived from crystallography and cryo-EM, our results imply that the generation of protein structures from fluorescence images should be possible.

Clinical sample analysis: Parkinson disease (PD)

In principle, all of the observations made above could be reproduced, at higher resolution, in cryo-EM imaging. However, cryo-EM faces challenges in observing specific proteins or protein assemblies in complex mixtures, unless they have special density and/or shape features[38]. ONE microscopy can rely on specific epitope recognition, thereby avoiding this problem. To test this, we sought to address a pathology-relevant imaging challenge, focusing on PD, a neurodegenerative disease characterized by the accumulation of aggregates composed of several proteins, of which α-synuclein (ASYN) is the most prominent[39]. In the cell, ASYN can exist as a monomer or can assemble into species of different sizes, including soluble oligomers and fibrils. A substantial number of studies focused on ASYN as a PD biomarker. Genetic changes (mutations) in *SNCA* (the gene for ASYN) are poor biomarkers because familial PD accounts for a minority of all cases. Measuring the ASYN levels has also proven to lack diagnostic relevance. Measuring post-translational modifications (for example, phosphorylation) has similarly been difficult to use as a biomarker. The combination of ASYN phosphorylation analyses with other parameters, including nerve fiber morphology, amyloid deposition and skin histology, has been more successful[40], leading to a commercial PD biomarker test (Syn-One Test, CND Life Sciences). However, it is unclear whether phosphorylated ASYN is a toxic species because it seems to inhibit seeded fibril formation and toxicity[41] while also being a physiological form of ASYN involved in synaptic transmission.

The ideal diagnostic procedure would reveal the actual toxic species, which are thought to be ASYN oligomers (reviewed previously[42]). This has been exceedingly difficult because the performance

https://doi.org/10.1038/s41587-024-02431-9

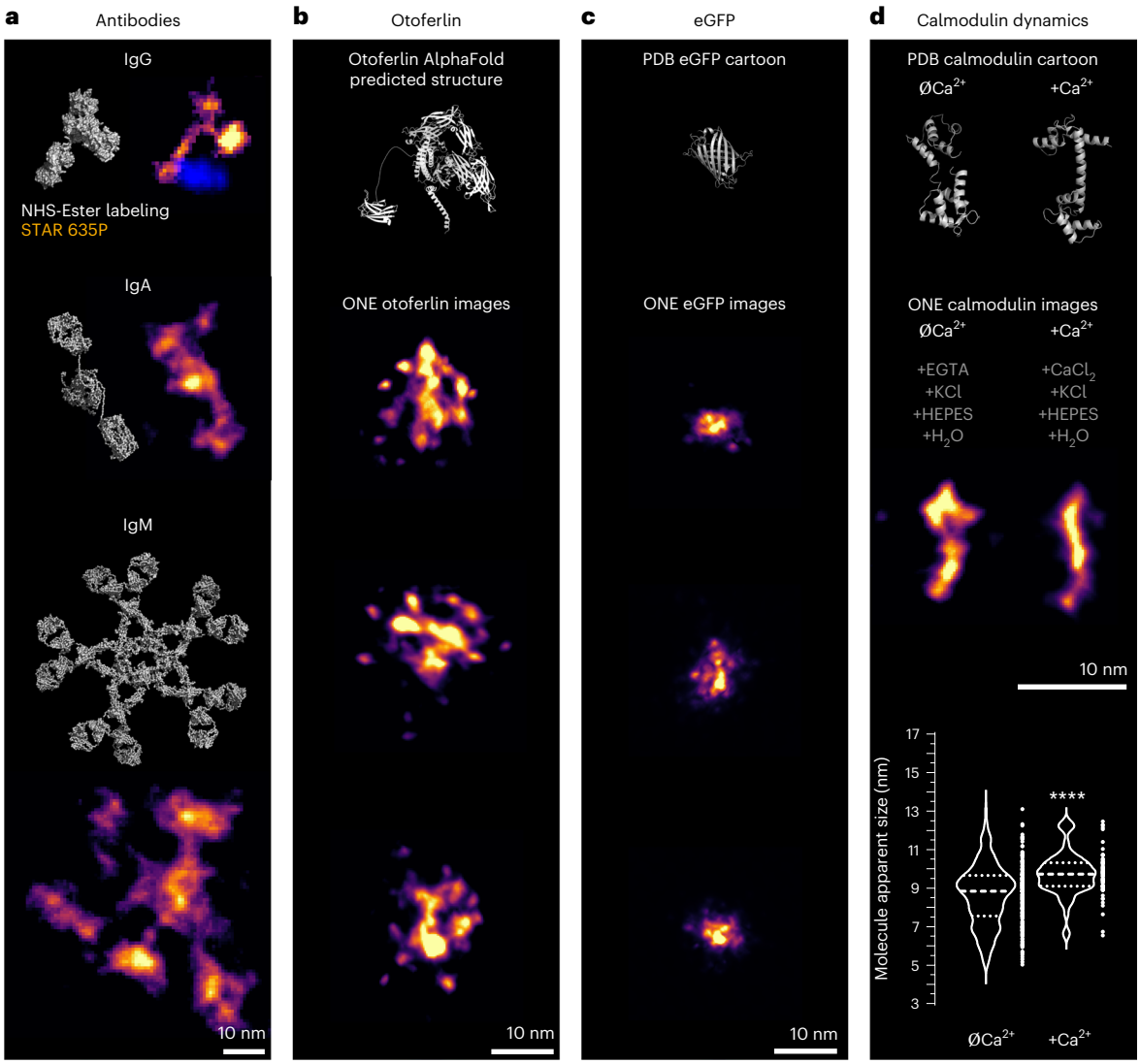

Fig. 2 | ONE analysis of single molecules. To delineate protein shapes, gels containing proteins were labeled with NHS-ester fluorescein after homogenization. **a**, ONE images of isolated immunoglobulins (secondary anti-mouse IgG conjugated to STAR 635P, human IgA and IgM and their respective PDB structures: 1HZH, 1IGA and 2RCJ) obtained from three independent experiments. Immunoglobulin ONE images were analyzed by a different fluctuation analysis, TRPPM, unlike the TRAC4 (ref. 12) approach used in most other figures. Unlike TRAC4, which aims to separate the individual fluorophores, TRPPM enhances the cohesiveness of the fluorophores decorating the single antibodies, resulting in cloud-like signals. Overviews and more analysis can be found in Supplementary Fig. 10. **b**, ONE examples of otoferlin images obtained from at least three independent experiments. The otoferlin model is an AlphaFold prediction. Overviews, control experiments and the otoferlin gallery can be found in Supplementary Fig. 11. **c**, GFP ONE images obtained from three independent experiments and the PDB 1EMA structure. Overviews, size measurements and the GFP gallery can be found in Supplementary Fig. 12. **d**, Structures (PDB 1CLL and 1CFD) of the Ca^{2+} sensor calmodulin, in the presence or absence of its ligand, respectively, along with ONE images after proteinase K-based homogenization and expansion. The expected elongation by ~1 nm was reproduced, as shown by the quantification, which indicates measurements of the longest axis of the calmodulin molecules, performed across all molecules, from all conditions, in a blind fashion ($P < 0.0001$, two-tailed nonparametric Mann–Whitney test; $n = 66–197$). Similar analysis, after homogenization using autoclaving ($P = 0.0006$, $n = 70–155$; Supplementary Fig. 13). The violin plot shows the median, the 25th percentile and the range of values.

of oligomer-specific ASYN antibodies is highly contested[43]. Importantly, ASYN-containing aggregates are present in the cerebrospinal fluid (CSF) and serum of both persons with PD and controls[44]. Thus, simply identifying aggregates (even oligomer-sized ones) is not useful for diagnostics; being able to reveal the toxic ones, those present specifically in persons with PD, would be much more valuable. Notably, a frequently used procedure for PD diagnostics, the seed amplification assay, does not even attempt to identify such species because of difficulties in their analysis.

We argued that insufficient resolution is the main problem in identifying such oligomers and ONE microscopy should be able to reveal them. We analyzed ASYN assemblies in the CSF of persons with PD versus controls (Supplementary Table 1) using an Nb[45]. Full-length immunoglobulins provide poor labeling because of their large size (Supplementary Fig. 24). Different types of ASYN assemblies could be detected (Fig. 4a,b) and persons with PD had higher levels of oligomer-like structures (Fig. 4c,d and Supplementary Fig. 25). All oligomer-like species were significantly more abundant in PD CSF than in control samples (Fig. 4f) and their cumulative analysis, which alleviated ambiguities because of imperfect classification of oligomer types, resulted in a good discrimination of persons with PD and age-matched controls (Fig. 4g,h). Analyses of the different ASYN species may prove to be relevant for diagnostics because some correlate to medication status while others may relate to clinical features (Supplementary Fig. 26). The analysis of ASYN aggregates by ONE microscopy is, therefore, a

https://doi.org/10.1038/s41587-024-02431-9

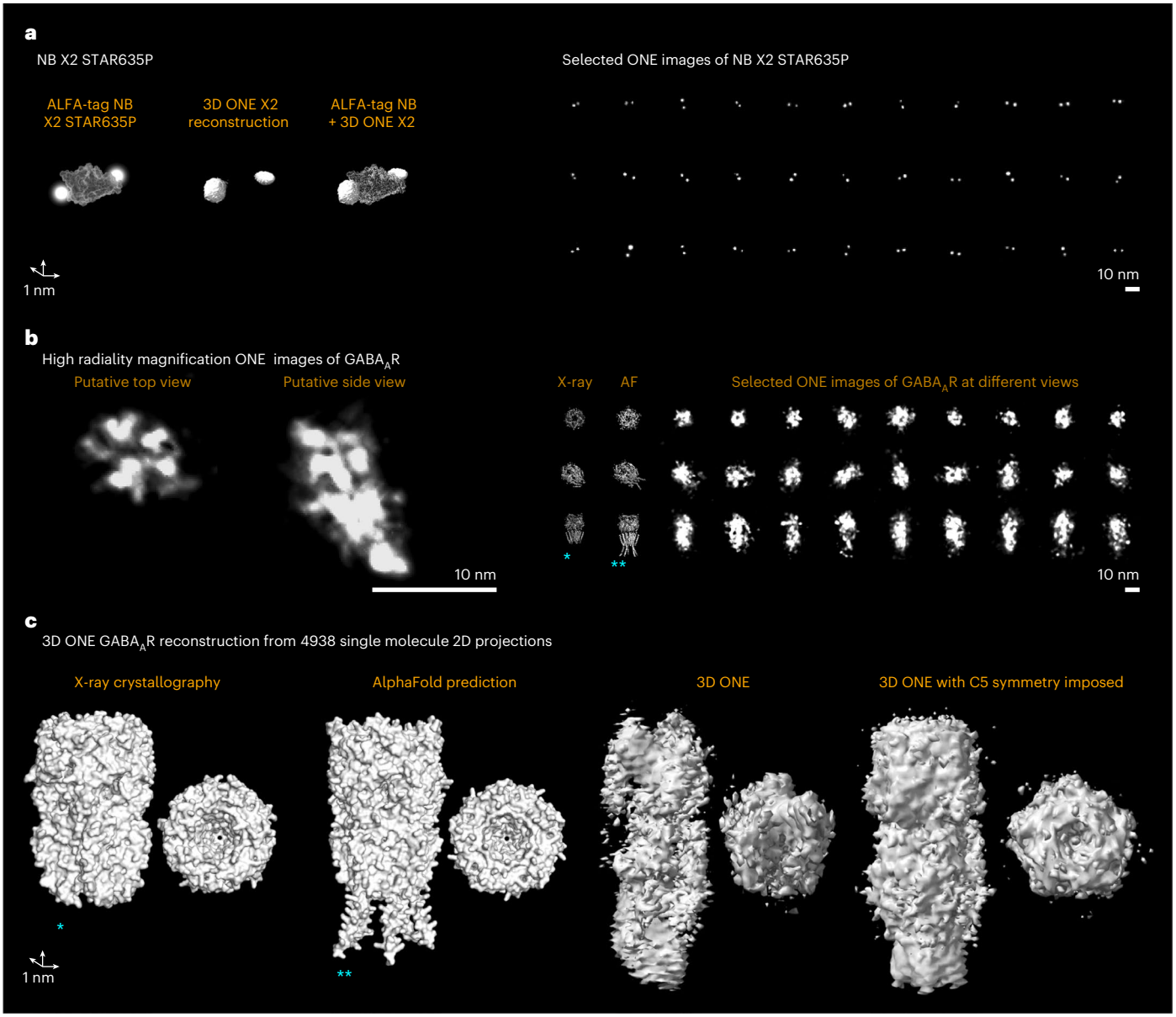

Fig. 3 | 3D ONE reconstruction using unsupervised ab initio artificial intelligence architecture. To reconstruct 3D models from 2D ONE images, segmented single molecules were transferred to a modified cryoFIRE neural network[35] (the neural network workflow can be found in Supplementary Fig. 22a). **a**, To run a sanity test on the reconstructed images, we used ONE images of 279 ALFA tag Nb STAR 635P with two fluorophores at known positions. This experiment used the inherent signal of the X2 STAR 635P fluorophores, foregoing additional labeling. The panel on the left shows the following: left, a model for the ALFA tag Nb structure (PDB 6I2G) in mesh representation, carrying two fluorophores; middle, 3D ONE X2 reconstruction; right, a view of both the 3D ONE X2 reconstruction and the Nb. The panel on the right shows selected ONE images of Nb X2 STAR 635P. The generated 3D positions of X2 fluorophores were at 4.6-nm distance, which correlates well with the measured line scans of 2D ONE images at 4.5 nm (Supplementary Fig. 14a–e). **b**, ONE images of NHS-ester fluorescein-labeled GABA$_A$R in top and side views, obtained with high-radiality magnification (Supplementary Discussion). A gallery of GABA$_A$R in different positions is shown. **c**, 3D representations of GABA$_A$R generated by crystal structure (PDB 4COF), by an AlphaFold-Multimer[37] prediction, by 3D ONE (raw) and by 3D ONE after imposing *C5* symmetry to the molecule. Side and top views are shown. The crystallography structure does not indicate segments that are shown in the AlphaFold model. These segments are visible in the 3D ONE reconstruction. The increased length of the 3D ONE reconstruction, when compared to the AlphaFold model, is probably accounted for by the fact that AlphaFold predicts a substantial unfolded coil in this region, which is not depicted (full AlphaFold-predicted models and error estimates can be found in Supplementary Fig. 23). 3D ONE reconstructions and AlphaFold-predicted models are provided in the Supplementary Information (PDB or MRC files; all reconstruction files have self-explanatory names). Fourier shell correlation analysis indicated that the 3D ONE reconstruction is generated at a resolution of 16 Å. The cyan asterisks indicate the following: *components known to be missing in the PDB 4COF structure; **AlphaFold prediction unclear in this area, as AlphaFold cannot reliably predict disordered domains.

promising procedure for PD diagnosis and possibly for monitoring the disease status.

Multilaboratory applications of ONE microscopy

An important issue for any new technology is its wide applicability in multiple laboratories. To test this issue, we collaborated with academic laboratories in Homburg and at Massachusetts Institute of Technology (MIT), as well as with the industrial laboratory of microscope developer Leica Microsystems. We focused on GABA$_A$Rs, samples that were well described in the rest of the work (Supplementary Figs. 27–29). We were able to show that ONE can be applied in different laboratories, with some of the experiments even surpassing our original applications by

https://doi.org/10.1038/s41587-024-02431-9

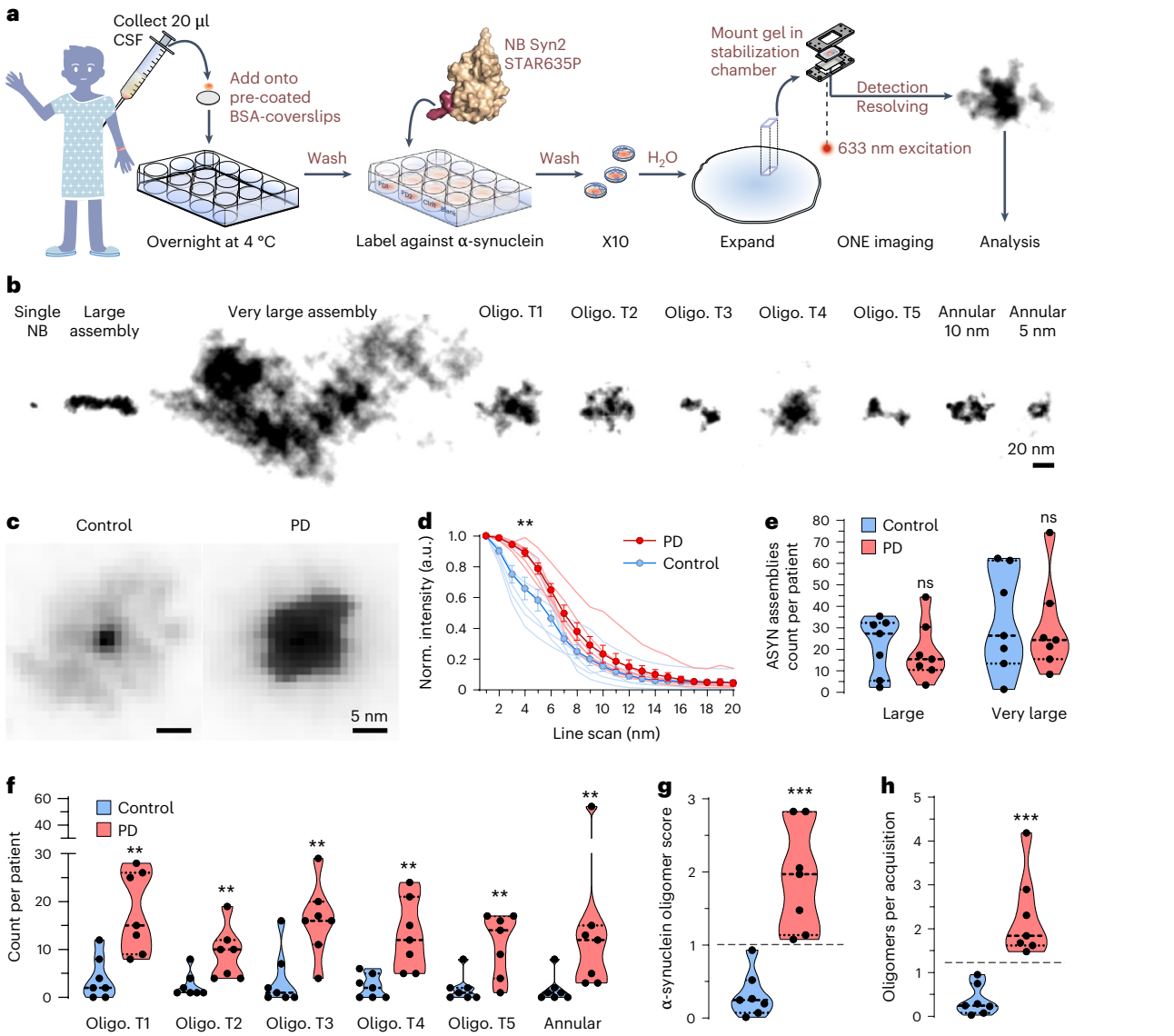

Fig. 4 | Detection of ASYN oligomers in human CSF. a, CSF probes were obtained from persons with PD and controls and 20-µl volumes were placed on BSA-coated coverslips, followed by ONE imaging after immunolabeling ASYN using a specific Nb[45]. **b**, A gallery of typical ASYN species observed in the CSF samples. Only the fluorophores contained by the Nbs are visualized here (no postexpansion labeling). **c**, Average ASYN assemblies from a person with PD and a control. **d**, An analysis of the spot profiles detects significant differences, with the average control object being smaller than the average PD object. All ASYN assemblies for the control and persons with PD were averaged from three independent experiments. Significant differences were determined by a Friedman test followed by Dunn–Šidák correction ($P = 0.0237$); errors show the s.e.m. AU, arbitrary units. **e**, An analysis of the number of larger assemblies in CSF samples. No significant differences were determined according to Mann–Whitney tests ($P = 1$ and 0.7104). NS, not significant. **f**, An analysis of the number of oligomers in CSF samples. All comparisons indicated significant differences according to Mann–Whitney tests followed by a Benjamini–Hochberg multiple-testing correction with a false discovery rate of 2.5% ($P = 0.0105$, 0.0023, 0.0111, 0.0012 and 0.0012, in the respective order of datasets). **g**,**h**, Analyses of the number of oligomers as a proportion of all ASYN assemblies analyzed (**g**) or as the number per acquisition (**h**). Both procedures discriminate fully between the persons with PD and the controls. For the second procedure, the lowest PD value is 50% larger than the highest control. Significant differences were determined by a two-tailed nonparametric Mann–Whitney test ($P < 0.0001$ for **h**,**g**); $n = 7$ persons with PD and $n = 7$ controls.

using either larger expansion factors (MIT laboratory, postexpansion stained bassoon in 20-fold expanded mouse brain tissue; Supplementary Fig. 29) or faster scanning to allow volumetric ONE imaging in two color channels (Leica Microsystems laboratory; Supplementary Fig. 27). We hope that future applications can be facilitated by the open-source software package we generated (Supplementary Fig. 30).

Discussion

ONE microscopy was applied here to analyze a variety of proteins, relying on conventional microscopes. No special handling, unusual fluorophores or reagents are necessary for this technique, which should enable the application of super-resolution analyses to laboratories without access to the best imaging instruments[46]. The initial immunostaining and expansion procedures take a total of 3–4 days, while imaging individual regions of interest only takes between 35 s and 2 min depending on the number of color channels; the SRRF-based procedure is then performed in minutes.

At the same time, several limitations should be considered carefully. Firstly, the ONE axial resolution surpasses that of confocal microscopy only by the expansion factor, implying that the axial and lateral resolutions differ by more than one order of magnitude. This can become a problem for dense samples; therefore, further improvements

in the axial resolution should be introduced in the future through methods such as total internal reflection fluorescence (TIRF), lattice light-sheet microscopy or multifocus microscopy. Secondly, applications to cell and tissue samples will require fixation, a procedure that can cause substantial artifacts. A combination of rapid freezing (or high-pressure freezing), fixation at subzero temperatures and rehydration would reduce such artifacts[32]. Thirdly, while ONE microscopy should be feasible for all ExM gel chemistries, it is likely that some gels will result in less homogeneous samples than others, thereby changing the signals in an unpredictable fashion. This implies that each gel type needs to be carefully calibrated before use.

Unlike fluorescence imaging techniques that are based on imaging native structures (that is, essentially all tools other than ExM), our approach is not limited by the size of the molecules to be analyzed. Normally, the shape of a small protein or peptide cannot be visualized in fluorescence because not enough fluorophores can be introduced into it. Our solution to this problem enables us to describe the shapes of molecules that could otherwise only be visualized by technologies such as cryo-EM. Lastly, a further advantage of ONE microscopy is that the fluorescence analysis is not dependent on molecular density, implying that extremely small objects, such as the peptide mCLING, can be analyzed, although they may be virtually invisible for density-based techniques such as EM.

Overall, ONE is a simple and easily applicable technology to study the morphology of proteins with high resolution and has the potential to bridge the gap between X-ray crystallography and EM-based techniques.

Online content

Any methods, additional references, Nature Portfolio reporting summaries, source data, extended data, supplementary information, acknowledgements, peer review information; details of author contributions and competing interests; and statements of data and code availability are available at https://doi.org/10.1038/s41587-024-02431-9.

References

1. Balzarotti, F. et al. Nanometer resolution imaging and tracking of fluorescent molecules with minimal photon fluxes. *Science* **355**, 606–612 (2017).
2. Gwosch, K. C. et al. MINFLUX nanoscopy delivers 3D multicolor nanometer resolution in cells. *Nat. Methods* **17**, 217–224 (2020).
3. Sahl, S. J. et al. Direct optical measurement of intra-molecular distances down to the Ångström scale. Preprint at *bioRxiv* https://doi.org/10.1101/2023.07.07.548133 (2023).
4. Reinhardt, S. C. M. et al. Ångström-resolution fluorescence microscopy. *Nature* **617**, 711–716 (2023).
5. Lelek, M. et al. Single-molecule localization microscopy. *Nat. Rev. Methods Primers* **1**, 39 (2021).
6. Helmerich, D. A. et al. Photoswitching fingerprint analysis bypasses the 10-nm resolution barrier. *Nat. Methods* **19**, 986–994 (2022).
7. Chen, F., Tillberg, P. W. & Boyden, E. S. Expansion microscopy. *Science* **347**, 543–548 (2015).
8. Cahoon, C. K. et al. Superresolution expansion microscopy reveals the three-dimensional organization of the *Drosophila* synaptonemal complex. *Proc. Natl Acad. Sci. USA* **114**, E6857–E6866 (2017).
9. Gao, M. et al. Expansion stimulated emission depletion microscopy (ExSTED). *ACS Nano* **12**, 4178–4185 (2018).
10. Xu, H. et al. Molecular organization of mammalian meiotic chromosome axis revealed by expansion STORM microscopy. *Proc. Natl Acad. Sci. USA* **116**, 18423–18428 (2019).
11. Dertinger, T., Colyer, R., Iyer, G., Weiss, S. & Enderlein, J. Fast, background-free, 3D super-resolution optical fluctuation imaging (SOFI). *Proc. Natl Acad. Sci. USA* **106**, 22287–22292 (2009).
12. Gustafsson, N. et al. Fast live-cell conventional fluorophore nanoscopy with ImageJ through super-resolution radial fluctuations. *Nat. Commun.* **7**, 12471 (2016).
13. Laine, R. F. et al. High-fidelity 3D live-cell nanoscopy through data-driven enhanced super-resolution radial fluctuation. *Nat. Methods* **20**, 1949–1956 (2023).
14. Culley, S., Tosheva, K. L., Matos Pereira, P. & Henriques, R. SRRF: universal live-cell super-resolution microscopy. *Int. J. Biochem. Cell Biol.* **101**, 74–79 (2018).
15. Truckenbrodt, S. et al. X10 expansion microscopy enables 25-nm resolution on conventional microscopes. *EMBO Rep.* **19**, e45836 (2018).
16. Truckenbrodt, S., Sommer, C., Rizzoli, S. O. & Danzl, J. G. A practical guide to optimization in X10 expansion microscopy. *Nat. Protoc.* **14**, 832–863 (2019).
17. Raab, M. et al. Using DNA origami nanorulers as traceable distance measurement standards and nanoscopic benchmark structures. *Sci. Rep.* **8**, 1780 (2018).
18. Li, R., Chen, X., Lin, Z., Wang, Y. & Sun, Y. Expansion enhanced nanoscopy. *Nanoscale* **10**, 17552–17556 (2018).
19. Klimas, A. et al. Magnify is a universal molecular anchoring strategy for expansion microscopy. *Nat. Biotechnol.* **41**, 858–869 (2023).
20. Cipriano, B. H. et al. Superabsorbent hydrogels that are robust and highly stretchable. *Macromolecules* **47**, 4445–4452 (2014).
21. Gao, R. et al. A highly homogeneous polymer composed of tetrahedron-like monomers for high-isotropy expansion microscopy. *Nat. Nanotechnol.* **16**, 698–707 (2021).
22. Damstra, H. G. J. et al. Visualizing cellular and tissue ultrastructure using ten-fold robust expansion microscopy (TREx). *eLife* **11**, e73775 (2022).
23. M'Saad, O. & Bewersdorf, J. Light microscopy of proteins in their ultrastructural context. *Nat. Commun.* **11**, 3850 (2020).
24. Miller, P. S. & Aricescu, A. R. Crystal structure of a human GABAA receptor. *Nature* **512**, 270–275 (2014).
25. Roux, I. et al. Otoferlin, defective in a human deafness form, is essential for exocytosis at the auditory ribbon synapse. *Cell* **127**, 277–289 (2006).
26. Jumper, J. et al. Highly accurate protein structure prediction with AlphaFold. *Nature* **596**, 583–589 (2021).
27. Saal, K. A. et al. Heat denaturation enables multicolor X10-STED microscopy. *Sci Rep.* **13**, 5366 (2023).
28. Shaib, A. H. et al. Expansion microscopy at one nanometer resolution. Preprint at *bioRxiv* https://doi.org/10.1101/2022.08.03.502284 (2022).
29. Gürth, C.-M. et al. Neuronal activity modulates the incorporation of newly translated PSD-95 into a robust structure as revealed by STED and MINFLUX. Preprint at *bioRxiv* https://doi.org/10.1101/2023.10.18.562700 (2023).
30. Sograte-Idrissi, S. et al. Nanobody detection of standard fluorescent proteins enables multi-target DNA-PAINT with high resolution and minimal displacement errors. *Cells* **8**, 48 (2019).
31. Gotzke, H. et al. The ALFA-tag is a highly versatile tool for nanobody-based bioscience applications. *Nat. Commun.* **10**, 4403 (2019).
32. Revelo, N. H. et al. A new probe for super-resolution imaging of membranes elucidates trafficking pathways. *J. Cell Biol.* **205**, 591–606 (2014).
33. Henderson, R. Avoiding the pitfalls of single particle cryo-electron microscopy: Einstein from noise. *Proc. Natl Acad. Sci. USA* **110**, 18037–18041 (2013).
34. Culley, S. et al. Quantitative mapping and minimization of super-resolution optical imaging artifacts. *Nat. Methods* **15**, 263–266 (2018).

35. Levy, A., Wetzstein, G., Martel, J., Poitevin, F. & Zhong, E.D. Amortized inference for heterogeneous reconstruction in cryo-EM. Preprint at https://arxiv.org/abs/2210.07387 (2022).
36. Scheres, S. H. RELION: implementation of a Bayesian approach to cryo-EM structure determination. *J. Struct. Biol.* **180**, 519–530 (2012).
37. Evans, R. et al. Protein complex prediction with AlphaFold-Multimer. Preprint at *bioRxiv* https://doi.org/10.1101/2021.10.04.463034 (2022).
38. Rickgauer, J. P., Choi, H., Lippincott-Schwartz, J. & Denk, W. Label-free single-instance protein detection in vitrified cells. Preprint at *bioRxiv* https://doi.org/10.1101/2020.04.22.053868 (2020).
39. Schmitz, M. et al. α-Synuclein conformers reveal link to clinical heterogeneity of α-synucleinopathies. *Transl. Neurodegener.* **12**, 12 (2023).
40. Gibbons, C. et al. Cutaneous α-synuclein signatures in patients with multiple system atrophy and Parkinson disease. *Neurology* **100**, e1529–e1539 (2023).
41. Ghanem, S. S. et al. α-Synuclein phosphorylation at serine 129 occurs after initial protein deposition and inhibits seeded fibril formation and toxicity. *Proc. Natl Acad. Sci. USA* **119**, e2109617119 (2022).
42. Wang, R. et al. A review of the current research on in vivo and in vitro detection for α-synuclein: a biomarker of Parkinson's disease. *Anal. Bioanal. Chem.* **415**, 1589–1605 (2023).
43. Kumar, S. T. et al. How specific are the conformation-specific α-synuclein antibodies? Characterization and validation of 16 α-synuclein conformation-specific antibodies using well-characterized preparations of α-synuclein monomers, fibrils and oligomers with distinct structures and morphology. *Neurobiol. Dis.* **146**, 105086 (2020).
44. Lobanova, E. et al. Imaging protein aggregates in the serum and cerebrospinal fluid in Parkinson's disease. *Brain* **145**, 632–643 (2022).
45. De Genst, E. J. et al. Structure and properties of a complex of α-synuclein and a single-domain camelid antibody. *J. Mol. Biol.* **402**, 326–343 (2010).
46. Callaway, E. 'Democracy in microscopy': cheap light microscope delivers super-resolution images. *Nature* **616**, 417–418 (2023).

[1]Institute for Neuro- and Sensory Physiology, University Medical Center Göttingen, Göttingen, Germany. [2]Department of Cellular Neurophysiology, Center for Integrative Physiology and Molecular Medicine (CIPMM), Saarland University, Homburg, Germany. [3]Department of Chemistry, GITAM School of Science, GITAM, Hyderabad, India. [4]MRC Laboratory of Molecular Biology, Cambridge, UK. [5]Department of Brain and Cognitive Sciences, Massachusetts Institute of Technology, Cambridge, MA, USA. [6]Department of Biological Engineering, Massachusetts Institute of Technology, Cambridge, MA, USA. [7]McGovern Institute, Massachusetts Institute of Technology, Cambridge, MA, USA. [8]Howard Hughes Medical Institute, Massachusetts Institute of Technology, Cambridge, MA, USA. [9]Koch Institute, Massachusetts Institute of Technology, Cambridge, MA, USA. [10]Center for Neurobiological Engineering, Massachusetts Institute of Technology, Cambridge, MA, USA. [11]Institute for Theoretical Physics, Georg-August University, Göttingen, Germany. [12]Center for Biostructural Imaging of Neurodegeneration, University Medical Center Göttingen, Göttingen, Germany. [13]Biochemistry of Membrane Dynamics Group, Institute for Auditory Neuroscience, University Medical Center Göttingen, Göttingen, Germany. [14]Institute for X-Ray Physics, University of Göttingen, Göttingen, Germany. [15]Institute for Auditory Neuroscience and InnerEarLab, University Medical Center Göttingen, Göttingen, Germany. [16]Department of Biotechnology and Biophysics, Biocenter, University of Würzburg, Am Hubland, Würzburg, Germany. [17]Institute of Computer Science, Georg-August University Göttingen, Göttingen, Germany. [18]Leica Microsystems CMS GmbH, Mannheim, Germany. [19]Department of Neurosurgery, University Medical Center, Göttingen, Germany. [20]Paracelsus-Elena-Klinik, Kassel, Germany. [21]Department of Neurology, University Medical Center, Göttingen, Germany. [22]Department of Experimental Neurodegeneration, Center for Biostructural Imaging of Neurodegeneration, University Medical Center Göttingen, Göttingen, Germany. [23]Max Planck Institute for Multidisciplinary Sciences, Göttingen, Germany. [24]Translational and Clinical Research Institute, Faculty of Medical Sciences, Newcastle University, Newcastle upon Tyne, UK. [25]German Center for Neurodegenerative Diseases (DZNE), Göttingen, Germany. [26]Cluster of Excellence "Multiscale Bioimaging: from Molecular Machines to Networks of Excitable Cells" (MBExC), University of Göttingen, Göttingen, Germany. [27]Auditory Neuroscience and Synaptic Nanophysiology Group, Max Planck Institute for Multidisciplinary Sciences, Göttingen, Germany. [28]NanoTag Biotechnologies GmbH, Göttingen, Germany. ✉e-mail: ali.shaib@med.uni-goettingen.de; srizzol@gwdg.de

Methods

Nanorulers

Custom-designed linear nanorulers of varying length (80, 60, 50, 30, 20 and 10 nm), carrying one Atto 647N molecule on each end, were purchased from GATTAquant.

Cell cultures

Hippocampal cultured neurons. Animals (Wistar rats, P0–P1) were treated according to the regulations of the local authority, the Lower Saxony State Office for Consumer Protection and Food Safety (Niedersächsisches Landesamt für Verbraucherschutz und Lebensmittelsicherheit), under the license Tötungsversuch T09/08. In brief, the hippocampi were dissected from the brains and washed with Hank's balanced salt solution (14175-053, Invitrogen), before being incubated under slow rotation in a digestion solution containing 15 U per ml papain (LS003126, Worthington), 1 mM $CaCl_2$ (A862982745, Merck), 0.5 mM EDTA and 0.5 mg ml^{-1} L-cysteine (30090, Merck) in DMEM. This procedure was performed for 1 h at 37 °C, before enzyme inactivation with a buffer containing 10% fetal calf serum (FCS) and 5 mg ml^{-1} BSA (A1391, Applichem) in DMEM. The inactivation solution was replaced after 15 min with the growth medium, containing 10% horse serum (S900-500, VWR International), 1.8 mM glutamine and 0.6 mg ml^{-1} glucose in MEM (51200046, Thermo Fisher Scientific), which was used to wash the hippocampi repeatedly. The neurons were then isolated by trituration using a glass pipette and sedimented by centrifugation at 80*g* (8 min). The cells were then resuspended in the same medium and seeded on poly(L-lysine) (PLL)-coated coverslips for several hours, before replacing the buffer with Neurobasal A culture medium (10888-022, Thermo Fisher Scientific) containing 0.2% B27 supplement (17504-044, Thermo Fisher Scientific) and 2 mM GlutaMAX (35050-038, Thermo Fisher Scientific). The neurons were then maintained in a humidified incubator (5% CO_2, 37 °C) for at least 14 days before use.

Conventional cell cultures. Tubulin immunostaining was performed in the U2OS cell line, obtained from the Cell Lines Service (CLS). The cells were grown in a humidified incubator (5% CO_2, 37 °C) in DMEM (D5671, Merck) with the addition of 10% FCS (S0615, Merck), 4 mM glutamine (25030-024, Thermo Fisher Scientific) and an antibiotic mixture added at 1% (penicillin–streptomycin; Thermo Fisher Scientific). For imaging purposes, cells were grown overnight on PLL-coated coverslips (P2658, Merck).

Brain slices

We dissected rat brains from P0–P1 rat pups (Wistar). The brains were then fixed with 4% PFA (30525894, Merck) in PBS for 20 h. The fixed brains were then placed in agarose (4% solution; 9012366, VWR Life Science), before cutting to the desired thickness (100–200 µm) using a vibratome.

Participants

Participants were in treatment at the Paracelsus Elena Klinik. They were diagnosed with PD according to standard criteria[47–49]. Neurological control participants were diagnosed with a variety of non-neurodegenerative disorders. A detailed presentation of participants, their ages and their diagnoses can be found in Supplementary Table 1. The informed consent of all of the participants was obtained at the Paracelsus Elena Klinik, following the principles of the Declaration of Helsinki.

CSF samples

CSF samples were collected at the Paracelsus Elena Klinik following identical standard operating procedures. CSF was obtained by lumbar puncture in the morning with the participants fasting and in sitting position. The CSF was processed by centrifugation at 2,000*g* for 10 min at room temperature; aliquots of supernatant were frozen within 20–30 min and stored at −80 °C until analysis. Samples with a red blood cell count > 25 $µl^{-1}$ or indication for an inflammatory process were excluded.

Immunostaining procedures

Tubulin immunostaining. U2OS cells were first incubated with 0.2% saponin (47036, Sigma-Aldrich) to extract lipid membranes. This procedure was performed for 1 min in cytoskeleton buffer, consisting of 10 mM MES (M3671, Merck), 138 mM KCl (K42209636128, Merck), 3 mM $MgCl_2$ (M8266-100G, Sigma-Aldrich), 2 mM EGTA (324626-25GM, Merck) and 320 mM sucrose at pH 6.1. The cells were then fixed using 4% PFA and 0.1% glutaraldehyde (A3166, PanReac) in the same buffer. Unreacted aldehyde groups were quenched using 0.1% $NaBH_4$ (71320, Sigma-Aldrich now Merck) for 7 min in PBS, followed by a second quenching step with 0.1 M glycine (3187, Carl Roth) for 10 min in PBS. The samples were blocked and simultaneously permeabilized using 2% BSA and 0.1% Triton X-100 (9036-19-5, Sigma-Aldrich) in PBS (room temperature, 30 min). Primary anti-tubulin antibodies (T6199 Sigma-Aldrich; 302211, Synaptic Systems; 302203, Synaptic Systems; ab18251, Abcam) were applied for 60 min at room temperature and were then washed off with permeabilization buffer, followed by an incubation of the samples with secondary antibodies (ST635P-1001, Abberior). Five washes were performed with permeabilization buffer followed by three PBS washes (each for 10 min) before continuing with cellular expansion.

PSD95 immunostaining. Neurons were fixed with 4% PFA in PBS (D8537-500ML, Thermo Fisher Scientific) for at least 30 min before quenching with 50 mM glycine (in PBS) for 10 min and blocking and permeabilizing using 2.5% BSA (9048-46-8, Sigma-Aldrich), 2.5% normal goat serum (NGS) and 0.1% Triton X-100 (1003287133, Sigma-Aldrich) in PBS (30 min at room temperature, unless specified otherwise). The antibodies and/or primary Nbs were diluted in 2.5% BSA and 2.5% NGS in PBS and added to coverslips for 60 min at room temperature. This was followed by washing with the permeabilization buffer (30 min, three buffer exchanges) and by incubation with the primary Nb FluoTag-X2 anti-PSD95 (clone 1B2; N3702, NanoTag Biotechnologies) for 1 h at room temperature. Specimens were then washed five times with permeabilization buffer before a final wash with PBS (15–30 min, three buffer exchanges), followed by expansion procedures.

Immunostaining of CSF samples. CSF probes were obtained from persons with PD and controls at the Paracelsus Elena Klinik and stored at −80 °C before use. Then, 20 µl of CSF was placed on BSA-coated coverslips, enabling the sedimentation of multiprotein species overnight at 4 °C. Fixation with 4% PFA (10 min, room temperature) and quenching with 50 mM glycine (10 min, room temperature) were followed by the application of anti-ASYN antibodies (128211 and 128002, Synaptic Systems) or ASYN Nb2 (SynNb2 (ref. 45), custom-produced and fluorescently conjugated by NanoTag) for 1 h at room temperature in 2.5% BSA in PBS buffer. For the case of antibodies, secondary Abberior STAR 635P was applied for 1 h at room temperature. Five washes with 2.5% BSA in PBS were followed by mild postfixation with 4% PFA for 4 min and expansion procedures.

Brain slice immunostaining. The fixed brain slices were first quenched using 50 mM glycine (in PBS), followed by three washes with PBS (each for 5 min) and blocking and permeabilization in PBS containing 2.5% BSA and 0.3% Triton X-100 for 120 min at room temperature. The primary antibodies used (anti-bassoon, ADI-VAM-PS003-F, Enzo Life Sciences; anti-Homer 1, 160003, Synaptic Systems) were diluted in the same buffer (lacking Triton X-100) to 2 µg ml^{-1} and added to the slices overnight at 4 °C. Three washes with PBS (each for 5 min) removed the primary antibodies, enabling the addition of secondary antibodies conjugated with Abberior STAR 635P (ST635P-1001, Abberior)

for Basson identification. The secondary antibodies were diluted to 1 µg ml^{-1} in PBS containing 2.5% BSA and incubated for 3 h at room temperature. The brain slices were finally subjected to five washes with PBS containing 2.5% BSA (each wash for 5 min), followed by two final 5-min washes in PBS.

GFP–Nb complex (TSR) generation

The monomeric (A206K) and nonfluorescent (Y66L) EGFP (mEGFP*) was modified to have an ALFA tag on its N terminus and a HaloTag on its C terminus (ALFA-EGFP-HaloTag). This construct was expressed in a NebExpress bacterial strain and it had an N-terminal His-tag, followed by a bdSUMO domain, which enabled the specific cleavage of the His-tag[31] after the purification procedures. Bacteria were grown at 37 °C with shaking at 2*g* in Terrific Broth (TB) supplemented with kanamycin. Upon reaching an optical density (OD) of ~3, the temperature was reduced to 30 °C and bacteria were induced using 0.4 mM IPTG, with shaking for another ~16 h. Bacteria lysates were incubated with Ni^+ resin (Roche, cOmplete) for 2 h at 4 °C. After several washing steps, the ALFA-mEGFP(Y66L)-HaloTag protein was eluted by enzymatic cleavage on the column using 0.1 µM SENP1 protease for 15 min. Protein concentration was determined using Nanodrop (Thermo Fisher Scientific) and purity was assessed by Coomassie gels. Complex formation was performed by mixing the following for 1 h at room temperature in a final volume of 40 µl: 25 pmol of ALFA-EGFP-HaloTag and 30 pmol of three different single-domain antibodies: FluoTag-Q anti-ALFA (N1505), FluoTag-X2 anti-GFP (clone 1H1; N0301) and FluoTag-X2 anti-GFP (clone 1B2), all from NanoTag Biotechnologies. The control experiments were performed using a similar procedure without including the target protein ALFA-EGFP-HaloTag. The expression and purification of EGFP used in Supplementary Figs. 15 and 16 were performed as previously described[50]. Briefly, NebExpress *Escherichia coli* strain (New England Biolabs) was cultured in TB at 37 °C and induced using 0.4 mM IPTG for 16 h at 30 °C. Bacteria pellets were sonicated on ice in 50 mM HEPES pH 8.0, 500 mM NaCl, 5 mM $MgCl_2$ and 10% glycerol. After removing cell debris by centrifugation, the lysate was incubated for 1 h with cOmplete His-tag purification resin (Roche) at 4 °C. After washing the resin in batch mode with more than ten column volumes, eGFP was enzymatically eluted using 0.1 µM SUMO protease. Concentration was determined by absorbance at 280 nm using the molecular weight and extinction coefficient of eGFP. Purified protein was diluted in 50% glycerol and stored in small aliquots at −80 °C.

PAGE

A primary mouse monoclonal antibody to synaptobrevin 2 (104211, Synaptic Systems) and a secondary antibody conjugated to Abberior STAR 635P (ST635P-1002-500UG) were mixed with reducing 2× Laemmli buffer (63 mM Tris-HCl pH 6.8, 2% SDS, 100 mM DTT and 20% glycerol) and heated for 10 min at 96 °C. The denatured and reduced samples were then loaded in a self-cast Tris-glycine 12% polyacrylamide gel and 10 µg of total protein was loaded per lane. Electrophoresis was run at low voltage at room temperature. The gel was briefly rinsed using distilled water and fluorescence was read on a GE-Healthcare AI 600 imager using a far-red filter (Cy5 channel). Next, the gel was submerged for 4 h in Coomassie brilliant blue solution to stain all proteins, followed by incubation with destaining solutions, before finally being imaged using the same GE-Healthcare AI 600 gel documentation system.

Dot blot

In a stripe of nitrocellulose membrane (GE-Healthcare), 5 mg of BSA and 1 µg of ALFA-tagged EGFP-Y66L-HaloTag were spotted and left to dry at room temperature. Membranes were then blocked in PBS supplemented with 5% skim milk and 0.05% Tween-20 for 1 h with tilting and shaking. FluoTag-X2 anti-GFP Cy3 (clone 1B1), FluoTag-X2 anti-GFP Abberior STAR 635P (clone 1H1) and Fluotag-X2 anti-ALFA Abberior STAR 635P (all from NanoTag) were used at 2.5 nM final concentration in PBS with 5% milk and 0.05% Tween-20 for 1 h with gentle rocking. After 1-h incubation at room temperature while protected from light, five washing steps were performed each using 2 ml of PBS supplemented with 0.05% Tween-20 for a total of 30 min. Membranes were finally imaged using a GE-Healthcare AI 600 system.

1,6-Hexanediol treatments. 1,6-Hexanediol (240117-50G, Sigma-Aldrich) was diluted in neuronal Neurobasal A culture medium at 3% for 2 min and 10% for 12 min before fixation and further processing for immunostaining.

Purified proteins

IgA and IgM were purchased from Jackson ImmunoResearch and IgG was purchased from Abberior (AffinityPure IgA 109-005-011, ChromePure IgM 009-000-012 and ST635P-1001, respectively) and all immunoglobulins were diluted in PBS before expansion procedures. Otoferlin was produced according to standard procedures[51] and was diluted in 20 mM HEPES, 100 mM KCl and 0.05% DDM buffer, before being used at 0.4 mg ml^{-1} concentration. For $GABA_A$Rs, a construct encoding the full-length human $GABA_A$R β3 subunit (UniProt P28472) with an N-terminal TwinStrep tag was cloned into the pHR-CMV-TetO2 vector[52]. A lentiviral cell pool was generated in HEK293S GnTI-TetR cells as described previously[53]. Cells were grown in FreeStyle 293 expression medium (12338018, Gibco) supplemented with 1% FBS (11570506, Gibco), 1 mM L-glutamine (25030149, Gibco), 1% NEEA (11140050, Gibco) and 5 µg ml^{-1} blasticidin (ant-bl-5b, Invivogen) at 37 °C (130 r.p.m., 8% CO_2) and induced as described[54]. Following collection by centrifugation (2,000*g*, 15 min), the cell pellets were resuspended in PBS pH 8 supplemented with 1% (v/v) mammalian protease inhibitor cocktail (Sigma-Aldrich). Cell membranes were solubilized with 1% (w/v) DDM (D3105GM, Anatrace) for 1 h. The insoluble material was removed by centrifugation (12,500*g*, 15 min) and the supernatant was incubated with 300 µl of Strep-Tactin Superflow resin (IBA Lifesciences) while rotating slowly for 2 h at 4 °C. The beads were collected by centrifugation (300*g*, 5 min) and washed with 150 ml of 0.04% (w/v) DDM and PBS pH 8. The sample was eluted in 2.5 mM biotin, 0.02% (w/v) DDM and PBS pH 8 and used for imaging at 1 mg ml^{-1} concentration. For the purification of the $GABA_A$R in complex with the β3-specific Nb (Nb25)[55], Nb25 was fluorescently labeled with STAR 635P at the N and C termini, generating Nb25-STAR 635P. Then, 20 µl of 10 µM Nb25-STAR 635P was added to the sample before the elution step and incubated for 2 h at 4 °C while rotating. The excess Nb25-STAR 635P was removed by washing the beads with six bed volumes of 0.04% (w/v) DDM and PBS pH 8, eluted with 2.5 mM biotin, 0.02% (w/v) DDM and PBS pH 8 and used for imaging at 3 mg ml^{-1} concentration. The same procedure was applied for the negative control anti-eGFP Nbs. To test that Nb25-STAR 635P could still bind the receptor, 2 µM Nb25-STAR 635P was added to the β3 homomeric receptor reconstituted in nanodiscs as described previously[56]. Next, 3.5 µl of the sample was applied to a freshly glow-discharged (PELCO easiGlow, 30 mA for 120 s) 1.2/1.3 UltrAuFoil grid (Quantifoil), which was blotted for 2.5 s and plunge-frozen using a Leica EM GP2 plunger at 14 °C and 99% humidity. Imaging was performed at the Medical Research Council (MRC) Laboratory of Molecular Biology on a Titan Krios G2 microscope equipped with an F4 detector in electron counting mode at 300 kV at a nominal magnification of 96,000×, corresponding to a calibrated pixel size of 0.824 Å. A total of 300 movies were collected using EPU (Thermo Fisher Scientific, version 2.0–2.11) with a total dose of 38 e^- per Å^2 and 6.43 s of exposure time. The movies were motion-corrected using MotionCor2 (ref. 57). Contrast transfer function estimation was performed with CTFFIND-4.1.13 (ref. 58). Particle picking was performed using a retrained BoxNet2D neural network in Warp[59], followed by 2D classification in cryoSPARC[60]. Calmodulin was purified as previously described[61] and was used in calcium-free buffer (150 mM KCl, 10 mM HEPES and 5 mM EGTA) or calcium-containing buffer (150 mM KCL, 10 mM HEPES and 2 mM $CaCl_2$)

at pH 7.2 before expansion procedures. Briefly, calmodulin 1 (mRNA reference sequence number NM_031969.2) was tagged with mEGFP and an ALFA tag for affinity purification purposes. The construct was transfected in HEK293 cells using Lipofectamine 2000 (11668019, Invitrogen) following the manufacturer's protocol. After expression for ~24 h, the cells were lysed in PBS buffer containing 1% Triton X-100, 2 mM EDTA and a protease inhibitor cocktail. The debris was removed by centrifugation and the supernatant was added to an ALFA Selector PE resin (NanoTag Biotechnologies), where it was allowed to bind for 60 min (4 °C, under rotation). After two washes with lysis buffer and one wash with PBS (ice-cold), the bound proteins were eluted by adding the ALFA peptide. The purified protein was analyzed by Coomassie gel imaging as previously described[61].

X10 expansion procedures

X10 expansion of cultured cells was performed using proteinase K exactly as described in the protocol article[16]. X10 expansion relying on autoclaving (X10ht[62]) was performed as follows. The samples were incubated overnight with 0.3 mg ml^{-1} Acryloyl-X (A-20770, Thermo Fisher Scientific) in PBS pH 7.4 at room temperature. The samples were then subjected to three PBS washes (5 min each) while preparing the gel monomer solution as previously described[16]. The solution was pipetted on parafilm and was covered with upside-down coverslips containing cells or with brain slices that were then also covered with fresh coverslips. Polymerization was allowed to proceed overnight at room temperature in a humidified chamber. Homogenization of proteins and single molecules was performed using 8 U per ml proteinase K (P4850, Sigma-Aldrich now Merck) in digestion buffer (800 mM guanidine HCl, 2 mM $CaCl_2$ and 0.5% Triton X-100 in 50 mM Tris; 8382J008706, Merck) overnight at 50 °C. Homogenization of cell cultures and brain slices was performed by autoclaving for 60 min at 110 °C in disruption buffer (5% Triton X-100 and 1% SDS in 100 mM Tris pH 8.0) followed by a 90-min incubation to cool the temperature to safe levels. Before autoclaving, the gels were washed first in 1 M NaCl and then at least four times in disruption buffer for a total time of at least 120 min. Gel expansion was then performed by washing with double-distilled water (ddH_2O) for several hours, with at least five solution exchanges. Expansion was performed in 22 × 22-cm square culture dishes, carrying 400–500 ml of ddH_2O. When desired, the samples were labeled using a 20-fold molar excess of NHS-ester fluorescein (46409, Thermo Fisher Scientific) in $NaCHO_3$ buffer at pH 8.3 for 1 h before the washing procedure that induced the final expansion.

ZOOM expansion procedures

Following a previously described protocol[63], fixed U2OS cultured cells were incubated in anchoring solution (25 mM acrylic acid NHS-ester in 60% (v/v) DPBS and 40% (v/v) DMSO) for 60 min. Afterward, cells were moved to monomer solution (30% (w/v) acrylamide and 0.014% (w/v) *N*-*N*′-methylenbisacrylamide in PBS buffer). After 60 min, the gelation process was started by adding initiators (0.5% (w/v) TEMED and 0.5% (w/v) APS) to the monomer solution. The hydrogel–cell hybrid was homogenized in detergent solution (200 mM SDS and 50 mM boric acid in deionized water, with the pH titrated to 9.0) at 95 °C for 15 min, followed by 24 h at 80 °C. ZOOM-processed samples were then stained using the previously mentioned anti-α-tubulin antibodies (1:400 in PBST).

mCLING expansion

For mCLING gelation, we started with 2 µl of mCLING-Atto 647N (710 006AT1, Synaptic Systems), originally reconstituted to a concentration of 1.0 nmol ml^{-1} and mixed with 2 µl of 10 mg ml^{-1} Acryloyl-X, before bubbling with N_2 gas for a few minutes to purge oxygen. This mixture was incubated overnight at 4 °C and then mixed with 100 µl of freshly prepared X10 polymer solution. Next, 80-µl aliquots of this gel-sample mixture were placed on parafilm in a humidified chamber and were covered with a clean 18-mm coverslip. Homogenization was carried out by X10 proteinase K digestion protocol, as previously described. Gels were then postexpansion labeled with NHS-ester fluorescein (46409, Thermo Fisher Scientific) or NHS-ester STAR 635P (07679-1MG, Sigma-Aldrich). Images were acquired using HyD X detectors on a STELLARIS 8 microscope.

mCLING structure simulation

The equilibrium structure of mCLING peptide-bonded to Atto 647N was assessed using molecular dynamics simulations with the AMBER99 force field[64]. The molecule was simulated in water using the TIP4P/EW model[65] in a cubic system of length 6 nm with periodic boundaries. The topology for the fluorophore was generated using ACPYPE[66], which interfaces with Antechamber from the AMBER suite of tools to create compatible topology files. The molecular dynamics package GROMACS[64] was used with the leap-frog algorithm to integrate Newton's equations of motion with a time step of 1 fs. Conditionally convergent long-range electrostatic interactions were calculated by the smooth particle mesh Ewald method with a cutoff distance of 1.2 nm. Lennard–Jones interactions were assessed using a single cutoff distance of 1.2 nm, supplemented by long-range dispersion corrections for both energy and pressure. After energy minimization, the system was equilibrated for 300 ns, followed by a 300-ns production run. The pressure was fixed at 1 bar by the Parrinello–Rahman barostat.

Microscope systems

For image acquisition, small gel fragments were cut and placed in the imaging chamber presented in Supplementary Fig. 7. Paper tissues were used to remove any water droplets around the gels, before enabling the gels to equilibrate for at least 30 min on the microscope stage. Epifluorescence imaging was performed using an Olympus IX83 TIRF microscope equipped with an Andor iXon Ultra 888, ×100 (1.49 numerical aperture (NA)) TIRF objective and Olympus LAS-VC four-channel laser illumination system. Confocal imaging was performed for most experiments using a TCS SP5 STED microscope (Leica Microsystems) with a ×100 (1.4 NA) HCX Plan Apochromat STED oil-immersion objective. The LAS AF imaging software (Leica) was used to operate imaging experiments. Excitation lines were 633, 561 and 488 nm and emission was tuned using an acousto-optical tunable filter. Detection was ensured by PMT and HyD detectors. Images were taken using a resonant scanner at 8-kHz frequency. The five-dimensional (5D) stacks for zONE were performed using a 12-kHz resonant scanner mounted on a Leica TCSSP8 Lightning confocal microscope. Samples were excited with a 40% white-light laser at wavelengths of 633, 561 and 488 nm and acquisitions were carried out using HyD detectors in unidirectional *xyct* line scans or in unidirectional and bidirectional *xyczt* line scans.

Image acquisition

Objectives of 1.4, 1.45 and 1.51 NA were used to acquire images with a theoretical pixel size of 98 nm. For a higher resolution, the theoretical pixel size was set to 48 nm at the cost of a slightly lower detection rate. Images acquired on the camera-based system had a predetermined pixel size of 100 nm. The acquisition speeds were 20–40 ms and 25 ms on resonant scanners of 8 and 12 kHz and on a camera, respectively, for *xyct*. For hyperstacks of *xyczt* acquisitions, images were acquired using 8-kHz and 12-kHz scanners in bidirectional mode (after the necessary alignments), allowing an achieved speed of 16 kHz and 24 kHz, respectively. Images of 8-bit depth were acquired at a line format ranging from 128 × 128 to 256 × 256. The scanning modality on a confocal was set to 'minimize time interval' (Leica LAS software). To maintain natural fluctuations of fluorophores, we did not use line accumulation or line averaging during scanning. A frame count from 200 up to 4,000 was acquired. We recommend a frame count of at least 1,500–2,000 for optimal computed resolution in *xyct* scans and 200–1,000 for *xyczt* scans for volume reconstructions.

Image processing

ONE image processing is enabled through a Java-written ONE Platform under 'ONE microscopy' in Fiji. The ONE microscopy plugin uses open-source codes from Bioformats Java library, NanoJ-Core, NanoJ-SRRF, NanoJ-eSRRF and Image Stabilizer[12,13,67,68]. ONE plugin supports multiple video formats of single or batch analyses in *xyct*. Hyperstacks with 5D *xyczt* format were processed with the zONE module. This module allows the user to select the optical slices and channels to resolve at ultraresolution. Upon irregularities in resolving one or more channels within one or more planes, zONE leaves a blank image and computes the remaining planes within a stack. The image processing is fully automated and requires minimal initial user input. Aside from the expansion factor, preset values and analysis modalities are automatically provided (see Supplementary Fig. 1 for more details). The ONE plugin has a preinstalled safety protocol to skip failures in computations or uncompensated drifts, without affecting the progress of batch analysis. Data analyses, parameters and irregularities are reported in log files. The ONE plugin automatically linearizes the scale on the basis of radiality magnification and expansion factor corrections. In addition, ONE offers the possibility to correct for chromatic aberration by processing multichannel bead images as a template that is applied to super-resolved images of the biological samples. The correction is performed by applying a modified Lucas–Kanade algorithm[67]. For the ONE microscopy plugin to store complex multidimensional images from hyperstacks, we modified the Java code of the ImageJ library and adapted it locally. The ONE Platform source code and plugin are available from GitHub (https://github.com/Rizzoli-Lab/ONE-Microscopy-Java-Plugin). For best performance, we recommend to download a preinstalled version on Fiji, available from the same link. The ONE plugin comes with predefined parameters optimized for single molecules, particularly emphasizing the highest resolution. Next to each parameter, the user will find explanations and recommendations. When the cursor hovers over the parameters, pop-up text bubbles provide further details. Users can adjust all parameters as desired. Importantly, the expansion factor should be set in accordance with the results obtained in the respective laboratories because this parameter is particularly important for obtaining the correct image scale. In addition, the temporal analysis mode should be adjusted in accordance with the type of experiment performed. For example, the temporal radiality pairwise product mean (TRPPM) analysis suits continuous and diffuse signals, while temporal radiality autocorrelation (TRAC) analysis is recommended for sparse labels and for colocalization studies requiring higher resolution. A TRAC order of 4 is preset for the analysis of single molecules because it provides the highest achievable resolution. For colocalization analysis, we recommend using the chromatic aberration correction function. The resulting images have an additional suffix of '_CAC' (for chromatic aberration corrected). Additional parameters are available in the advanced options tab, which can be used to accommodate various experimental paradigms with different SNR and signal quality. When acquiring zONE images, where image quality becomes noisier and the acquisition rate slows down because of imaging in multiple axial planes, users may choose to analyze the images using a lower TRAC order of 3 or 2. However, users should note that, while zONE allows the collection of information across a volume, this comes at the cost of reducing the achieved resolution because of hardware limitations. Lastly, we recommend that the users thoroughly read Supplementary Fig. 30, in which we present the software in graphic format, and Supplementary Figs. 1 and 2, in which the imaging and analysis flowcharts are shown.

Image analysis and statistics

For single-object analyses, such as synaptic vesicle or antibody analyses, signal intensities and distances between objects were analyzed manually using ImageJ (W. Rasband and contributors, National Institutes of Health). Line scans were also performed and analyzed using ImageJ. For the analysis of PSDs (Fig. 2), spots were identified by thresholding bandpass-filtered images, relying on empiric thresholds and bandpass filters, organized in the form of semiautomated routines in Matlab (version 2017b). Spots were overlaid to determine their overall signal distributions or their center positions were determined to measure distances between spots (in the same or different channels). The same procedure was used for the averaging analysis of CSF samples (Fig. 4) and for the analysis of spot distances for the GFP–Nb assemblies (Supplementary Figs. 15 and 16). Full width at half maximum values were measured after performing line scans over small but distinguishable spots (Supplementary Fig. 16), followed by Gaussian fitting using Matlab. The averaging analysis of $GABA_AR$s is presented in detail in the main text and was performed using Matlab. In brief, receptors were detected automatically as particles with intensities above an empirically derived threshold. To remove particles with uncompensated drift, we eliminated all receptors coming from images in which a large proportion of the particles were oriented similarly. We then visually inspected all of the remaining particles to choose those that appeared to be in a 'front view', showing a reasonably round appearance, with Nbs placed at the edges of the receptor (visible in the second color channel). All particles were centered on the intensity maxima of the respective $GABA_AR$ channel images. The particles were subjected to an analysis of the peaks of fluorescence, using a bandpass procedure, followed by identification of maxima[69]; the positions of the peaks were calculated to below-pixel precision and were rounded off to a pixel size of 0.384 nm (the starting pixel size was 1 nm). These positions were then mapped into one single matrix, which represents the 'averaged receptor', as indicated in the main text. Averaging analyses of actin were performed similarly. In brief, actin strands were selected manually and were overlaid to generate average views. Model objects were generated as a comparison by convoluting the amino acid positions in the respective Protein Data Bank (PDB) structures with empirically derived ONE spots. All of these analyses were performed using Matlab. The SNR for single Nbs was determined by measuring the average pixel intensities within the Nb spots and away from them and then dividing the two measurements. Identically sized circular regions of interest, sufficient to capture the Nb spots completely, were used for both signal and background (noise) regions. Plots and statistics were generated using GraphPad Prism 9.3.1 (GraphPad Software), SigmaPlot 10 (Systat Software) or Matlab. Statistical details are presented in the respective figure captions. Figures were prepared with CorelDraw 23.5 (Corel Corporation).

Optimization

Overview of critical steps in ONE microscopy. The gel preparation for ONE microscopy in classical ExM cell imaging closely follows the recommendations in the X10 guide, which we published several years ago[16]. Here, we highlight briefly the crucial steps for ONE microscopy, which include anchoring, homogenization and oxygen purging. Proper anchoring is vital for maintaining labeled targets and fluorescence signals. Effective homogenization prevents the rupture of cell compartments and enables the proper expansion of proteins. To troubleshoot this step, one may consider tuning the strength of the homogenization process by testing both autoclave and proteinase K protocols. Milder digestion methods, including short autoclave times (<60 min) or trypsin-based digestion (instead of proteinase K), could also be considered. Improper oxygen purging results in inconsistent sticky gels, with varying expansion factors that are hard to handle. For optimal results, the user should always add the reaction initiator KPS and the catalyst TEMED to the polymer solution in a rapid fashion and then the gel amount used (typically 70–80 µl for an 18-mm coverslip) should be sealed off with a coverslip within, at most, 70 s. When preparing more than five gels simultaneously, we suggest having two people perform this step side by side to minimize oxygen exposure. In the special case of single-molecule analyses, it is crucial to work only with a thin film of

fluid containing the molecules to be analyzed, to which the gel solution is quickly added. Please be aware that thin films of protein-containing buffers tend to dry very rapidly. An indicator of failure in this step is the appearance of salt and protein precipitates, looking as white clumps, which will be visible on the coverslip.

Imaging chamber optimization. All of the chamber blueprints and data are available in the Supplementary Information. For chamber usage, a gel slightly larger than the chamber should be cut, before removing excess water and fitting the gel onto the stabilizing net. Any overhanging gel should be trimmed away. The tight gel–chamber fit minimizes drift but automated drift correction in the ONE plugin is also available to address any residual drift before processing. It is automatically implemented and operates independently for each color channel. If the correction fails for one channel, it attempts to implement the drift correction coordinates from another channel. The interchannel drift correction feature is exclusive to line-by-line scanning and should not be used in frame-by-frame or stack-by-stack scan modes. Users suspecting postcorrection artifacts should sum the intensity of the entire drift-corrected raw video. Comet effects in the summed images indicate a drift correction failure, suggesting the need to discard such acquisitions. Drift correction issues often stem from dim or poorly labeled specimens or strong vibrations from an unstable imaging system.

Optimizing objective type selection. For targets in cells, which are close to the glass–gel interface, or single molecules, oil objectives with NA ≥ 1.4 should be used. For optimal imaging of single molecules, which are typically less than 1 µm in size when expanded, high-NA oil objectives should be used. Additionally, maintaining an imaging distance of ≤5 µm, by removing excess water between the gel and glass surfaces, is essential. To image cellular targets at higher depths accurately, it is crucial to address the refractive index mismatch. Using water-immersion objectives for deeper specimens is recommended to reduce artifacts.

Microscope selection. The user should consider the resolution needed and the type of specimen analyzed before settling on a particular microscope. In general, confocal microscopes are preferred. However, for general cellular imaging, epifluorescence microscopes are sufficiently accurate. Confocal microscopes offer higher resolution for single molecules and should be preferred for such uses. When using a confocal microscope, optimal results are achieved with the following detectors: HyD detectors, especially HyD X for its high quantum yield and SNR, or HyD R for near-infrared applications in photon counting mode (avoid analog and digital modes). Gallium arsenide phosphide and Avalanche photodiodes are also recommended. Classical photomultiplier tubes can be used at moderate voltage with a corrected smart offset to minimize dark counts to 1–5 per field of view.

Imaging conditions to avoid. During sample preparation, imaging single molecules from sticky gels or gels with cracks should be avoided, while ensuring that the expansion factor is corrected using known structures as rulers. For sample imaging, using noisy detectors with high dark counts should be avoided. Bidirectional scanners without manual phase shift correction should also be avoided. When processing images, users should be wary of artifactual airy disks caused by brightly labeled molecules that are partially out of focus. We suggest to opt for NHS-ester fluorescein over bright and stable modern dyes for labeling multimeric protein complexes, as bright parts of large complexes may get out of focus and lead to artifacts. The lower photon output of fluorescein reduces this problem.

Software considerations. The generated images have a 32-bit depth with negative values. These negative values represent noise and should be ignored. The users should set the dynamic display range to a zero-value minimum to exclude the noise. If gridded patterns appear in processed images, this may indicate low SNR, out-of-focus signals or incorrect bidirectional line scanning. Such images should be discarded. One can troubleshoot this by optimizing the labeling and the fluorophore selection and/or by adjusting the pixel dwell time and detector sensitivity.

3D model reconstruction

To prepare the ONE images for suitable 3D model reconstruction, we applied automated thresholding algorithms to extract dense areas of intensity, in which the expected protein should be located. The extracted areas have a window size of 200 × 200 pixels. The next step involved deconvolving the images using the Lucy–Richardson[70] method with 80 iterations and a Gaussian PSF kernel of size 13 × 13 and $\sigma = 2$. Subsequently, the images were normalized to a range of 0–8 and then scaled down using bilinear interpolation to dimensions of 128 × 128 pixels. The processed images were transferred into cryoFIRE, an unsupervised ab initio autoencoder for complex shape reconstruction with amortized inference[35]. cryoFIRE consists of two components, the encoder f_{enc} and decoder f_{dec}. The encoder contains convolutional followed by fully connected layers. It takes a processed ONE image Y_i and estimates its pose R_i, translation t_i, expansion factor e_i and molecule confirmation z_i (that is, $f_{\text{enc}}(Y_i) = (R_i, t_i, e_i, z_i)$). Here, e_i was added to the original cryoFIRE approach to account for mild variations in the expansion factor between different gels. The decoder, a coordinate-based multilayer perceptron, represents the protein structure implicitly. For a given 3D coordinate, its output represents the density of the protein at this location. The decoder gets a 2D grid of coordinates, centered at the origin, which gets rotated and scaled by (R_i, e_i); therefore, the predicted image is $\hat{Y}_{k_x,k_y} = f_{\text{dec}}(z_i, e_i \cdot R_i \cdot (k_x, k_y, 0)^T)$ with $(k_x, k_y) \in R^2$. This prediction is then shifted by t_i to move it back to the original position. Because the predicted output represents a 2D central slice of the molecule in the Hartley domain, to compare the prediction $\hat{Y}$ to the input Y, it also needs to be transformed into the Hartley domain. Because of the deconvolution in the preprocessing step, we did not need to apply a contrastive transfer function to the prediction, as proposed in cryoFIRE. With the modified (symmetric) mean squared error loss, which takes account of the handedness of the protein, the parameters are optimized using stochastic gradient descent. The 3D reconstructed images can be inspected with UCSF ChimeraX. The computation and processing were hosted by the Norddeutscher Verbund für Hoch- und Höchstleistungsrechnen servers (https://hlrn.de/).

Reporting summary

Further information on research design is available in the Nature Portfolio Reporting Summary linked to this article.

Data availability

Image data are available from the corresponding authors on reasonable request. Source data are provided with this paper.

Code availability

The ONE platform plugin software (source code) is available from Zenodo (https://doi.org/10.5281/zenodo.13685267)[71].

References

47. Torres-Garcia, E. et al. Extending resolution within a single imaging frame. *Nat. Commun.* **13**, 7452 (2022).
48. Shannon, C. E. Communication in the presence of noise. *Proc. IRE* **37**, 10–21 (1949).
49. Wu, Y. et al. Resonant scanning with large field of view reduces photobleaching and enhances fluorescence yield in STED microscopy. *Sci Rep.* **5**, 14766 (2015).

50. Dubois, B. et al. Research criteria for the diagnosis of Alzheimer's disease: revising the NINCDS–ADRDA criteria. *Lancet Neurol.* **6**, 734–746 (2007).
51. Gibb, W. R. Accuracy in the clinical diagnosis of parkinsonian syndromes. *Postgrad. Med. J* **64**, 345–351 (1988).
52. McKeith, I. et al. Dementia with Lewy bodies. *Lancet Neurol.* **3**, 19–28 (2004).
53. Gerdes, C. et al. A nanobody-based fluorescent reporter reveals human α-synuclein in the cell cytosol. *Nat. Commun.* **11**, 2729 (2020).
54. Pullara, F. et al. A general path for large-scale solubilization of cellular proteins: from membrane receptors to multiprotein complexes. *Protein Expr. Purif.* **87**, 111–119 (2013).
55. Aricescu, A. R., Lu, W. & Jones, E. Y. A time- and cost-efficient system for high-level protein production in mammalian cells. *Acta Crystallogr. D Biol. Crystallogr.* **62**, 1243–1250 (2006).
56. Elegheert, J. et al. Lentiviral transduction of mammalian cells for fast, scalable and high-level production of soluble and membrane proteins. *Nat. Protoc.* **13**, 2991–3017 (2018).
57. Masiulis, S. et al. GABAA receptor signalling mechanisms revealed by structural pharmacology. *Nature* **565**, 454–459 (2019).
58. Uchanski, T. et al. Megabodies expand the nanobody toolkit for protein structure determination by single-particle cryo-EM. *Nat. Methods* **18**, 60–68 (2021).
59. Nakane, T. et al. Single-particle cryo-EM at atomic resolution. *Nature* **587**, 152–156 (2020).
60. Zheng, S. Q. et al. MotionCor2: anisotropic correction of beam-induced motion for improved cryo-electron microscopy. *Nat. Methods* **14**, 331–332 (2017).
61. Rohou, A. & Grigorieff, N. CTFFIND4: fast and accurate defocus estimation from electron micrographs. *J. Struct. Biol.* **192**, 216–221 (2015).
62. Tegunov, D. & Cramer, P. Real-time cryo-electron microscopy data preprocessing with Warp. *Nat. Methods* **16**, 1146–1152 (2019).
63. Punjani, A., Rubinstein, J. L., Fleet, D. J. & Brubaker, M. A. cryoSPARC: algorithms for rapid unsupervised cryo-EM structure determination. *Nat. Methods* **14**, 290–296 (2017).
64. Perego, E. et al. A minimalist model to measure interactions between proteins and synaptic vesicles. *Sci Rep.* **10**, 21086 (2020).
65. Saal, K. A. et al. Heat denaturation enables multicolor X10-STED microscopy at single-digit nanometer resolution. *Sci. Rep.* **13**, 5366 (2023).
66. Park, H. E. et al. Scalable and isotropic expansion of tissues with simply tunable expansion ratio. *Adv. Sci. (Weinh.)* **6**, 1901673 (2019).
67. Abraham, M. J. et al. GROMACS: high performance molecular simulations through multi-level parallelism from laptops to supercomputers. *SoftwareX* **1–2**, 19–25 (2015).
68. Horn, H. W. et al. Development of an improved four-site water model for biomolecular simulations: TIP4P-Ew. *J. Chem. Phys.* **120**, 9665–9678 (2004).
69. Sousa da Silva, A. W. & Vranken, W. F. ACPYPE—Antechamber Python parser interface. *BMC Res. Notes* **5**, 367 (2012).
70. Li, K. The image stabilizer plugin for ImageJ. http://www.cs.cmu.edu/~kangli/code/Image_Stabilizer.html (2008).
71. Alawieh, M. M. ONE Microscopy Java plugin source code. *Zenodo* https://doi.org/10.5281/zenodo.13685267 (2024).

Acknowledgements

We thank C. Zeising, G. Klaehn, A.-K. Jaehnke and J. Hentze (University Medical Center Göttingen) and U. Schwarz (Leica Microsystems) for excellent technical assistance. We thank A. Kassem for driver debugging and integration. We thank S. W. Hell (Max Planck Institute for Multidisciplinary Sciences) for encouragement with this project. We thank A. Triller (École Normale Supérieure) for initial input on the PSD95 data. We acknowledge the University of Massachusetts Medical School Sanderson Center for Optical Experimentation Core Facility (RRID: SCR_022721), Massachusetts Life Sciences Center and C. Baer for assistance with imaging. We thank N. Brose (Max Planck Institute for Multidisciplinary Sciences) for help with access to his fluorescence microscopy facility. We thank M. Krone (Max Planck Institute for Multidisciplinary Sciences) and F. Kötting (European Neuroscience Institute) for their support in building the gel stabilization chambers. We thank T. C. Cheng and H. Hillen (University Medical Center Göttingen) for their advice relating to Fourier shell correlation methods and analyses. We thank E. Fornasiero and C. Tetzlaff (University Medical Center Göttingen) and G. B. Rizzoli for comments on the initial manuscript. The work was supported by grants from the German Ministry for Education and Research (13N15328/NG-FLIM) and the German Research Foundation (Deutsche Forschungsgemeinschaft, DFG; SFB1286/A03/B02/C06/Z04, SFB1190/P09, RI1967/10-1 (NeuroNex) and GRK 2824 to S.O.R.), the European Research Council under the European Union's Horizon 2020 research and innovation program (grant nos. 835102 and 964016) and the DFG under Germany's Excellence Strategy (EXC 2067/1-390729940). Funding from the Chan Zuckerberg Initiative (CZI), grant iNano (2023-321180(5022)GB-1586232 to S.O.R.), and support from the DFG (grant SFB894/A9 to U.B.) and the UK Medical Research Council (grants MR/L009609/1, MC_EX_MR/T046279/1 and MC_UP_1201/15 to A.R.A.) are also acknowledged. R.C. is supported by a fellowship from the Alexander von Humboldt Foundation. E.S.B. acknowledges HHMI, L. Yang, L. McGovern, J. Doerr, Good Ventures, NIH 1R01EB024261, NIH 1R01AG070831, T. Stocky and A. Shah, K. Octavio, and ERC Synergy grant no. 835102. We also gratefully acknowledge the computing time granted by the Resource Allocation Board and provided on the supercomputer Lise and Emmy at NHR@ZIB and NHR@Göttingen as part of the NHR infrastructure. The calculations for this research were conducted with computing resources under the projects nim00007 and nip00062.

Author contributions

A.H.S. and S.O.R. conceptualized the project. A.A.C. and U.B. developed the ONE Platform plugin, which was supported for driver compatibility by M.M.A. A.H.S. and S.O.R. designed and performed the experiments. U.B. supervised the ONE experiments at the Center for Integrative Physiology and Molecular Medicine (CIPMM). J.A. and A.A.C. implemented the deep learning algorithms for 3D reconstructions under the supervision of A.H.S., C.P. and S.O.R. E.S.B. supervised the ONE experiments at MIT. S.K. supervised T. Mimoso's ONE experiments at the Institute for X-Ray Physics. M.S. supervised the ONE experiments at Würzburg University. A.H.S., V.I. and S.O.R. analyzed the data. R.C., N.M., P.F. and S.V.G. contributed to reproducing the ONE experiments. C.Z. performed the ONE experiments at MIT. J.K. contributed to the bassoon in tissues experiment. N.A. and U.B. performed the ONE experiments at the CIPMM. M.M., H.C. and J.P. purified otoferlin protein. H.C. and T.M. generated the otoferlin AlphaFold model. D.M. and A.R.A. generated the $GABA_A$Rs and the cryo-EM data. S.R. purified calmodulin protein. A.H.S. and D.K. performed the mCLING experiments and the mCLING simulation was performed by R.K.W.S., A.S. and M.M. J.E. performed the ONE experiments at Würzburg University. R.C. and L.A. contributed to the experiments at Leica. F.O. generated the TSRs. D.C. generated the tissue sections. K.A.S. assisted with the initial implementation of X10ht experiments. C.T. and B.M. provided the CSF specimens from participants. T.F.O. verified the analysis of PD data. M.S. contributed to the understanding of photophysics fluctuations and E.S.B. contributed to the understanding of ExM gel behavior. S.O.R. wrote the manuscript, which was revised by all other authors, with especially strong contributions from A.H.S., A.R.A., M.S. and E.S.B.

Competing interests

S.O.R. and F.O. are shareholders of NanoTag Biotechnologies GmbH. E.S.B. is an inventor on multiple patents related to ExM and co-founder of a company working on commercial applications of ExM. The other authors declare no competing interests.

Ethics statement

Animals (Wistar rats, P0–P1) were treated according to the regulations of the local authority, the Lower Saxony State Office for Consumer Protection and Food Safety (Niedersächsisches Landesamt für Verbraucherschutz und Lebensmittelsicherheit), under the license Tötungsversuch T09/08. The informed consent of all of participants was obtained at the Paracelsus Elena Klinik, following the principles of the Declaration of Helsinki.

Additional information

Supplementary information The online version contains supplementary material available at https://doi.org/10.1038/s41587-024-02431-9.

Correspondence and requests for materials should be addressed to Ali H. Shaib or Silvio O. Rizzoli.

Peer review information *Nature Biotechnology* thanks Alberto Diaspro and the other, anonymous, reviewer(s) for their contribution to the peer review of this work.

nature portfolio

Corresponding author(s): Ali Shaib and Silvio Rizzoli

Last updated by author(s): Sep 5, 2024

Reporting Summary

Nature Portfolio wishes to improve the reproducibility of the work that we publish. This form provides structure for consistency and transparency in reporting. For further information on Nature Portfolio policies, see our Editorial Policies and the Editorial Policy Checklist.

Statistics

For all statistical analyses, confirm that the following items are present in the figure legend, table legend, main text, or Methods section.

n/a	Confirmed
☐	☒ The exact sample size (*n*) for each experimental group/condition, given as a discrete number and unit of measurement
☐	☒ A statement on whether measurements were taken from distinct samples or whether the same sample was measured repeatedly
☐	☒ The statistical test(s) used AND whether they are one- or two-sided *Only common tests should be described solely by name; describe more complex techniques in the Methods section.*
☐	☒ A description of all covariates tested
☐	☒ A description of any assumptions or corrections, such as tests of normality and adjustment for multiple comparisons
☐	☒ A full description of the statistical parameters including central tendency (e.g. means) or other basic estimates (e.g. regression coefficient) AND variation (e.g. standard deviation) or associated estimates of uncertainty (e.g. confidence intervals)
☐	☒ For null hypothesis testing, the test statistic (e.g. *F*, *t*, *r*) with confidence intervals, effect sizes, degrees of freedom and *P* value noted *Give P values as exact values whenever suitable.*
☒	☐ For Bayesian analysis, information on the choice of priors and Markov chain Monte Carlo settings
☒	☐ For hierarchical and complex designs, identification of the appropriate level for tests and full reporting of outcomes
☐	☒ Estimates of effect sizes (e.g. Cohen's *d*, Pearson's *r*), indicating how they were calculated

Our web collection on statistics for biologists contains articles on many of the points above.

Software and code

Policy information about availability of computer code

Data collection	Data was acquired using Leica Application Suite for SP5 version 1.6 and SP8 version 3.5.7.23225, STELLARIS 8 version 4.7.0.28176, Abberior Instruments Imspector v16.3 and Olympus CellSens Dimension 2.3.
Data analysis	Custom code written in Matlab2017b and 2019b, ImageJ versions 1.53j and 1.54f, GraphPad Prism 9, SigmaPlot 10 and Excel 2022.

For manuscripts utilizing custom algorithms or software that are central to the research but not yet described in published literature, software must be made available to editors and reviewers. We strongly encourage code deposition in a community repository (e.g. GitHub). See the Nature Portfolio guidelines for submitting code & software for further information.

Data

Policy information about availability of data

All manuscripts must include a data availability statement. This statement should provide the following information, where applicable:

- Accession codes, unique identifiers, or web links for publicly available datasets
- A description of any restrictions on data availability
- For clinical datasets or third party data, please ensure that the statement adheres to our policy

Image data are available from the corresponding authors on reasonable request.

Research involving human participants, their data, or biological material

Policy information about studies with human participants or human data. See also policy information about sex, gender (identity/presentation), and sexual orientation and race, ethnicity and racism.

Reporting on sex and gender	Fourteen human participants (male, female) were involved in this study, seven of which were diagnosed with Parkinson's disease and the other seven patients served as neurological controls and have been diagnosed with a variety of non-neurodegenerative disorders.
Reporting on race, ethnicity, or other socially relevant groupings	No reporting on race, ethnicity, or other socially relevant groupings.
Population characteristics	The age of participants carried from 76.7 ± 2.3 years and 72.0 ± 2.9 years and more details about the population characteristics that include age, sex, and diagnosis is available in the manuscript, see Supplementary Table 1.
Recruitment	Patients were in treatment at the Paracelsus Elena Klinik, Kassel, Germany.
Ethics oversight	The informed consent of all of the participants was obtained at the Paracelsus Elena Klinik, following the principles of the Declaration of Helsinki.

Note that full information on the approval of the study protocol must also be provided in the manuscript.

Field-specific reporting

Please select the one below that is the best fit for your research. If you are not sure, read the appropriate sections before making your selection.

☒ Life sciences ☐ Behavioural & social sciences ☐ Ecological, evolutionary & environmental sciences

For a reference copy of the document with all sections, see nature.com/documents/nr-reporting-summary-flat.pdf

Life sciences study design

All studies must disclose on these points even when the disclosure is negative.

Sample size	The largest possible numbers of experiments were performed, taking into account the high number of different experimental settings, and is well within the range of typical imaging experiments. No formal sample size calculation was performed.
Data exclusions	No experiments or data points were excluded (unless stated in figure legends).
Replication	In general 2 to 5 independent experiments were performed (experimental N is indicated for every dataset in the figure legends, with tens or hundreds of items (molecules, purified proteins, protein assemblies, synapses, synaptic structures, etc.) analyzed. All replications were successful. For expanded samples, each experimental N encompassed from 2 and up to 4 gel replicates.
Randomization	Not relevant for this manuscript.
Blinding	Most analyses relied on automated procedures which are not influenced by the nature of the sample. Blind analysis was applied when meaningful for the manual analysis and for the calmodulin experiment of which image acquisition was carried out blindly as well. Parkinson's disease data were imaged blindly and the analysis was performed by two independent investigators using two different image processing paradigms which was in agreement with automated script results using Matlab.

Reporting for specific materials, systems and methods

We require information from authors about some types of materials, experimental systems and methods used in many studies. Here, indicate whether each material, system or method listed is relevant to your study. If you are not sure if a list item applies to your research, read the appropriate section before selecting a response.

Materials & experimental systems

n/a	Involved in the study
☐	☒ Antibodies
☐	☒ Eukaryotic cell lines
☒	☐ Palaeontology and archaeology
☐	☒ Animals and other organisms
☒	☐ Clinical data
☒	☐ Dual use research of concern
☒	☐ Plants

Methods

n/a	Involved in the study
☒	☐ ChIP-seq
☒	☐ Flow cytometry
☒	☐ MRI-based neuroimaging

Antibodies

Antibodies used

FluoTag-X2 anti-PSD95 anti-PSD95, clone 1B2, #N3702, NanoTag Biotechnologies, Göttingen, Germany, dilution 1:1000.
FluoTag-X2 anti-ALFA nanobody, Cat#N1502, NanotTag GmbH, Göttingen, Germany, dilution 1:500.
Alpha-Synuclein, Nb2, NanoTag Biotechnologies, Göttingen, Germany, dilution 1:200.
Alpha-Synuclein antibody, Synaptic Systems Cat#128 211, Göttingen, Germany, dilution 1:500.
Alpha/beta-Synuclein antibody, Synaptic Systems Cat#128 002, Göttingen, Germany, dilution 1:500.
GABAaR nanobody, Nb25, NanoTag Biotechnologies, Göttingen, Germany dilution : 20 µl of 10 µM Nb25-STAR635P was added to the sample prior to the elution step.
Rabbit alpha-Tubulin Abcam, Cat#ab18251, Cambridgshire, UK, dilution 1:1000.
Mouse alpha-Tubulin Sigma Cat#T6199; Sigma-Aldrich, Darmstadt, Germany, dilution 1:1000.
Rabbit alpha Tubulin Synaptic Systems Cat#302 203, Göttingen, Germany, dilution 1:1000.
Mouse alpha Tubulin Synaptic Systems Cat#302 211; Göttingen, Germany, dilution 1:1000.
Mouse Bassoon, #ADI-VAM-PS003-F, Enzo Life Sciences GmbH, Lörrach, Germany, dilution 1:500.
Abberior Star635P, Cat#ST635P-1001, Abberior, Göttingen, Germany, dilution 1:1000.
Abberior Star635P, Cat#ST635P-1002-500UG, Abberior, Göttingen, Germany, dilution 1:1000.

Validation

FluoTag-X2 anti-PSD95 anti-PSD95, clone 1B2, #N3702, NanoTag Biotechnologies GmbH, validated by NanoTag, see: https://nano-tag.com/product/fluotag-x2-anti-psd95/
FluoTag-X2 anti-ALFA nanobody, Cat#N1502, NanotTag GmbH, Göttingen, Germany; validated by NanoTag, see: https://nano-tag.com/product/fluotag-x2-anti-alfa/, and recently cited by Saal et la., 2022 - BioRxivs.
Alpha-Synuclein 2 nanobody, NanoTag GmbH, Göttingen, Germany; validated by: De Genst et al., 2010 - J Mol Biol.
Alpha-Synuclein antibody, Synaptic Systems Cat#128 211, Göttingen, Germany; recently validated by: Vinueza-Gavilanes et al., 2020 - Neurobiology of Disease.
Alpha/beta-Synuclein antibody, Synaptic Systems Cat#128 002, Göttingen, Germany; validated 13 times including Wilhelm et al., 2014 - Science, and Chandra,... Südhof, 2003 - J Biol Chem.
GABAaR nanobody, NanoTag GmbH, Göttingen, Germany; validated by NanoTag and A. Radu Aricescu lab, see: Miller et al., 2017 - Nat Struct Mol Biol.
Rabbit alpha-Tubulin Abcam, Cat#ab18251, Cambridgshire, UK; validation in 286 citations, Berbari et al., 2012 - Cytoskeleton.
Mouse alpha-Tubulin Sigma Cat#T6199; Sigma-Aldrich, Darmstadt, Germany; validated in 105 citations, recent validation: Latremoliere et al., 2018 - Cell Rep.
Rabbit alpha Tubulin Synaptic Systems Cat#302 203, Göttingen, Germany; 4 citations, Wilhelm et al., 2014 - Science.
Mouse alpha Tubulin Synaptic Systems Cat#302 211; Göttingen, Germany; 15 citations, Groffen et al., 2010 - Science.
Mouse Bassoon, #ADI-VAM-PS003-F, Enzo Life Sciences GmbH, Lörrach, Germany; validated 73 times, most recent: Yamamoto et al., 2022 - Cell Biol.

Eukaryotic cell lines

Policy information about cell lines and Sex and Gender in Research

Cell line source(s)

U2OS cell line from Cell Lines Service (CLS), Eppelheim, Germany.
HEK 293T, Thermo Scientific, #HCL4517, Germany.

Authentication

STR analysis according to the global standard ANSI/ATCC ASN-0002.1-2021 (2021) resulted in an authentic STR profile of the reference STR database - confirmed by the company.

Mycoplasma contamination

Both lines are negative in PCR assay - confirmed by the companies.

Commonly misidentified lines
(See ICLAC register)

Not listed in the ICLAC database.

Animals and other research organisms

Policy information about studies involving animals; ARRIVE guidelines recommended for reporting animal research, and Sex and Gender in Research

Laboratory animals	Rattus norvegicus, Wistar, P0 to P1 pups.
Wild animals	None
Reporting on sex	Both sexes
Field-collected samples	none
Ethics oversight	All animals were handled according to the specifications of the University of Gbttingen and of the local authority, the State of Lower Saxony (Landesamt fur Verbraucherschutz, LAVES, Braunschweig, Germany). All animal experiments were approved by the local authority, the Lower Saxony State Office for Consumer Protection and Food Safety (Niedersachsisches Landesamt fur Verbraucherschutz und Lebensmittelsicherheit).

Note that full information on the approval of the study protocol must also be provided in the manuscript.

Plants

Seed stocks	Not relevant for this study.
Novel plant genotypes	Not relevant for this study.
Authentication	Not relevant for this study.

nature biotechnology

Supplementary information

https://doi.org/10.1038/s41587-024-02431-9

One-step nanoscale expansion microscopy reveals individual protein shapes

In the format provided by the authors and unedited

Supplementary Information

Table of contents

Supplementary Figures

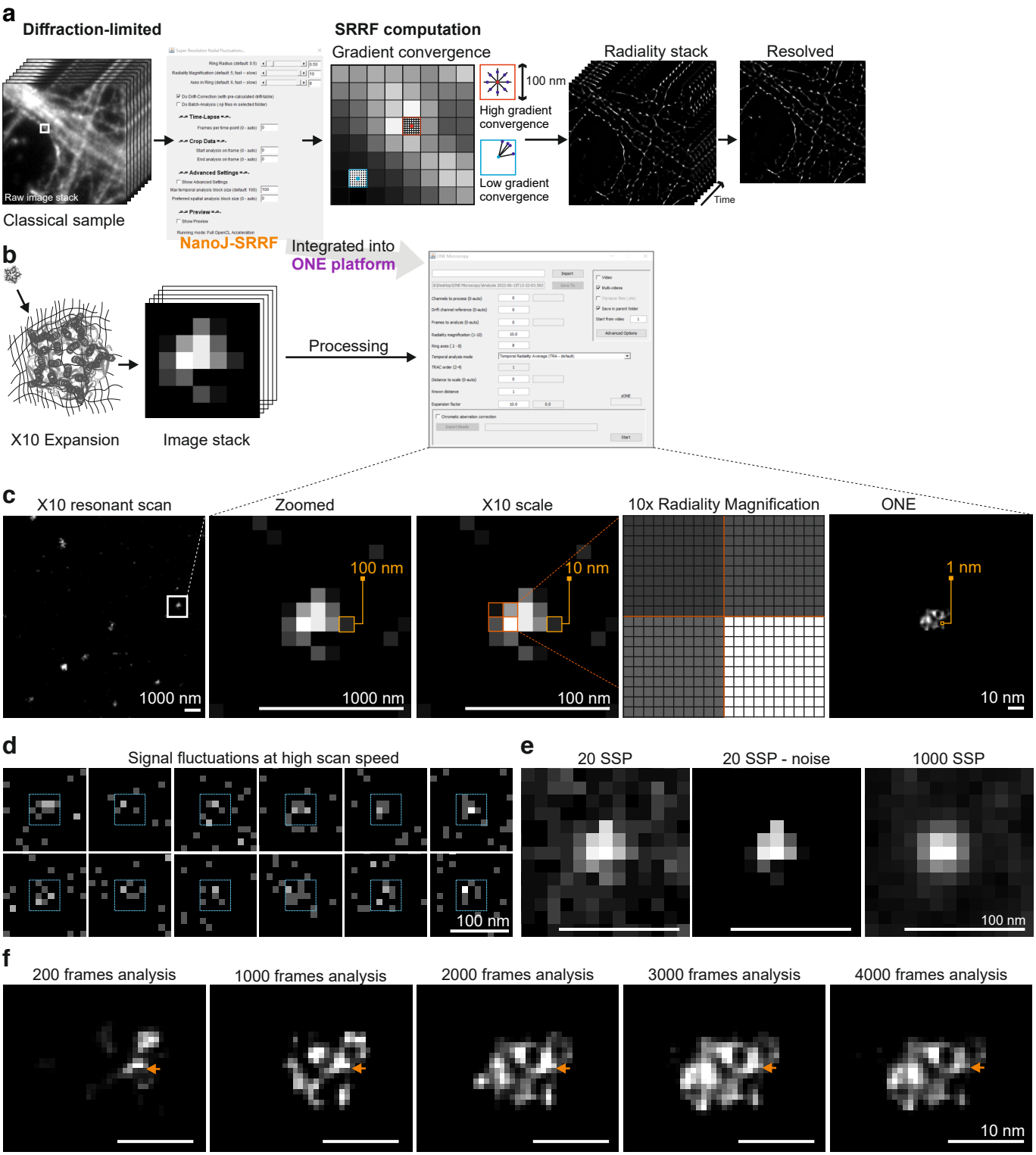

Supplementary Fig. 1. A detailed view of the ONE procedure. a, Processing a stack of diffraction-limited images with SRRF, based on the analysis of a gradient of convergence of sub-pixels over a radiality stack, results in super-resolved images with resolutions varying between 50-70 nm. **b**, The ONE procedure adapts the SRRF algorithm to expanded gels. **c-f**, A detailed explanation of the analysis procedure. **c**, A sample was fixed and expanded using a 10-fold expansion protocol (X10). The sample was then imaged using a resonant scanner on a confocal microscope. The zoomed-in view indicates one bright spot, whose size in real space is limited by diffraction to ~200-300 nm, but represents a 10-fold smaller size in the pre-expansion space (see scale bars in the middle panels). Every pixel is then subjected to a 10-fold radiality magnification and is then subjected to the procedure explained in panels d-f, which provides the final, high-resolution image (right-most panel). **d**, Signal fluctuations are measured by imaging the sample repeatedly, using the resonant scanner (here at 8 kHz). **e**, A view of the overall signals, obtained by summing 20 of the fluctuating images (raw in the left-most panel, background-subtracted in the middle panel), or by summing 1000 images. **f**, Each image from series obtained as in panel b is subjected to a temporal analysis of fluctuating fluorophores, based on radiality magnification, thereby providing a super-resolved image whose level of detail becomes optimal after ~1500 frames. These results are typical of 753 images acquired from 5 independent experiments.

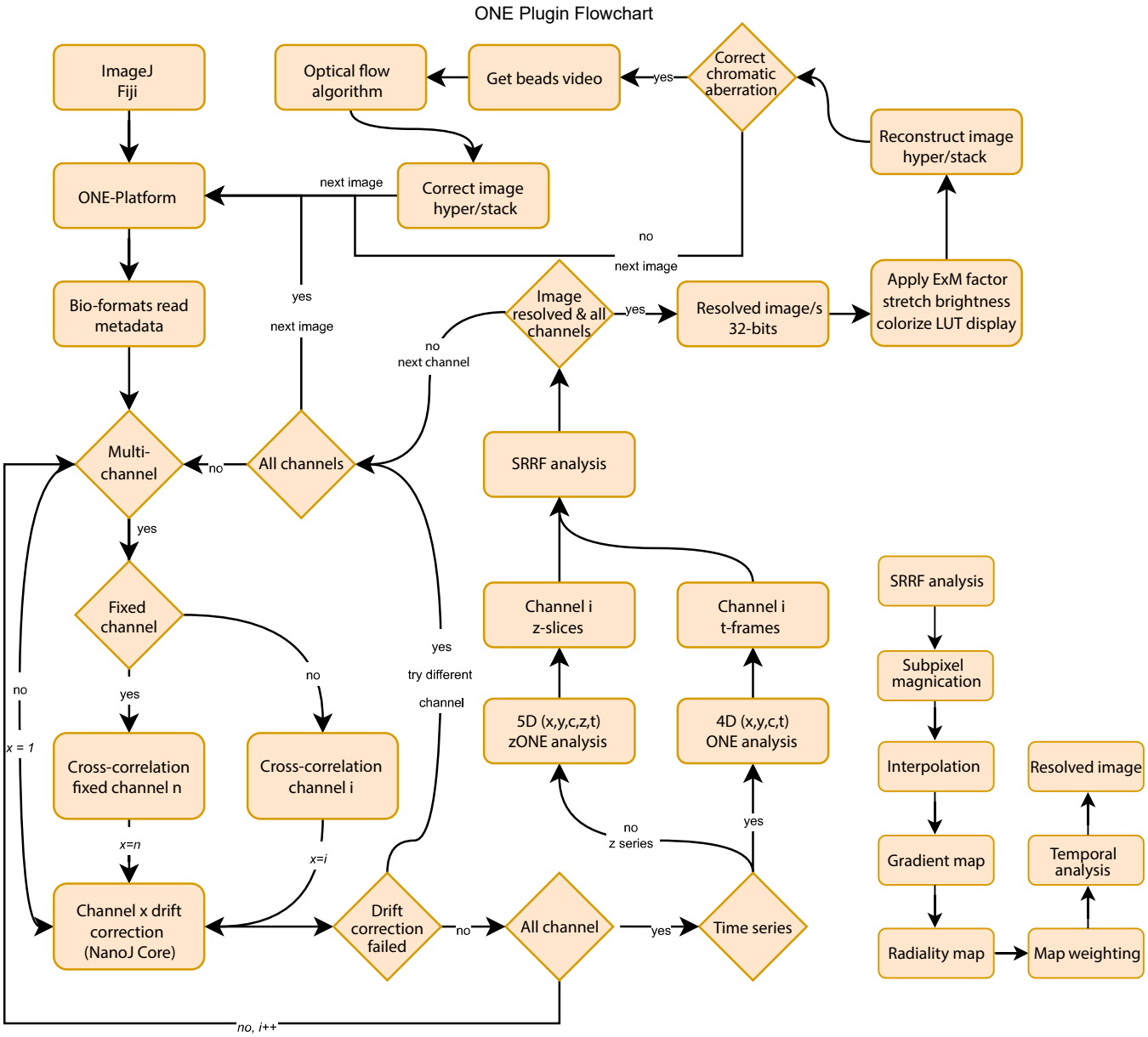

Supplementary Fig. 2. ONE plugin flowchart. ONE platform is a JAVA-based plugin for Fiji. ONE platform is capable of reading any image format with up to 5-dimension information (x,y,z,c,t) in batch analysis mode. After applying automatic drift correction, NanoJ core is called for SRRF analysis. The platform corrects for expansion factors and chromatic aberration. The processed data is stored in separate folders carrying the image ID name.

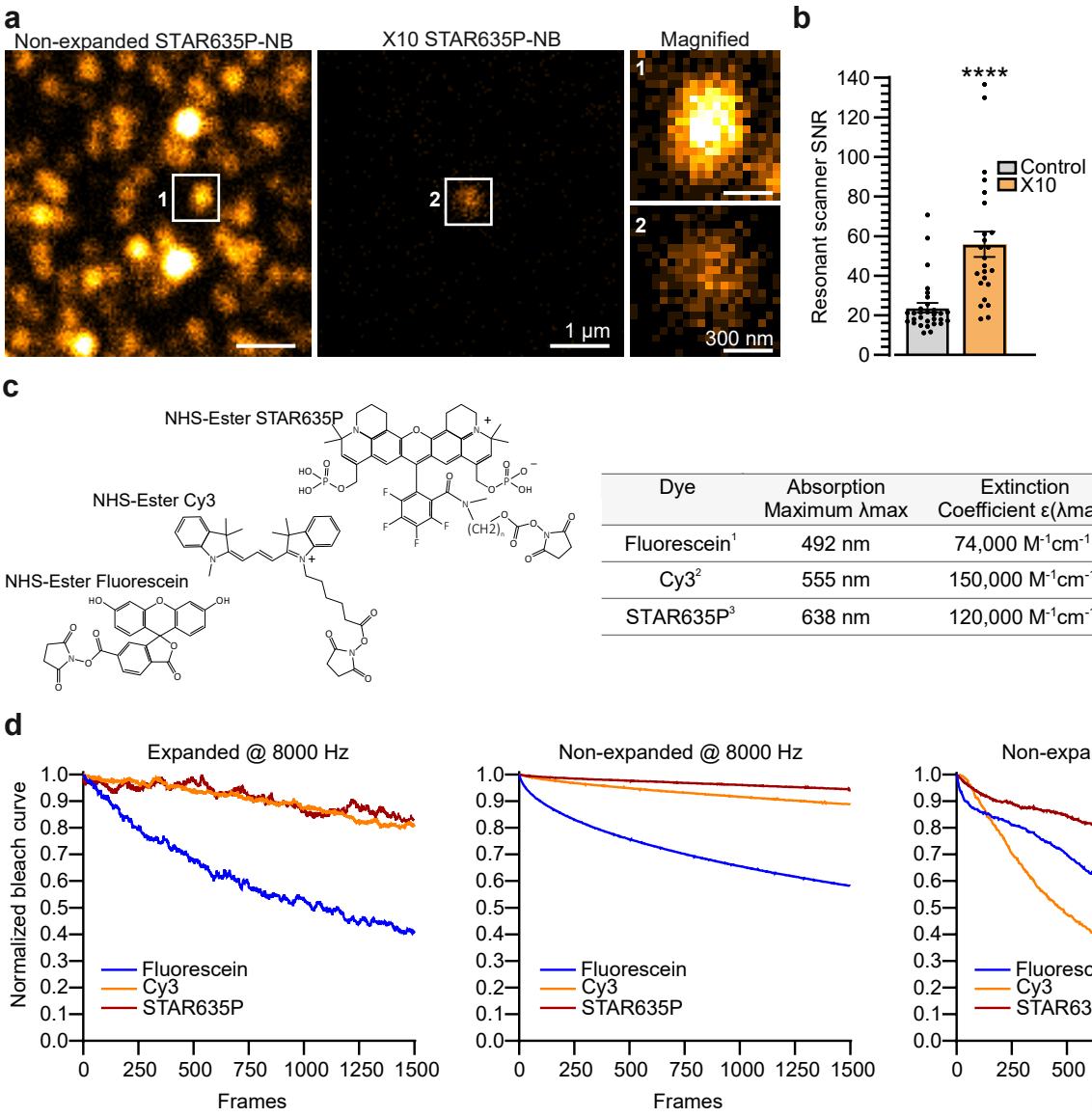

Dye	Absorption Maximum λmax	Extinction Coefficient ε(λmax)	Quantum Yield η
Fluorescein[1]	492 nm	74,000 $M^{-1}cm^{-1}$	0.90
Cy3[2]	555 nm	150,000 $M^{-1}cm^{-1}$	0.31
STAR635P[3]	638 nm	120,000 $M^{-1}cm^{-1}$	0.90

Supplementary Fig. 3. Expansion microscopy results in a higher signal-to-noise ratio. Expansion microscopy, which separates proteins of interest and removes much of the other cellular components (*e.g.* lipids, metabolites) should result in a higher signal-to-noise ratio (SNR). **a**, To test this, we analyzed here the simplest possible sample, consisting of Star635P-conjugated nanobodies on glass coverslips, or in expanded gels, using confocal microscopy, relying on analysis using a resonant scanner. **b**, The SNR of these samples displayed as an average bar graph with standard error of mean, increases by 2-fold, on average, after expansion. N = 30-24, from 3 independent measurements. *P* = 0.000001, Two-tailed Mann-Whitney Ranksum test. **c**, Bleaching properties of fluorescein, Cy3, and STAR635P. A representation of the structures of each of the used dyes, followed by a table of their properties. The molecule structures and properties were reproduced from measurements of commercial providers: [1]https://broadpharm.com/product/bp-23900, [2]https://broadpharm.com/product/bp-22535, and [3]https://abberior.shop/abberior-STAR-635P. **d**, Normalized bleach curves from expanded specimens at 8000 Hz, and non-expanded specimens at 8000 Hz and 200 Hz.

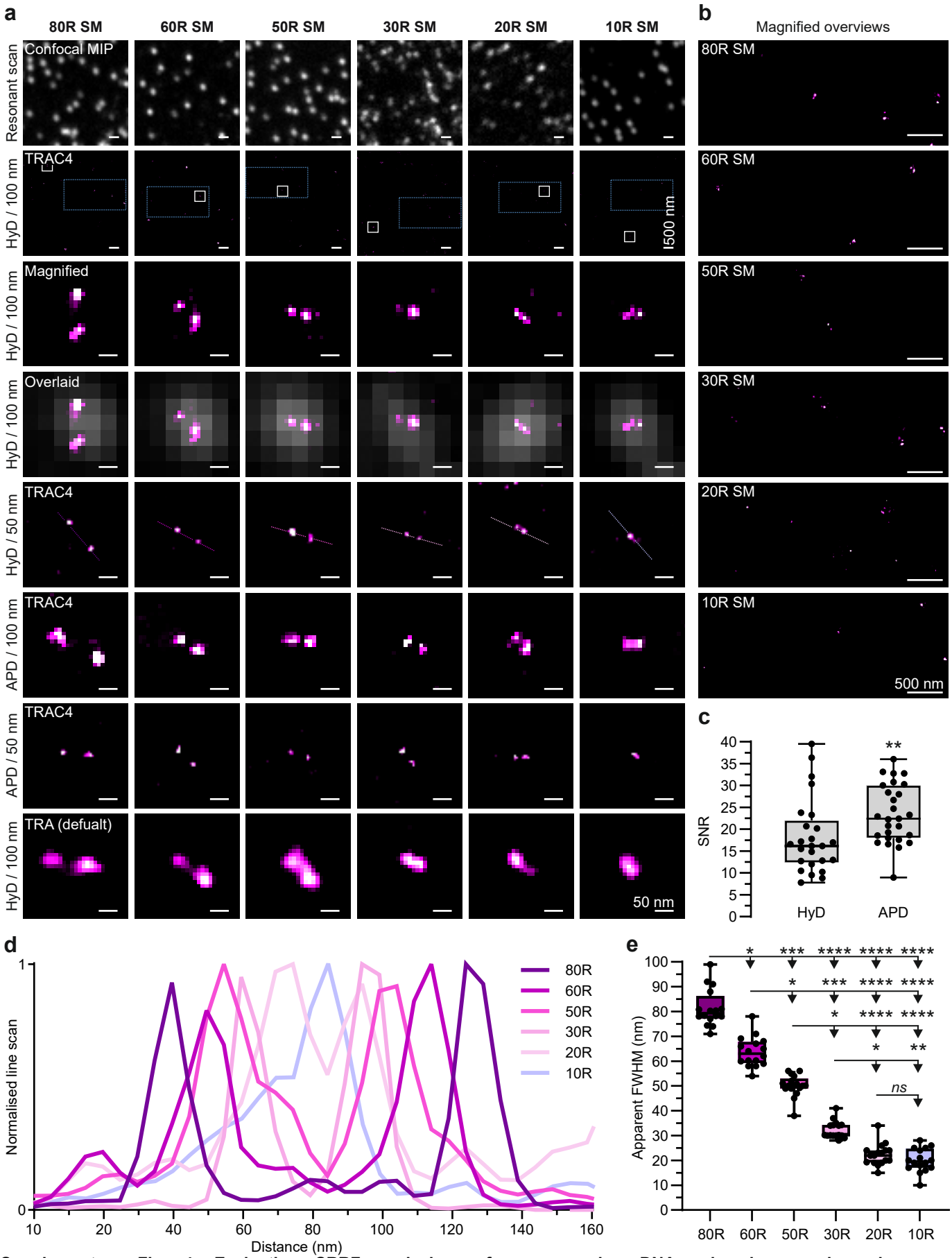

Supplementary Fig. 4. Evaluating SRRF analysis performance using DNA origami nanorulers, in non-expanded samples. **a**, Nanorulers with single Atto647N molecules (R SM) were generated by GATTAquant carrying fluorophores on each end of DNA structures of 80, 60, 50, 30, 20 and 10 nm in length. ...

... They were then imaged using a confocal resonant scanner, without expansion procedures. The first panel shows confocal maximal intensity projections (MIPs) for each of the rulers. The second panel shows temporal radiality averaging (TRA) analysis overviews. White boxes indicate the magnified regions displayed in the third panel. The fourth panel shows a temporal radiality auto-correlations of fourth order (TRAC4) analysis, overlaid with the respective confocal MIPs. The remaining panels show different ruler examples, acquired at different starting pixel sizes, using either a hybrid detector (HyD) or an avalanche photodiode detector (APD), and analyzed in different SRRF modalities. This analysis is shown in the fifth panel for 50 nm pixel size, using a HyD and analyzed using TRAC4. The sixth and seventh panels show rulers acquired at 100 and 50 nm pixel sizes, using an APD and analyzed using TRAC4. The eighth panel shows rulers that were acquired at 100 nm pixel size and were analyzed using default SRRF settings (TRA). **b**, Magnified overviews of selected regions (indicated by blue rectangles) from each of the ruler exemplary images to the left. **c**, Signal-to-noise ratio (SNR) box plot analysis showing mean, minimum and maximum whiskers of HyD and APD detectors, $N_{nanorulers}$ = 25 and 30 independent measurment for HyD and APD, respectively. Two-tailed Mann Whitney test, p = 0.004. **d**, Normalized line scans across the different ruler images, as indicated in the respective panels in (**a**). **e**, Apparent FWHM of the different rulers. N = 17, 17, 18, 17, 18 and 17 for 80, 60, 50, 30, 20, and 10 R SM DNA origami nanoruler, respectively. Three independent measurements were carried out A Kruskal-Wallis test was applied, followed by Dunn's *post hoc* test; p values for 80R vs. 60R, 50R, 30R, 20R and 10R = 0.0367, 0.0006, <0.0001, <0.0001, and <0.0001, respectively. p values for 60R vs. 50R, 30R, 20R and 10R = 0.031, 0.0004, <0.0001 and <0.0001, repectively. p values for 50R vs. 30R, 20R and 10R = 0.0286, <0.0001 and <0.0001, respectively. p values for 30R vs. 20R and 10R = 0.0121 and 0.004, respectively. p value of R20 vs. R10 = 0.1757. p values > 0.05 not significant (*ns*), $p \leq 0.05$: *, $p \leq 0.01$ **, $p \leq 0.001$ ***, $p \leq 0.0001$ ****.

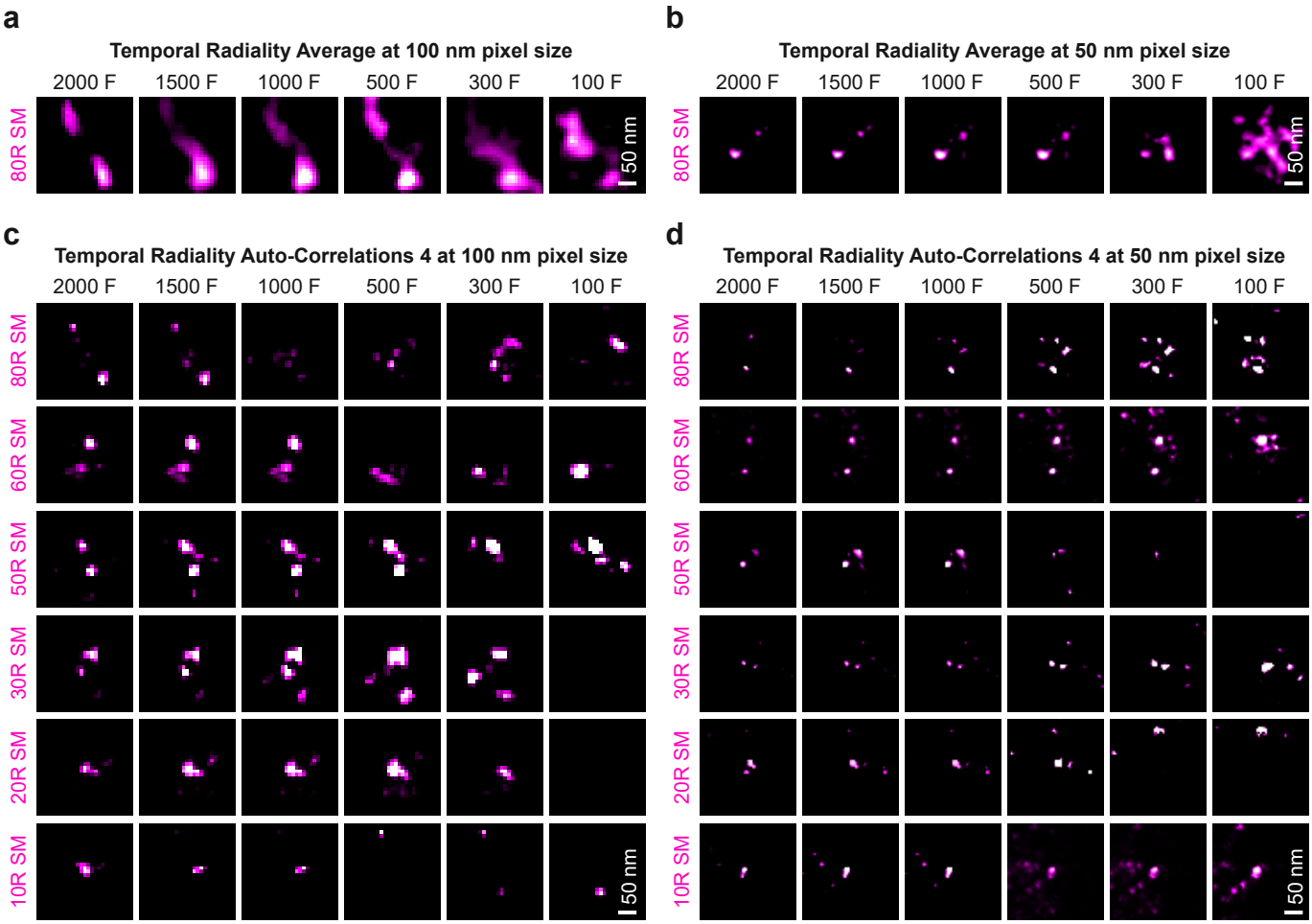

Supplementary Fig. 5. The effect of frame number on SRRF analysis. a & **b**, 80 nm rulers were imaged at 100 and 50 nm pixel sizes, and were then analyzed with the default SRRF parameter (temporal radiality average, TRA), using varying frame counts (termed F in the figure), from 100 to 2000. **c** & **d**, The same procedure was repeated using temporal radiality auto-correlations (TRAC4) for rulers of 10 to 80 nm. The frame count does not affect the TRA analysis as much as it affects TRAC4. The TRA performance, which is the parameter reported in most publications, is far poorer than that of TRAC4, when sufficient frames are analyzed. These experiments were repeated at least three times each.

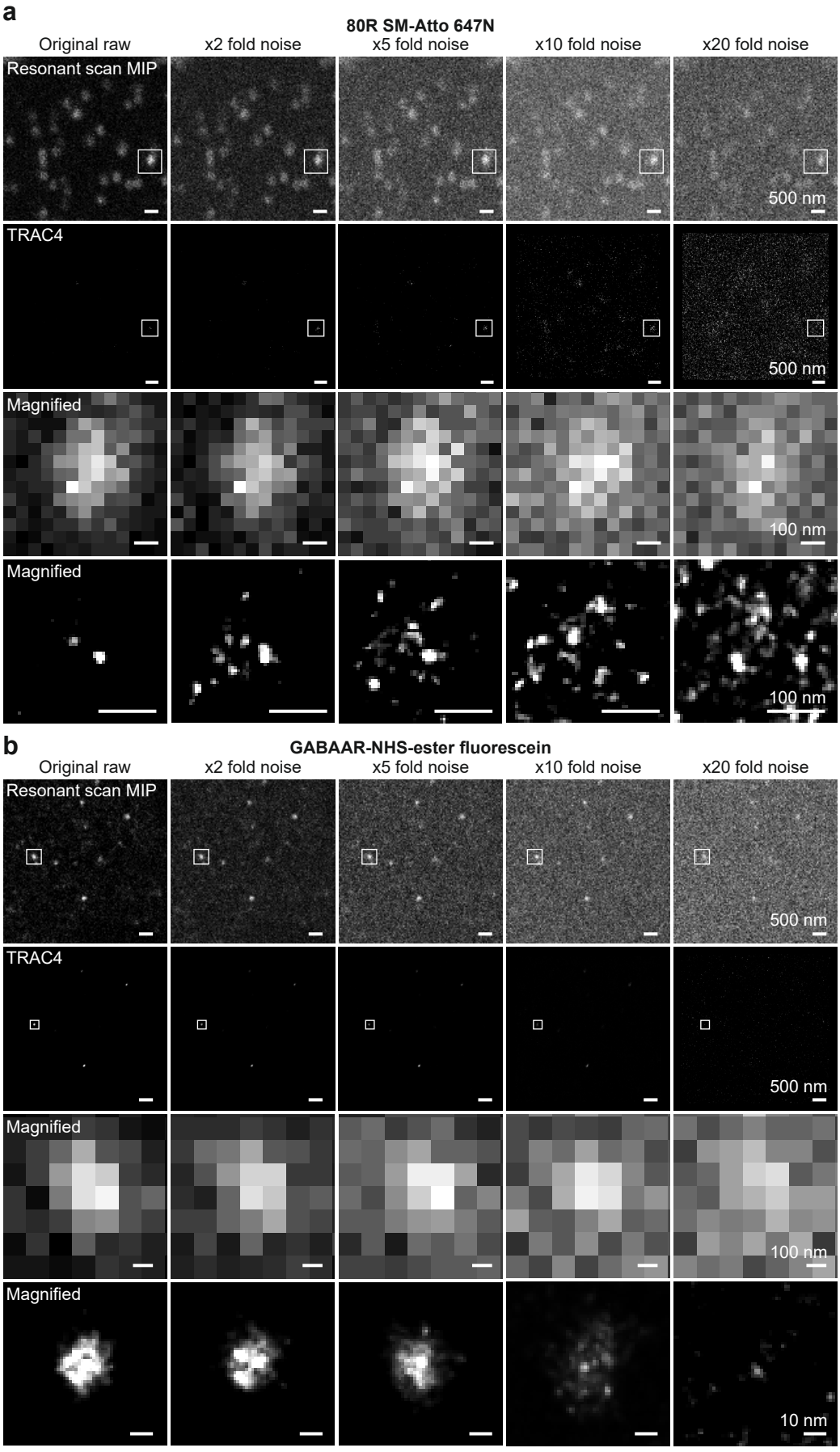

Supplementary Fig. 6. SNR effect on SRRF performance. a, The top panel shows an overview of 30 frame-MIPs of an 80 nm ruler, followed by MIPs of the same ruler that were subjected to 2-fold, 5-fold, 10-fold and 20-fold increase in noise. Noise was added artificially, using a Matlab routine. The initial SNR was 27.84...

... The second panel shows TRAC4 analyses of the data. The third and fourth panels show a magnified region from the resonant scan MIPs, and their respective TRAC4 analysis results. **b**, The same analysis was performed on expanded GABAAR. Note that the receptor pore disappears at a 5-fold noise level in TRAC4-resolved images. The nanoruler image is corrupted far more strongly by a 2-fold increase in noise than that of the GABAAR, owing to the substantially higher original SNR of the receptor image (76.72). These results are typical of 753 images acquired from 5 independent experiments.

a

ONE Chamber

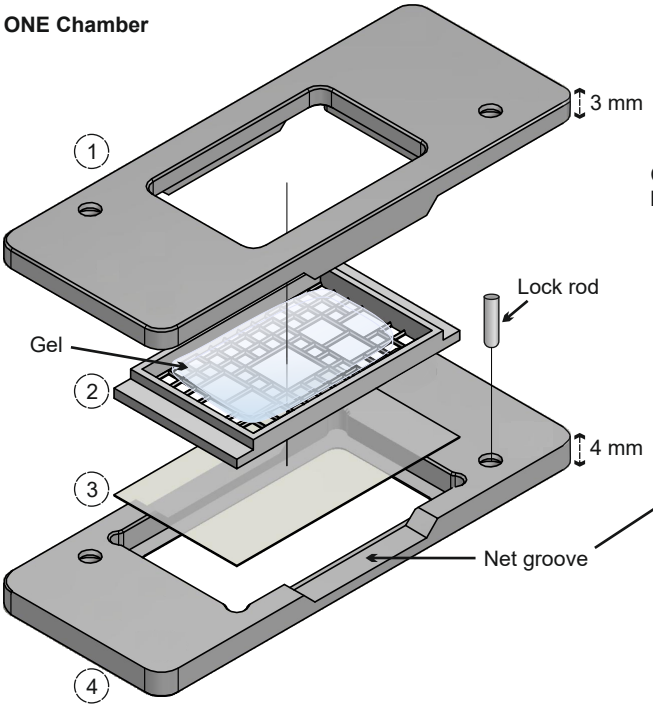

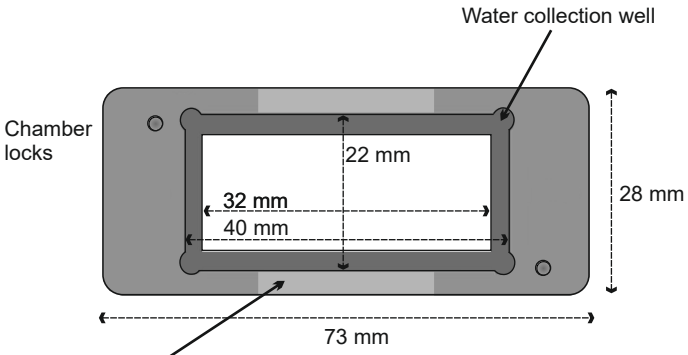

Item	Specifications
1	Chamber cover / EN AW 5083 [$AlMg_4$,5Mn 0,7]
2	3D-printed Gel cage / Pursa White Tough ink
3	Coverslip 40 x 22 x 0.18 mm / Menzel-Gl ser
4	Chamber holder / EN AW 5083 [$AlMg_4$,5Mn 0,7]

3D-printed Gel cage dimensions	(LxWxH)
Gel cage dimension:	40x22x3 mm
Central imaging zone:	7x7x0.5 mm
Six-flanking imaging zones:	5x5x0.5 mm
Counter-drift squares:	2x2x0.5 mm

b

Different views

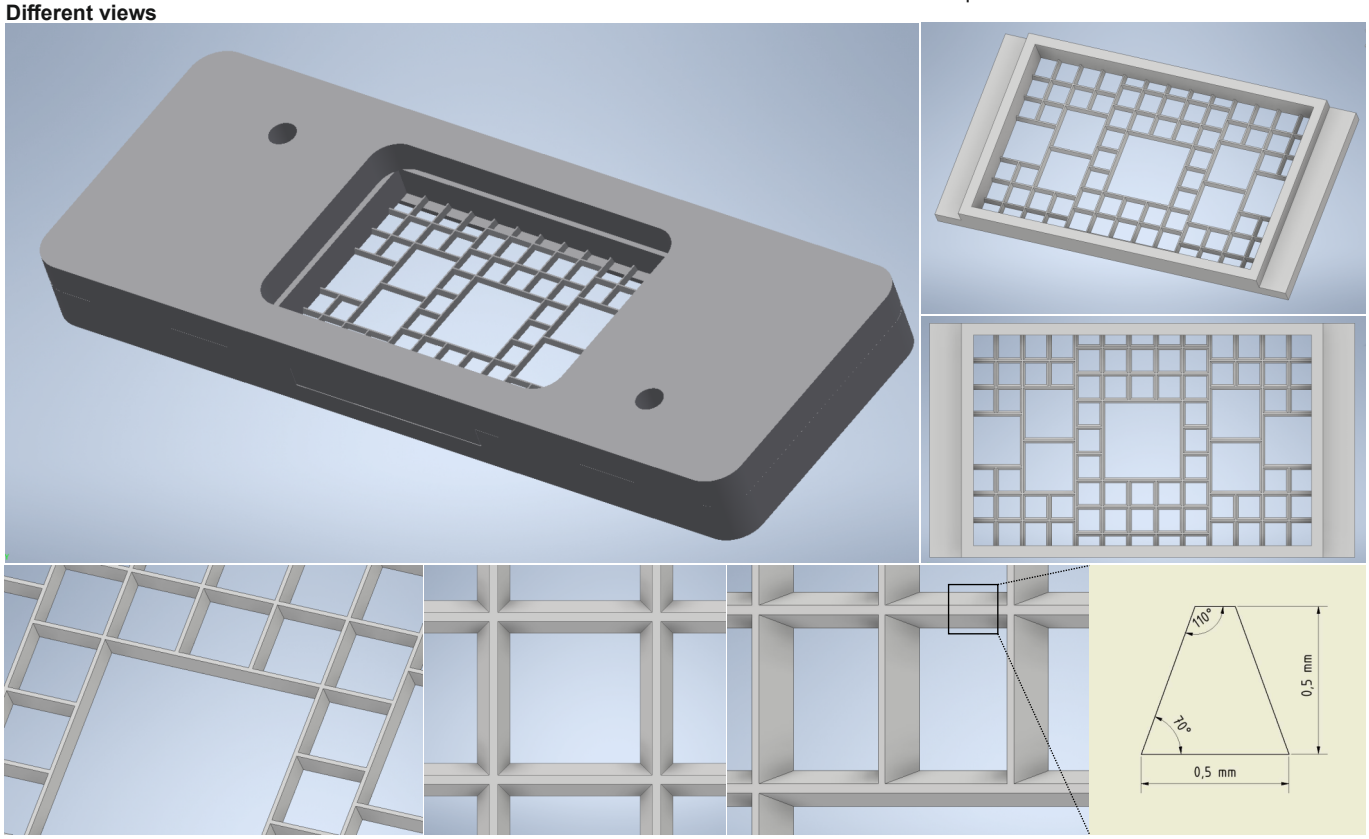

Supplementary Fig. 7. Technical scheme of the stabilization chamber used in this work. **a**, The exact measurements and materials for the stabilization chamber are included in the figure text. The 3D-printed gel cage patterning can be organized according to the user's preferred design. Only a suggested design is included here in **b**, many others work equally well. The design files can be obtained from the corresponding authors, to produce this chamber in any facility.

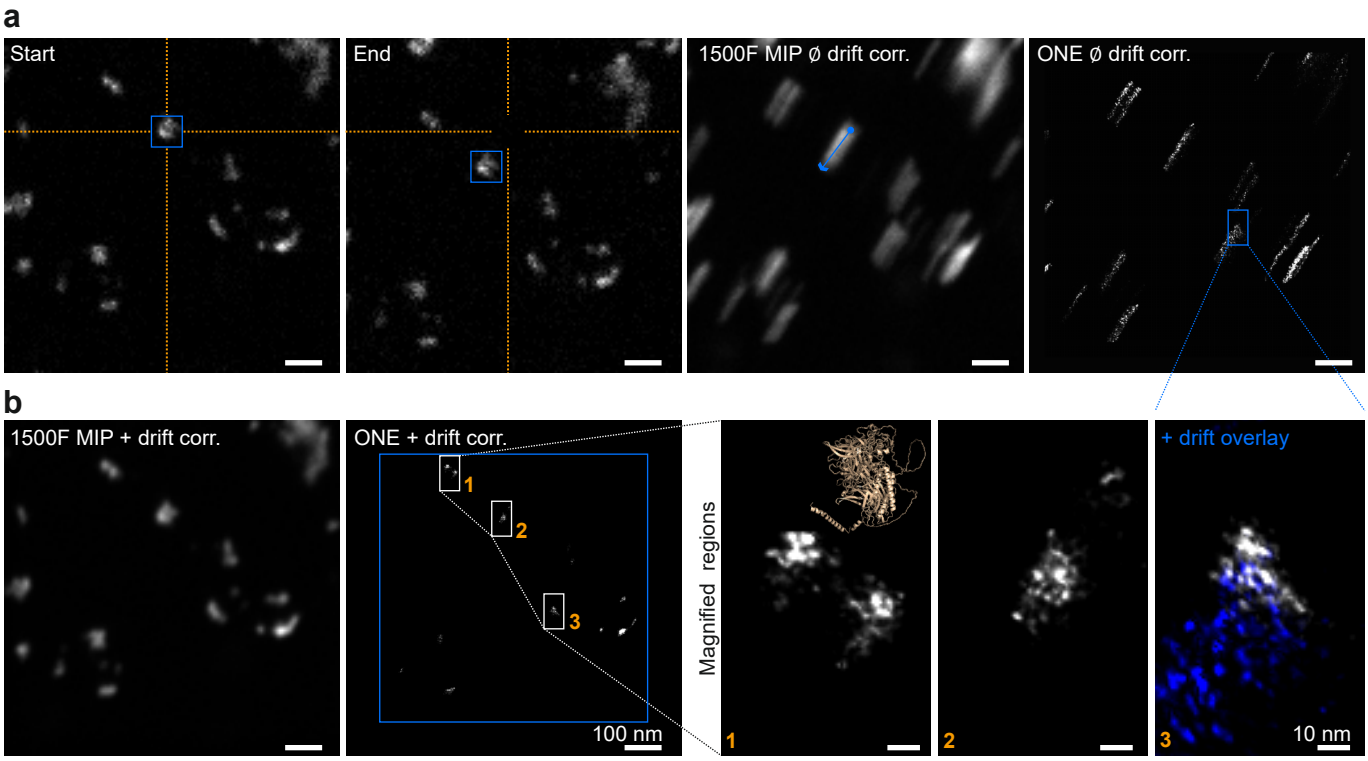

Supplementary Fig. 8. Drift compensation. a, A resonant confocal X10 image of otoferlin molecules at the start of a 1500-frame time series recording (first panel) and at its end (second panel). The third panel shows a maximum intensity projection of the resonant confocal scan. The blue arrow indicates the direction of drift. The fourth panel shows ONE processing without drift correction. A streak artefact is evident as a result. **b**, Applying drift correction, using the SRRF software, to the same acquisition and maximum intensity projection yields an image (first panel) similar to the first image in (**a**). The second panel shows the result of the ONE processing with drift correction application. The last set of panels show magnified regions of otoferlin molecules. An otoferlin AlphaFold cartoon is presented for comparison (not drawn to scale). In panel 3, the ONE image is overlaid with its counterpart from the same dataset, processed without drift correction (blue). This is a typical observation for all otoferlin and $GABA_AR$ 945 images acquired from at least of 9 independent experiments.

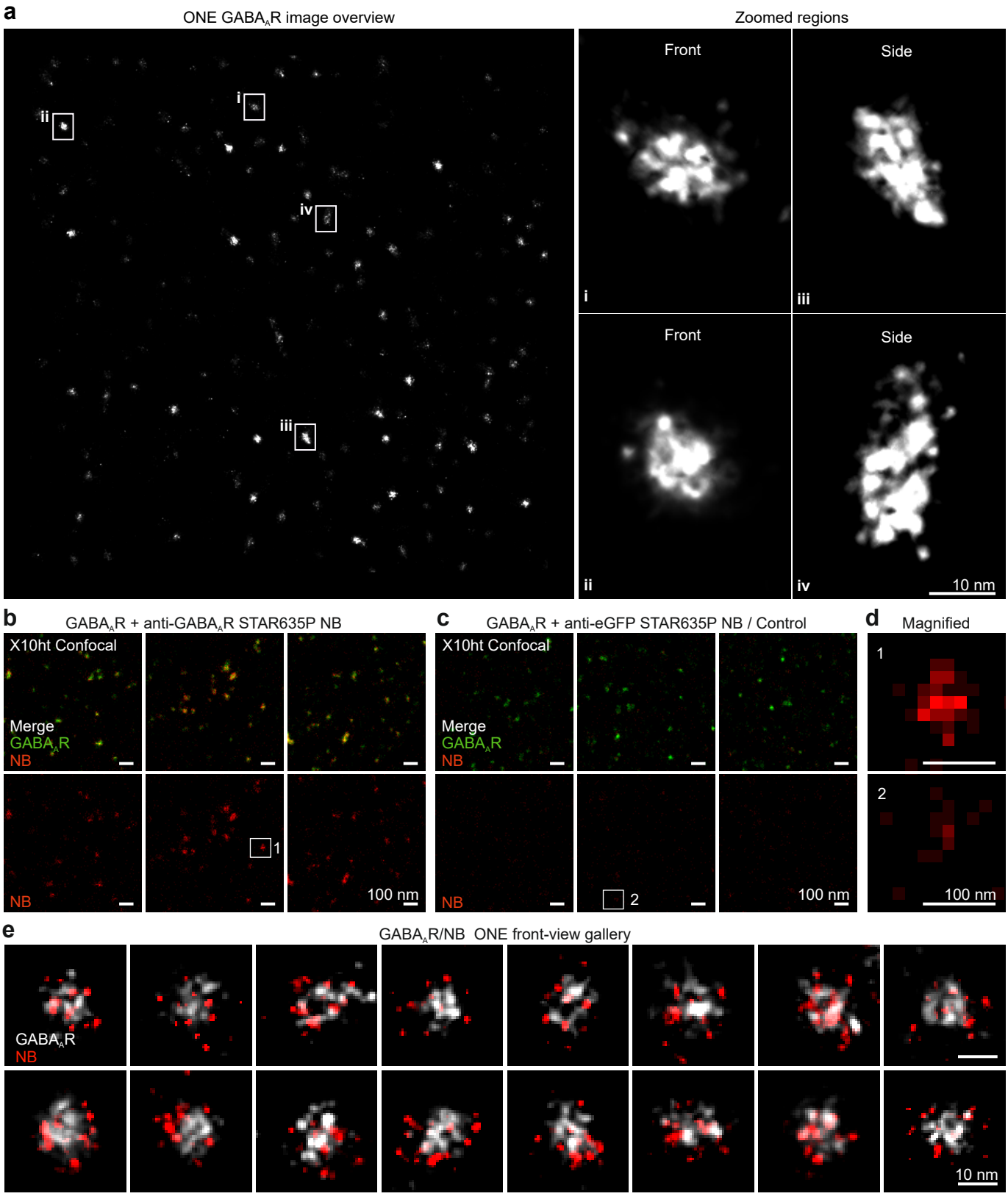

Supplementary Fig. 9. GABAAR ONE overview and nanobody labeling. a, Uncropped exemplary ONE GABA$_A$R image overview followed by four magnified regions. This is a typical overview from 105 image acquisitions from 3 independent experiments. **b**, Confocal images of expanded GABAAR labelled with anti-GABAAR nanobodies (NBs) conjugated to STAR635P. **c**, Confocal images of expanded GABAAR mixed with anti-eGFP nanobodies, which only induce little non-specific background. **d**, Magnified regions of single receptor either labelled with anti- GABAAR or anti-eGFP NBs. **e**, A gallery of ONE images showing GABAAR in white and anti-GABAAR NBs in red. A 648 GABA$_A$R+NBs images were acquired from 3 independent experiments.

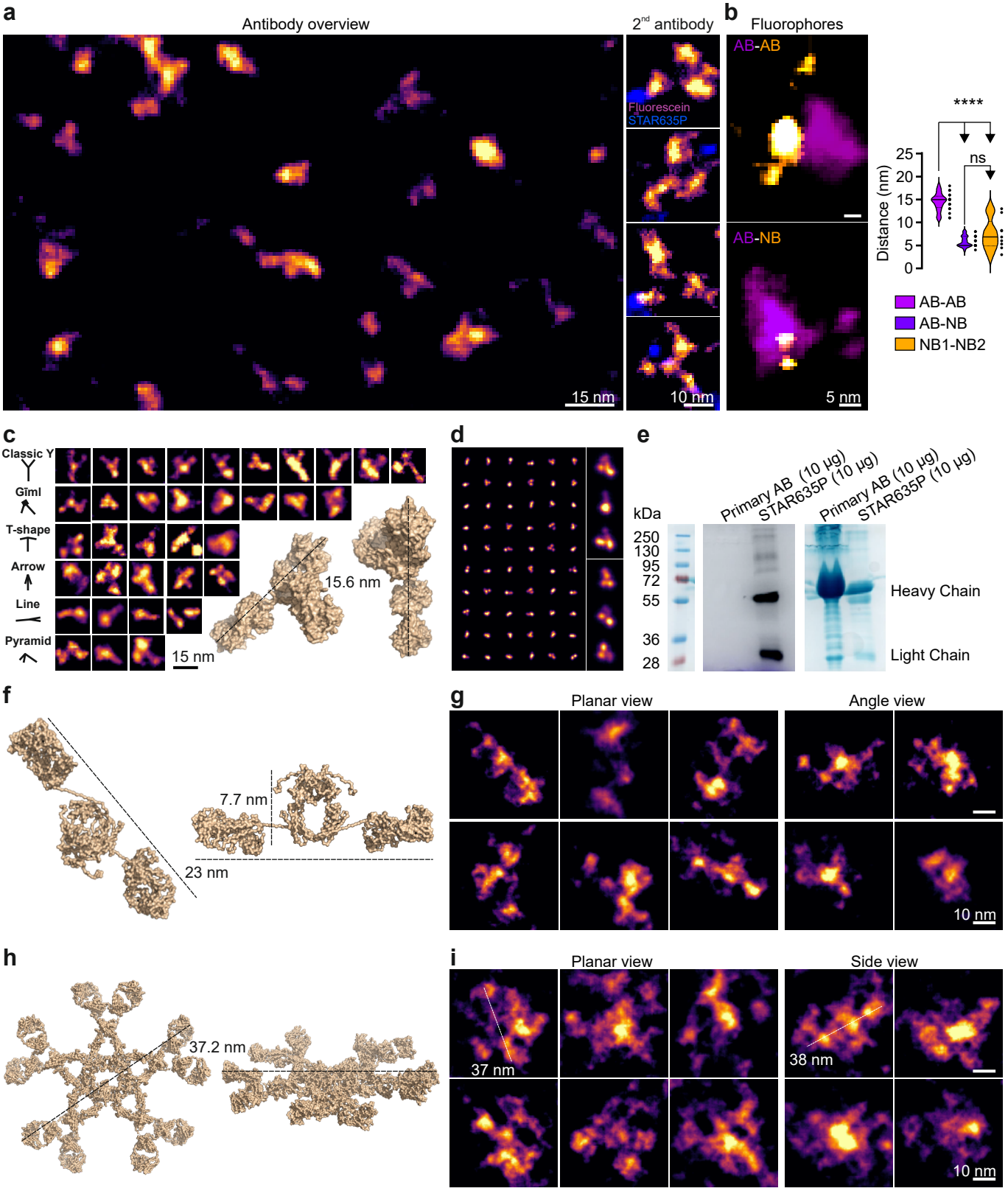

Supplementary Fig. 10. Further ONE examples of immunoglobulin imaging. a, An overview of a field showing IgG antibodies labelled using NHS-fluorescein (left), along with a few zoom-in images of fluorescently-conjugated secondary IgG antibodies (right; Abberior Star635P conjugation shown in blue). **b**, Distances between fluorescently-conjugated IgGs and fluorescently-conjugated secondary antibodies (top) or secondary nanobodies (bottom), N = 20 AB-AB and AB-NB signals from 3 independent gels for AB:AB/AB:NB molecules, two-tailed Mann-Whitney test, p = 0.0001. **c**, Several examples of IgG antibodies imaged in different positions and perspectives. **d**, A gallery of the expected antibody shapes, obtained by convoluting a PDB IgG structure with a ONE point-spread-function, after revolving the IgG molecules in 3D space randomly. A few enlarged views are shown, along with a multitude of small-sized views, to explain how IgG molecules should appear when they are visualized in fluorescence in random orientations. The typical IgG views are similar to the modeled ones. **e**, Fluorescence (Abberior Star635P) and Coomassie SDS-PAGE gels indicating...

... the size distribution of antibody fragments. A mouse monoclonal primary antibody was run on the gels, along the secondary antibody imaged in panel a. The gel was first imaged under a fluorescence (Cy5 channel) and then total proteins were revealed with Coomassie brilliant blue staining. The results from this one gel suggest that numerous small fragments are expected for both primary and secondary antibodies in the ONE images, not only full antibodies, due to impurities being present in the commercial antibody samples. **f** & **g**, An overview of IgA molecules. **h** & **i**, A similar overview of IgM molecules. The antibody structures are shown using Pymol representations from PDB structures 1HZH, 1IGA, and 2RCJ.

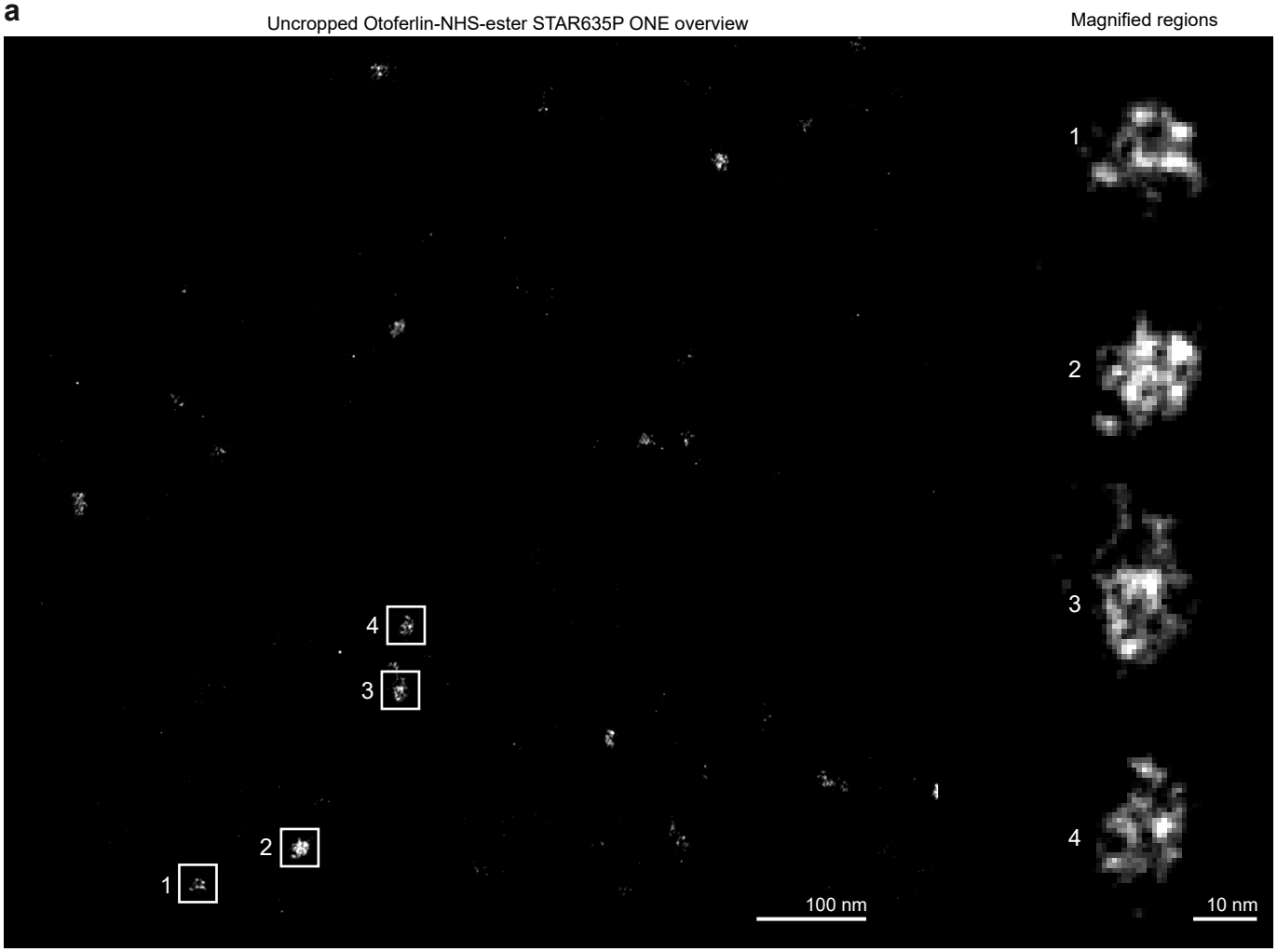

Supplementary Fig. 11. Otoferlin galleries. a, An overview of otoferlin followed by 4 magnified regions. **b**, More ONE...

... images of uncropped otoferlin overviews and their respective blank control. **c**, A gallery of magnified otoferlin molecules. These images are typical of 150 otoferlin image acquisition from at least 3 independent experiments.

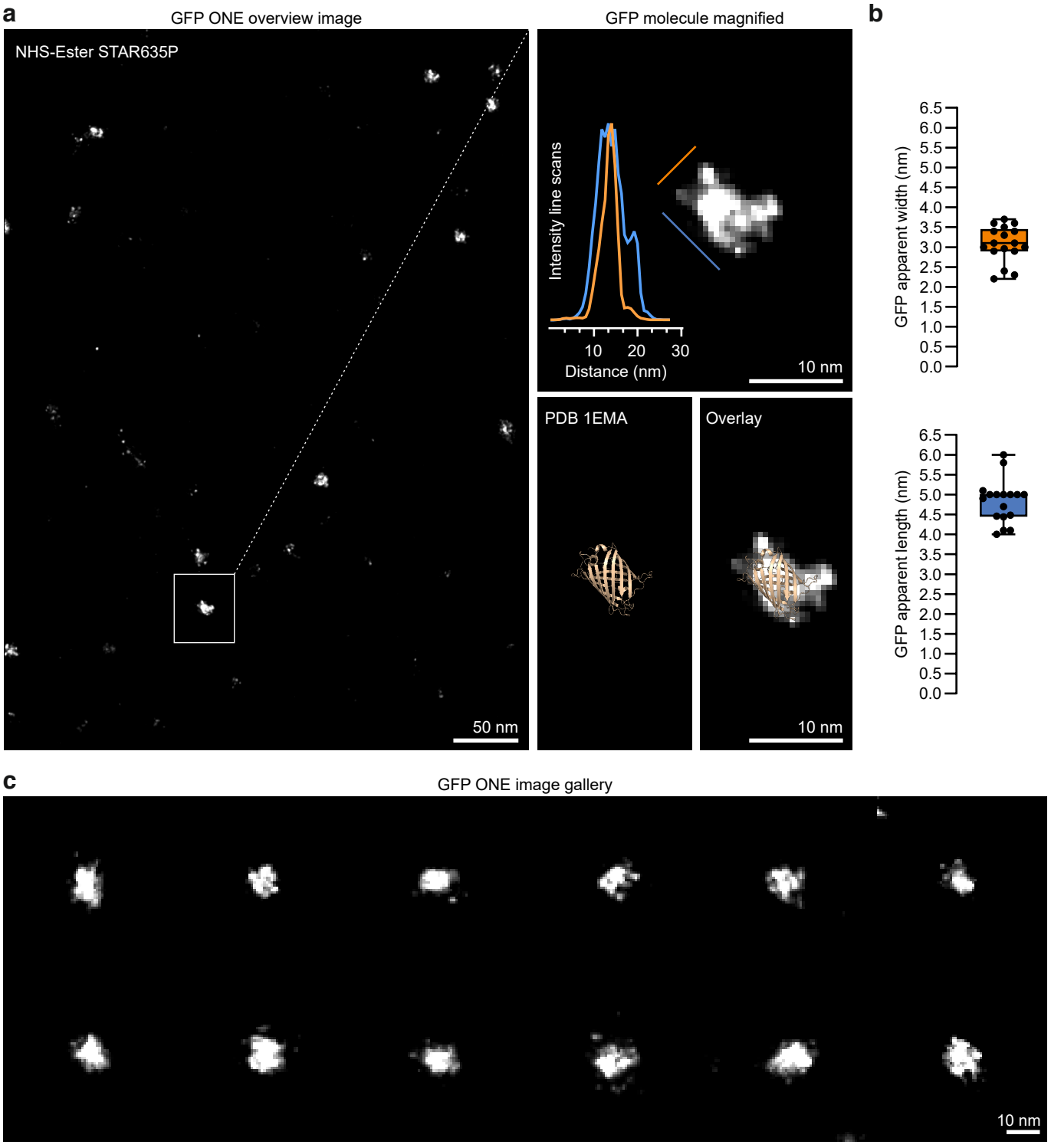

Supplementary Fig. 12. ONE imaging of purified eGFP molecules. a, The first panel shows a ONE overview of eGFP molecules labeled with NHS-Ester STAR635P. The second panel shows a magnified area. The third panel shows the eGFP 1EMA PDB structure. The fourth panel shows a PDB/fluorescence overlay. **b**, A box plot displaying the mean and the minimum and maximum whiskers for a measurement of the apparent width and length of the molecules, from line scans as the examples shown in panel a, in blue and orange. A total of 17 single molecules were measured from an n of 3 independent gels. **c**, A gallery of eGFP molecules.

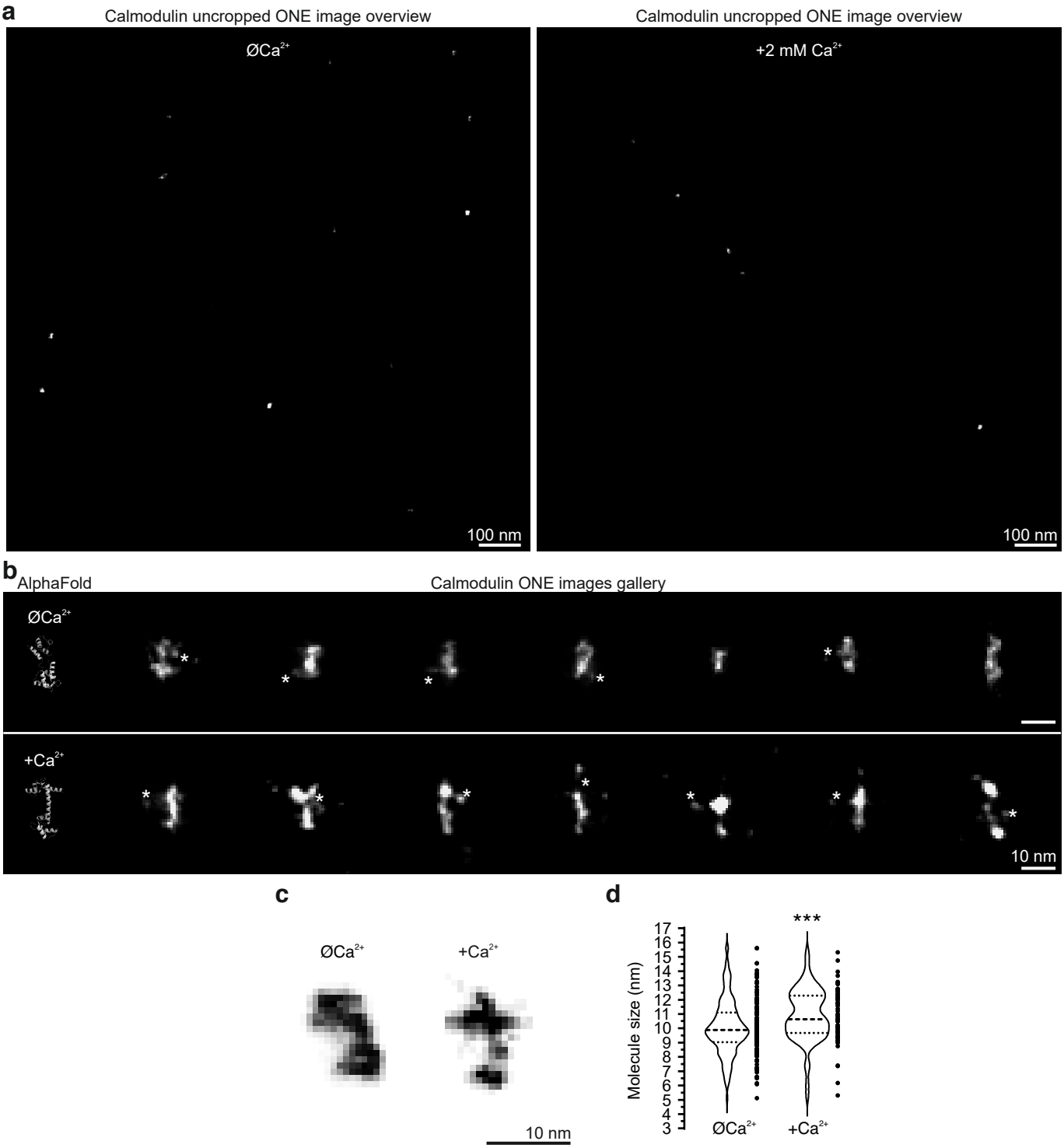

Supplementary Fig. 13. ONE imaging of purified calmodulin. a, An overview of calmodulin ONE acquisitions in the presence and absence of calcium. This molecule was expressed and purified as a chimera containing mEGFP. The compact signal associated to the GFP molecule, as observed already in the TSR images in Fig. 1, has a limited contribution to the overall size of the molecule. **b**, Exemplary zoomed calmodulin ONE images. The asterisk denotes the best guess of GFP molecule bound to calmodulin. This is a typical overview from 4 independent gels. (**C**) ONE images of calmodulin in the absence and presence of its ligand calcium after homogenization using autoclaving. **d**, Calmodulin size analysis plotted as violin plot showing the average, the quartiles and all data points. A two-tailed non-parametric Mann-Whitney test was applied (p = 0.0006, N = 155-70).

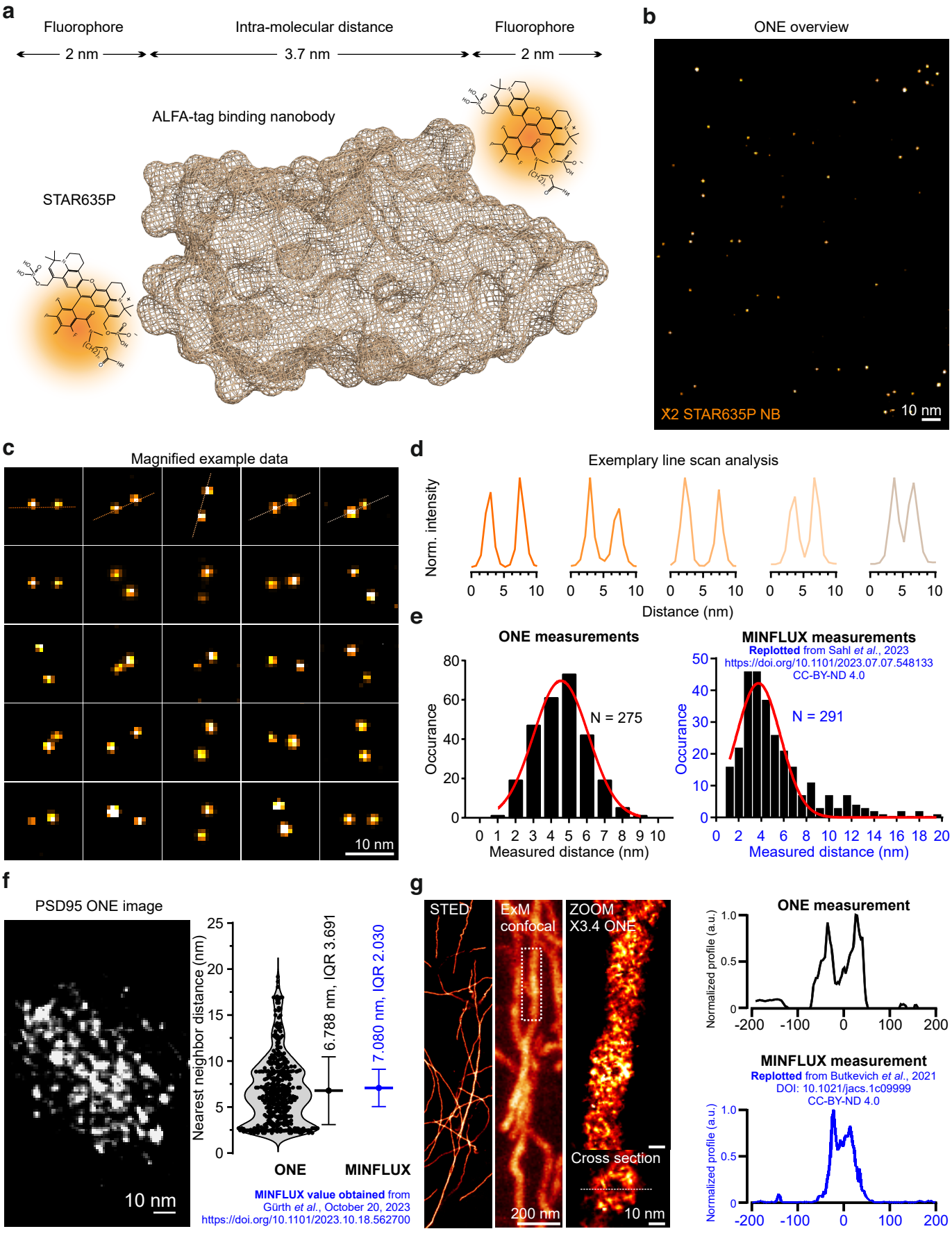

Supplementary Fig. 14. Comparative analysis between ONE microscopy and MINFLUX. **a**, ONE imaging of X2 STAR635P nanobodies. A cartoon showing an ALFA-tag nanobody conjugated to two fluorophores. **b**, An overview of purified X2 STAR635P nanobodies, *in vitro*. **c**, A magnified X2 STAR635P regions that are typically observed from at least 9 independent experiments. The line scans are displayed in (**d**). **e**, Histograms of measured distances between the two fluorophores from ONE microscopy (left, N= 275 nanobodies) and replotted MINFLUX...

... measurements (right) from Sahl *et al*., 2023. **f**, ONE imaging of PSD95 immunostained in cultured neurons, using a PSD95-specific nanobody. The exemplary image is followed by a graph that shows the nearest neighbor distances we measured for the PSD95 spots (N = 402 spot distance measurement), in comparison to measurements obtained in similar samples in MINFLUX, from Gürth *et al*., 2023. **g**, Tubulin immunostainings (relying on primary and secondary antibodies) imaged using STED, without expansion, in confocal ExM and in ONE microscopy, relying on ZOOM ExM (3.5 fold expansion) as observed from 2 independent gels. The graphs depict the line scan indicated by the dashed lines in the tubulin cross-section (top) and a replotted MINFLUX line scan measurement, obtained from Butkevich *et al*., 2021 (bottom).

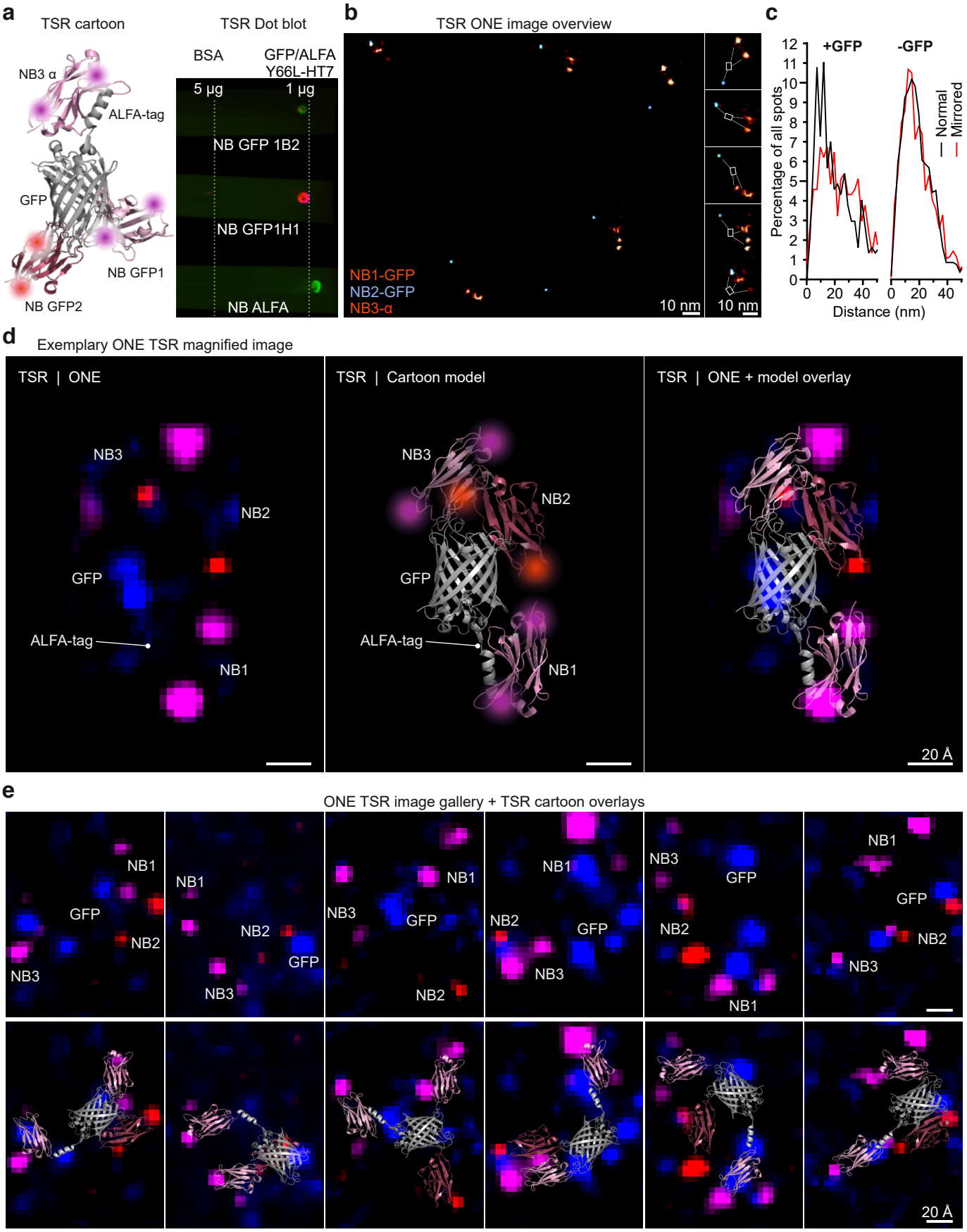

Supplementary Fig. 15. Analysis of GFP-nanobody complexes. a, TSR cartoon followed by a one dot blots experiment as a proof of principle that each nanobody was binding specifically the TSR individually, before carrying out ONE experiment. Nitrocellulose membranes were spotted with TSRs and bovine serum albumin, as control, and the spots were revealed with the respective nanobodies, using a fluorescence scanner (GE-Healthcare AI 600)...

... **b**, An overviewof an image showcasing two-color nanobodies bound to their GFP target as observed from 3 independent gels. **c**, An analysis of distances from STAR635P to Cy3 nanobodies, in normal images or after mirroring one of the fluorescence channels, as a negative control. The close-distance interval is largely removed by mirroring. N = 40-40 TSRs from at least 3 independent gels. Performing this in samples lacking the GFP, in which the nanobodies are randomly distributed, results in no differences between the normal and mirrored distributions. N= 40/40 images. **d**, The first panel shows a magnified TSR using only two-color nanobody labelling. The TSR is also labelled with NHS-ester fluorescein, and a small pixel size (0.48 nm) is used, to enable the optimal visualization. The middle panel shows a cartoon model that fits the TSR. The third panel shows an overlay of the ONE image and the model. **e**, A gallery of TSR ONE images and their respective cartoon overlays.

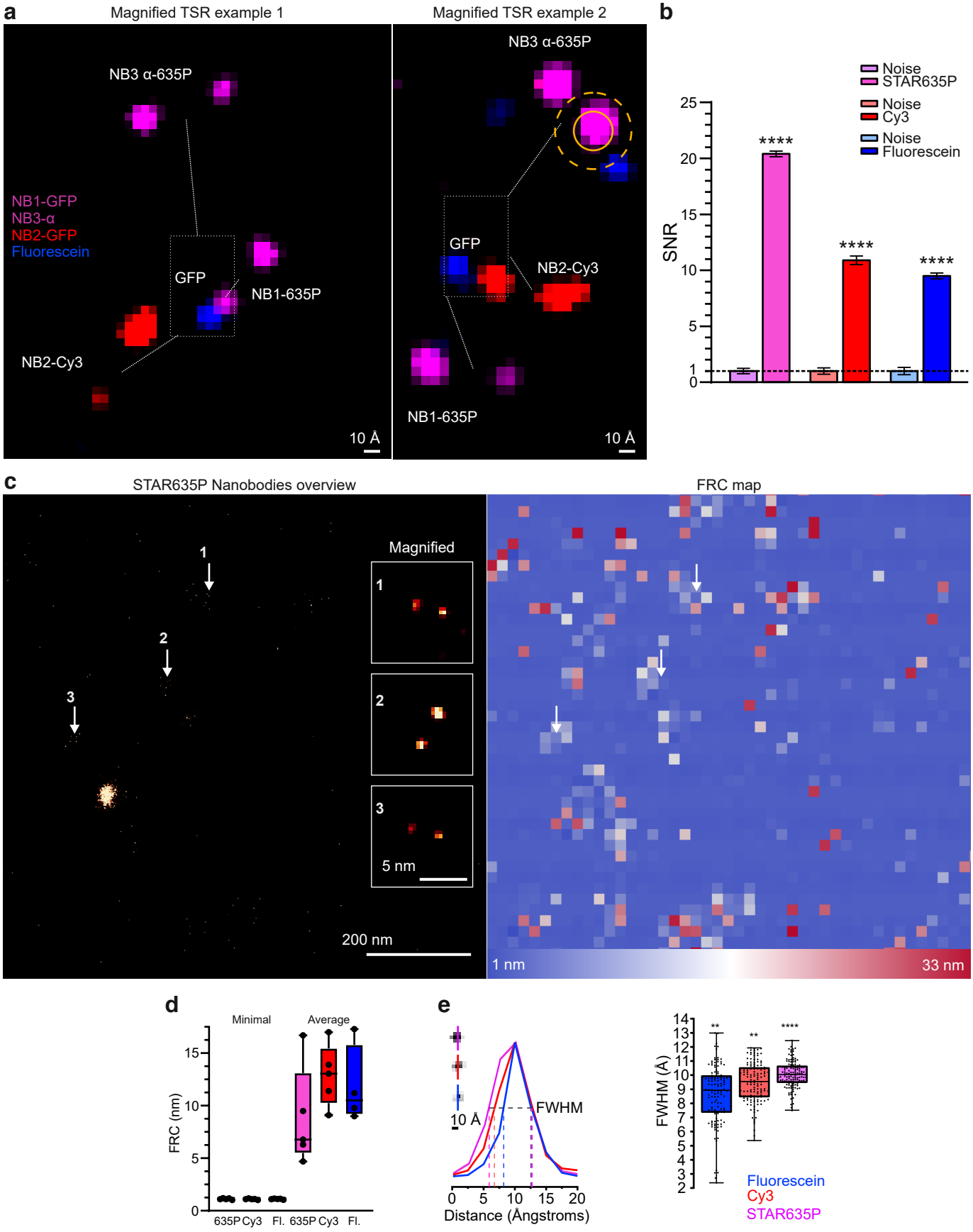

Supplementary Fig. 16. In-depth analysis of GFP-nanobody complexes. a & **b**, A bar graph of the average analysis with the standard error of mean of the signal-to-noise ratio of the TSRs, obtained by measuring the noise levels in the vicinity of the nanobodies. The noise levels are normalized to 1, implying that the normalized signal of the respective nanobodies now provides directly the signal-to-noise ratio. N = 20-18, 12-14, and 17-11 measurements from the fluorophore and noise signals from nanobodies with STAR635P, Cy3 and fluorescein, p < 0.0001, 0.0006 and < 0.0001, respectively. A two-tailed Mann-Whitney test was applied. **c**, An exemplary display of Fourier Ring Correlation (FRC) analysis of nanobody images.

d, The best and average FRC analyses obtained per image, in the different color channels (N = 4 to 5 analyses for each acquired from different gels). **e**, To approximate the apparent resolution of the system, we drew line scans across spots and measured the full width at half maximum (FWHM) in curve fits executed on the line scans. The graph plots the FWHM of 129, 135, and 132 fluorescein, Cy3 and STAR635P line scans. The values are significantly different between the color channels. $p = 0.0024$, $p < 0.0001$ and p 0.0096 for fluorescein vs. Cy3, fluorescein vs STAR635P and Cy3 vs. STAR635P, respectively. A Kruskal-Wallis test with Dunn's multiple comparisons test were applied. The box plot shows the median, 25th percentile and the range of values.

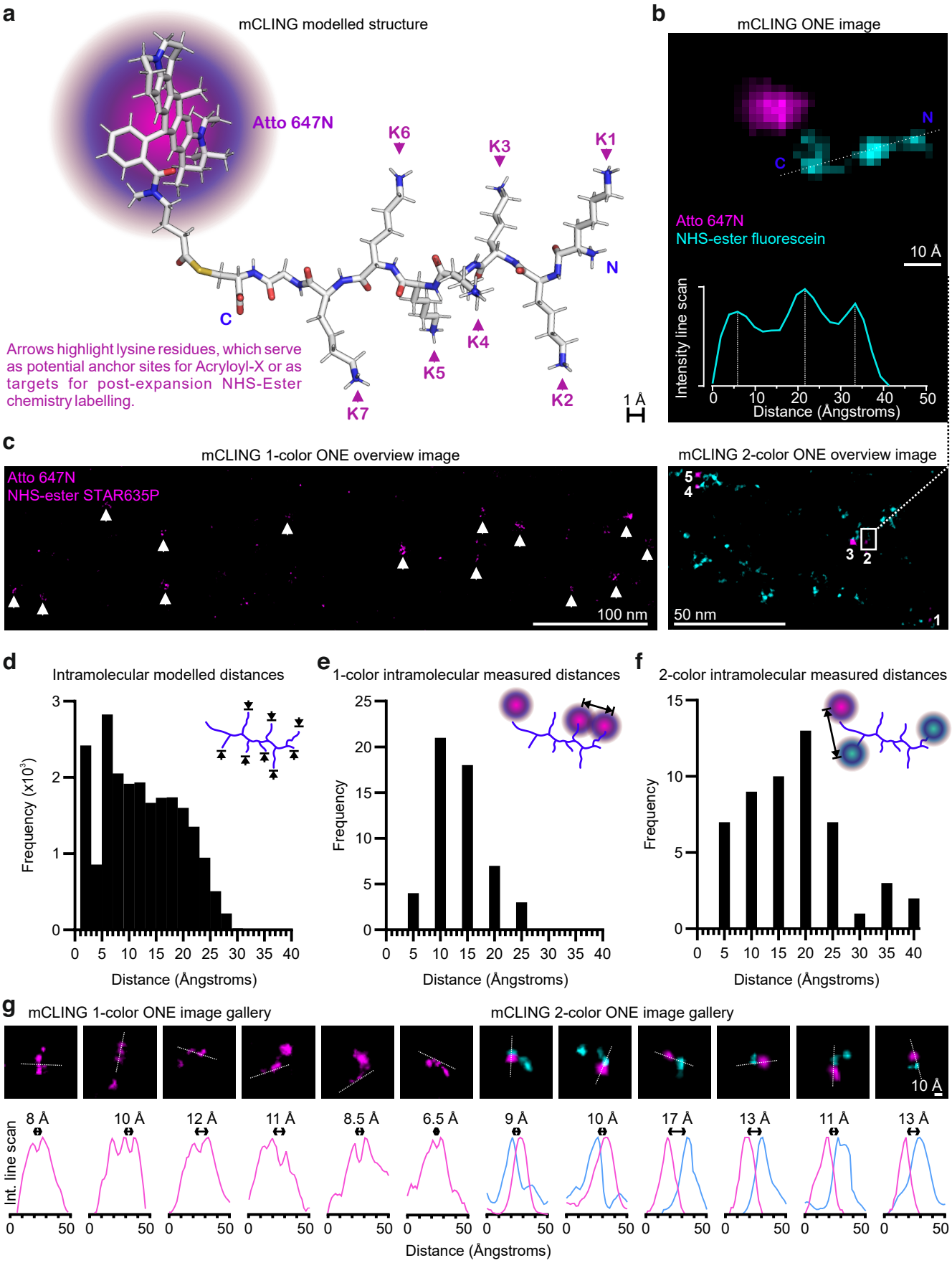

Supplementary Fig. 17. ONE Microscopy multi-color fluorophore imaging of a small peptide. a, A modelled mCLING structure, using the AMBER99 force field-GROMACS simulation package (please see Methods sections for more details). In mCLING, seven lysine residues are positioned at a varying distance from the C-terminal end, with separation intervals...

... spanning from a modelled proximal 3.627 Å to a more distal 27.954 Å. In our experiments, mCLING carries an Atto647N fluorophore. **b**, A 2-color image of mCLING-Atto 647N, labeled with NHS-ester fluorescein after expansion. The indicated intensity line scan is displayed below the image. **c**, A 1-color ONE overview image of mCLING-Atto 647N, labeled with NHS-ester STAR635P after expansion (left side), and a 2-color ONE overview of mCLING-Atto 647N, labeled with NHS-ester fluorescein. **d**, A frequency graph showing intramolecular distances between the C terminus and the lysin residues. **e**, A binned frequency graph of intramolecular measured distances from 1-color and (**f**) 2-color mCLING ONE images. Three independent experiments were carried out, and N1-color = 53 and N2-color = 52 measurements were performed. All mCLING experiments were independently repeated 3 times with 2 gels each. **g**, Exemplary 1- and 2-color mCLING ONE images, with line scans drawn over the exemplary pairs of spots. The intensity line scans are displayed below each panel.

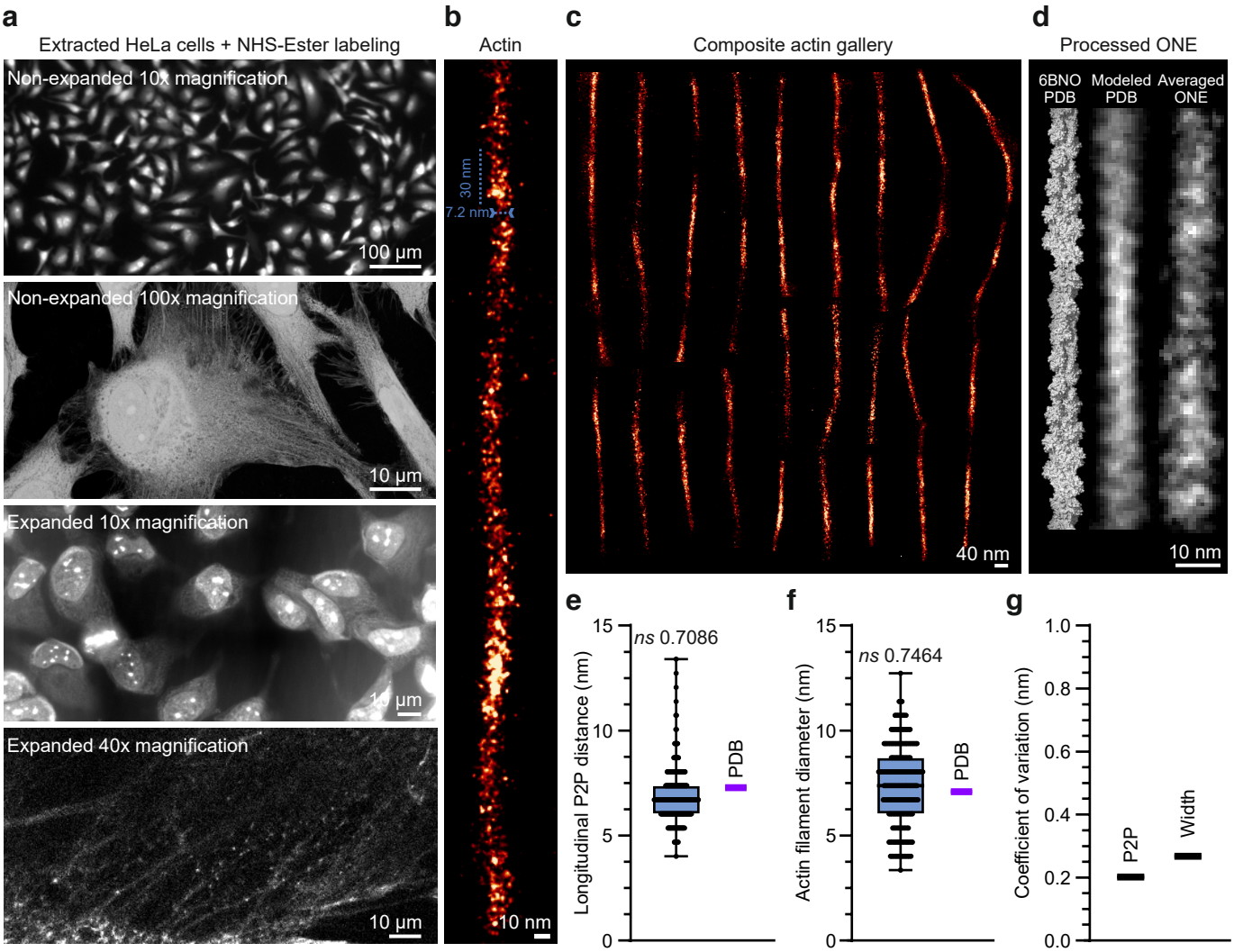

Supplementary Fig. 18. ONE imaging of cytoskeletal components, in NHS-ester labelled cells. a, HeLa cells were subjected to extraction according to a previously published protocol (Svitkina *et al.*, 2016). Panels from top to bottom show an overview of non-expanded, extracted HeLa cells labelled with NHS-ester chemistry (10x objective), followed by a higher magnification view and by two views of cells expanded after extraction. **b**, An exemplary image of a cytoskeletal filament. **c**, Composite actin gallery. **d**, A PDB cartoon, followed by a modeled averaged PDB, depicting a best-case scenario for ONE microscopy of actin fibrils under ideal conditions, and the achieved ONE image reconstructed from 47 different actin regions from 2 independent experiments from 4 gels. **e**, **f**, & **g**, A set of measurements that were applied over actin filaments, quantifying the longitudinal peak-to-peak distance along the filament (distance between actin monomers), the actin filament width, and the coefficient of variance of these two measurements, respectively. These values resemble well the known dimensions from actin PDBs (magenta lines). N = 198 and 130 actin measurement for the first graph and second graph, respectively; 2 independent experiments. Data in **e** and **f** are plotted as box plots with all data points and whiskers showing minimum and maximum values. An unpaired nonparametric two-tailed t-test was applied.

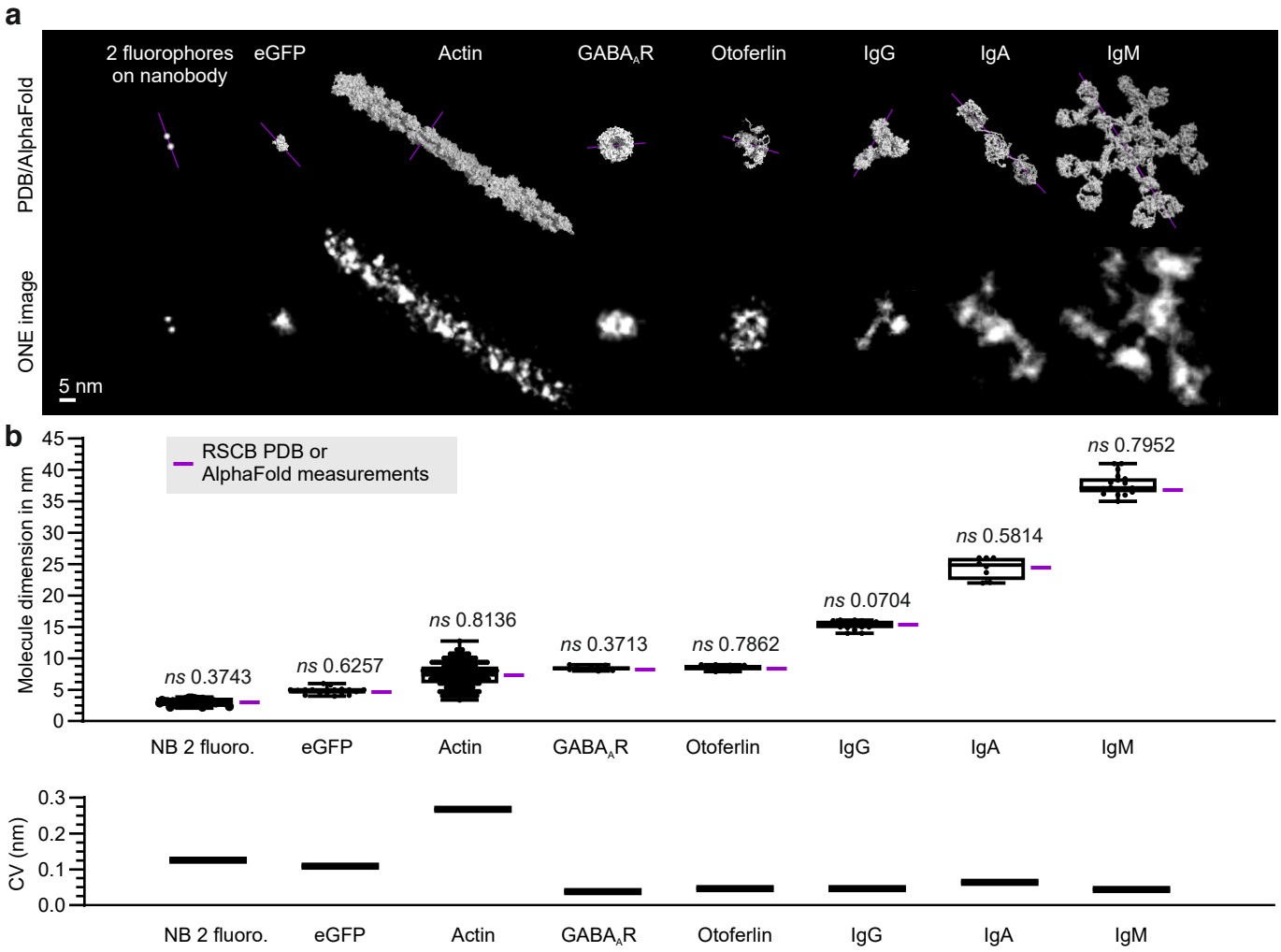

Supplementary Fig. 19. Expansion precision evaluation. **a**, A direct compassion between single-molecule ONE images and their respective PDB/AlphaFold models. The purple line indicates the line scan used to measure the molecule dimension indicated in the first graph. **b**, The upper graph shows measurements of molecule dimensions, in nm displayed as box plots with averages and whiskers showing minimum and maximum values. The horizontal purple line indicates the expected value, obtained from measurements of PDB structures (for all molecules except otoferlin), or AlphaFold predictions (for otoferlin). The lower graph shows the variability of these measurements, in the form of the coefficient of variance. N = 34, 17, 192, 10, 10, 14, 8, and 18 size measurement for NB, eGFP, actin, GABAAR, otoferlin, IgG, IgA, and IgM; at least 2 experimental replicates were carried for all experiments. Paired t tests were carried out to determine whether the measured values are different from the values predicted by the PDBs; the respective *p* values are reported above the plots. A two-tailed Mann-Whitney tests were applied.

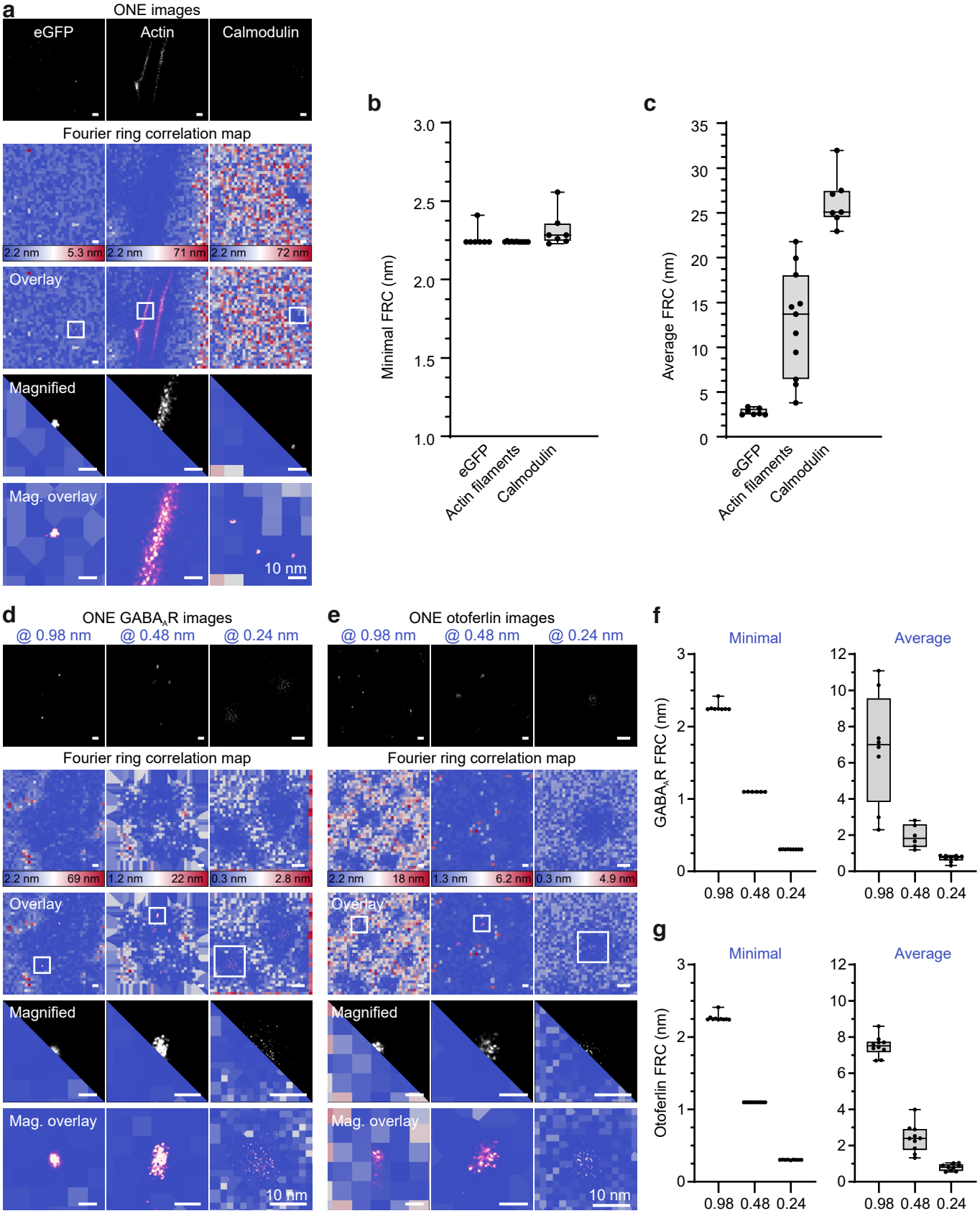

Supplementary Fig. 20. Detailed analysis of Fourier ring correlation. a, FRC analysis of ONE images collected with a pixel size of 0.98 nm. The first panel row shows ONE images of the different specimens. The second row shows the corresponding FRC maps. The third row shows ONE images overlaid over FRC maps, using a screen-blend mode. The fourth and fifth rows show magnified views. These data are as typically observed from 3, 2, and 4 independent gels for eGFP, actin and calmodulin, respectively. **b**, A graph plotting the minimal FRCs in nm. **c**, A graph plotting the average FRCs in nm. Please note that all the labelled targets reside in the "bluest" regions of the map, indicating minimal FRCs that correspond to high resolution. N = 7, 12, and 7 FRC measurement for eGFP, actin, and calmodulin, respectively. **d** & **e**, FRC analysis of ONE...

... images achieved with a pixel size at 0.98, 0.48, and 0,24 nm for GABAAR and otoferlin, respectively, as observed from at least 4 independent experiments for each. **f**, The graphs shows minimal and average FRCs in nm for GABAAR ONE images. N = 8, 6, and 9 for 0.98, 0.48, and 0.24 nm images, respectively. **g**, The graphs shows minimal and average FRCs in nm for otoferlin ONE images N = 10, 10, and 9 FRC measurement for 0.98, 0.48, and 0.24 nm images, respectively. All experimental sets were performed with at least 2 replicates. Data in **b**, **c**, **f** and **g** are plotted as box plots with the average and whiskers showing minimum and maximum values.

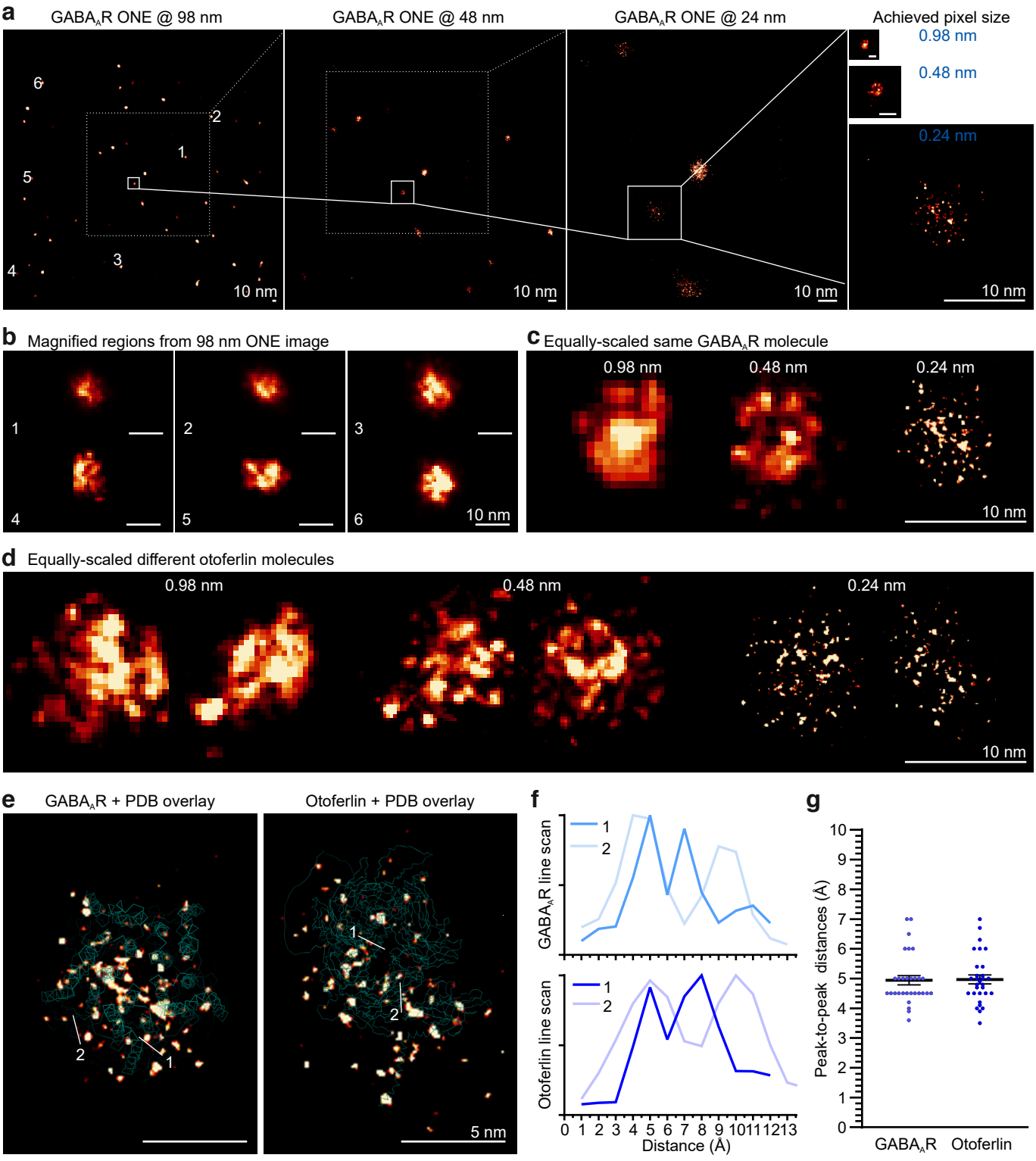

Supplementary Fig. 21. Intra-molecular measurements within a single protein molecule. **a**, GABA$_A$R ONE images acquired with 0.98, 0.48, and 0.24 nm pixel sizes, for the same region. **b**, GABA$_A$R magnified examples from the first image in the panel above. **c**, One particular GABA$_A$R molecule displayed at different resolutions. (**D**) Equally-scaled otoferlin molecules acquired at different resolutions. **e**, ONE images of GABA$_A$R and otoferlin at 0.24 nm overlaid with their respective PDBs. **f**, The graphs show 2 exemplary line scans for peptide segments in GABA$_A$R and otoferlin. **g**, A dot plot graph with the average and standard error of mean showing peak-to-peak distances in Ångström. N = 30 line scans for GABA$_A$R, and 30 line scans for otoferlin, 10 independent experiments for GABA$_A$Rs and 4 independent experiments for otoferlin, of which representative images are shown in panels **a-e**.

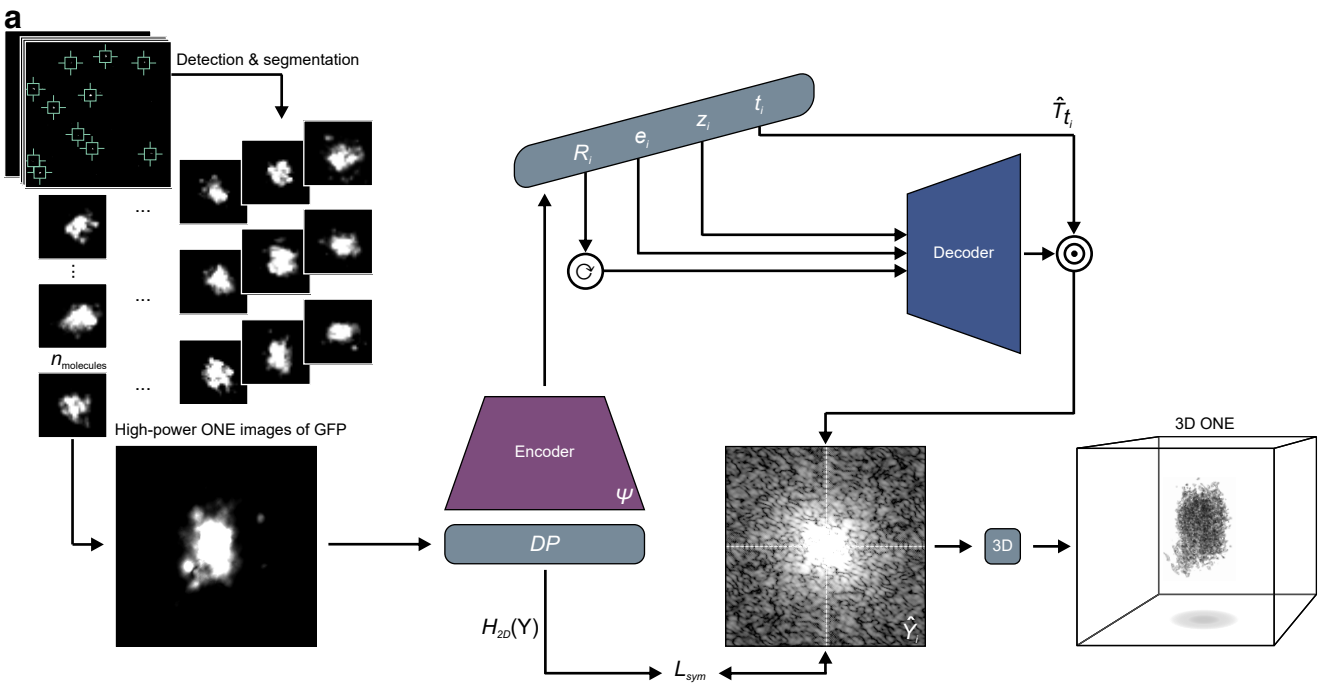

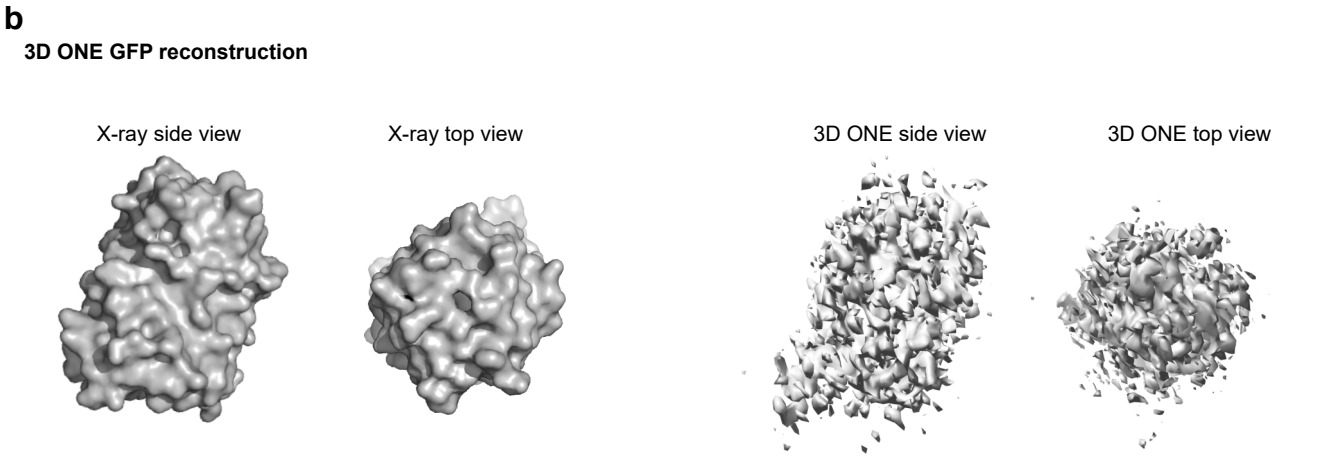

Supplementary Fig. 22. 3D ONE reconstruction via unsupervised *ab initio* artificial intelligence architecture. a, Molecules of interest are automatically detected and segmented from 2D ONE images. Fluorescence images are converted to density points *DP*. *DP* images are transferred into a modified cryoFIRE network (Levy *et al*., 2022, arXiv:2210.07387v1) that performs heterogeneous reconstructions in an amortized interreference framework of images with unknown positions in the 3D space. The encoder predicts, for each molecular image, a set of features that includes a linear scale of intensity D_i, the latent variables rotation R_i, expansion factor correction e_i, molecule conformation Z_i, and the translation t_i. The decoder deciphers the encrypted features in the Hartley domain, followed by performing elementwise multiplication with t_i to form the predicted image $\hat{Y_i}$. The network backpropagates using the symmetric loss function L_{sym} with the $H_{2D}(Y)$, and the decoded information is stacked in perpendicular slices, allowing the generation of 3D reconstructed files that can be viewed using UCSF ChimeraX. **b**, 3D reconstruction of GFP from 885 molecules. For comparison, GFP side and top views are shown from X-ray 4KW4 PDB and from our reconstruction. Fourier shell correlation analysis indicated that the 3D ONE structure is generated at a resolution of 18 Å.

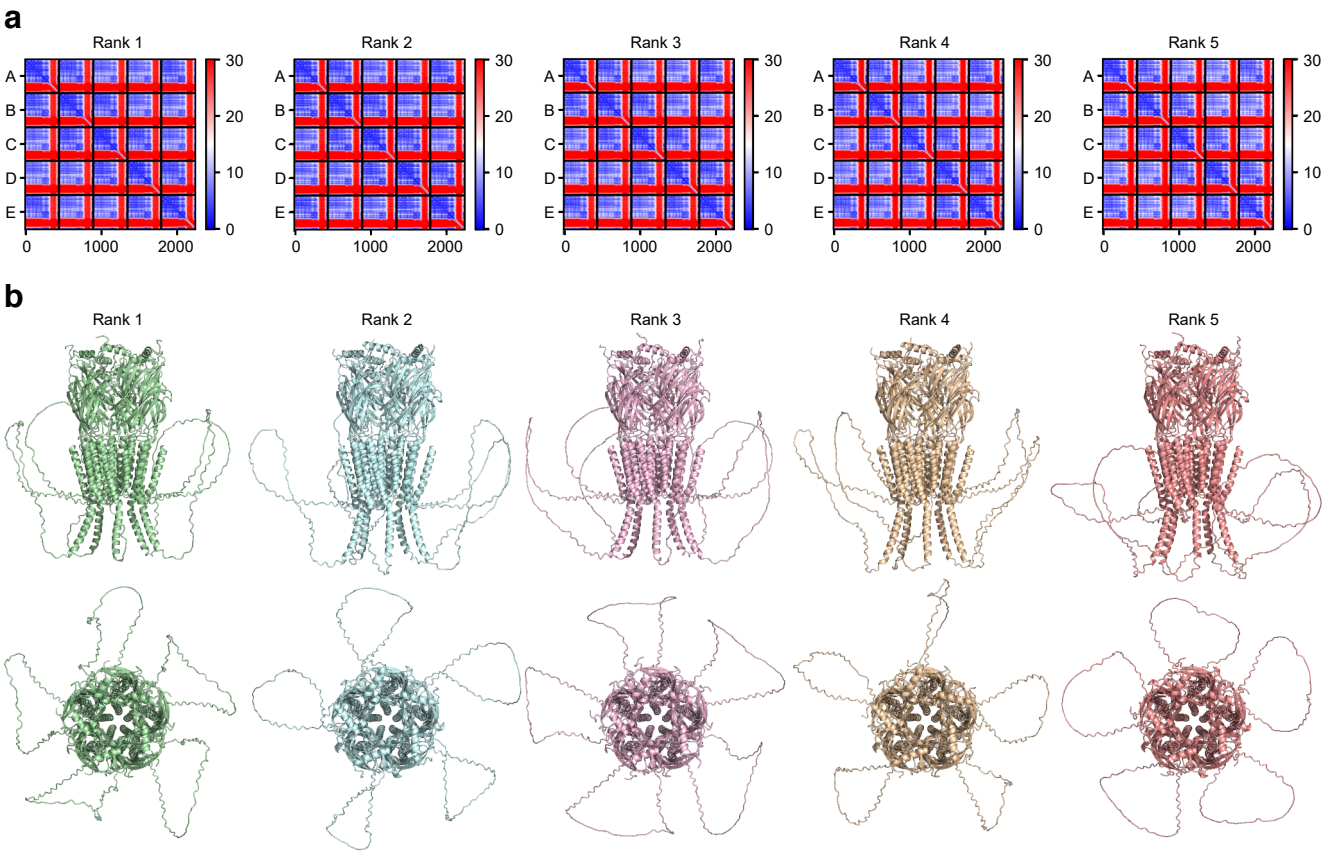

Supplementary Fig. 23. AlphaFold multimer prediction of a homopentameric GABAA beta 3 receptor. a, Matrices of predicted aligned errors (PAE) for the top 5 ranked models. **b**, Top five GABAA beta3 receptor predictions. For more information, see Supplementary Material.

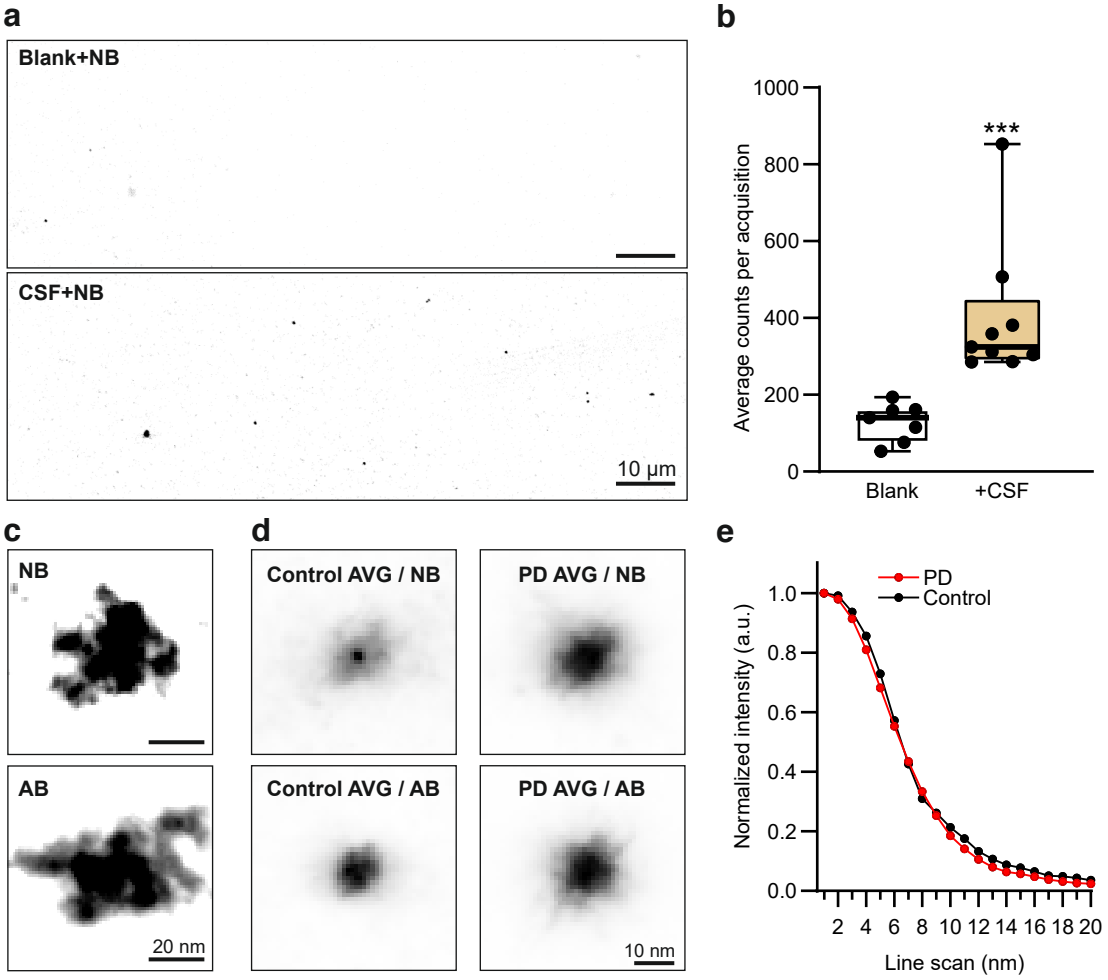

Supplementary Fig. 24. The nanobody imaging of ASYN objects is specific and is not easily reproduced by antibodies. **a**, Low-resolution images of CSF-containing samples, or blanks (clean, BS-coated coverslips). Only a few dim spots, presumably representing single nanobodies, are seen in the blanks. **b**, Quantification of the signal intensity, as a sum across all image pixels plotted as a box plot with average and whiskers showing the minimum and maximum values. N = 7 and 9 independent region measurements for blank and CSF; two-tailed non-parametric Mann-Whitney test, *P* = 0.0002. **c**, Individual examples of oligomers immunolabelled with nanobodies (top) or antibodies (bottom) as observed in 986 and 66 acquired images with nanobody or antibody labeling from multiple gels. **d**, Averages of SYN objects from individual patients, immunolabeled with nanobodies or antibodies. **e**, An analysis of the average object size in antibody-labelled samples, as in Fig. 4. N = 2 patients for each condition. Nanobodies reveal differences between patients, at object sizes of only a few nm. Antibodies have difficulties in this direction, as their large size causes a lower-fidelity labelling, and as their sizes obscure the actual sizes of small objects.

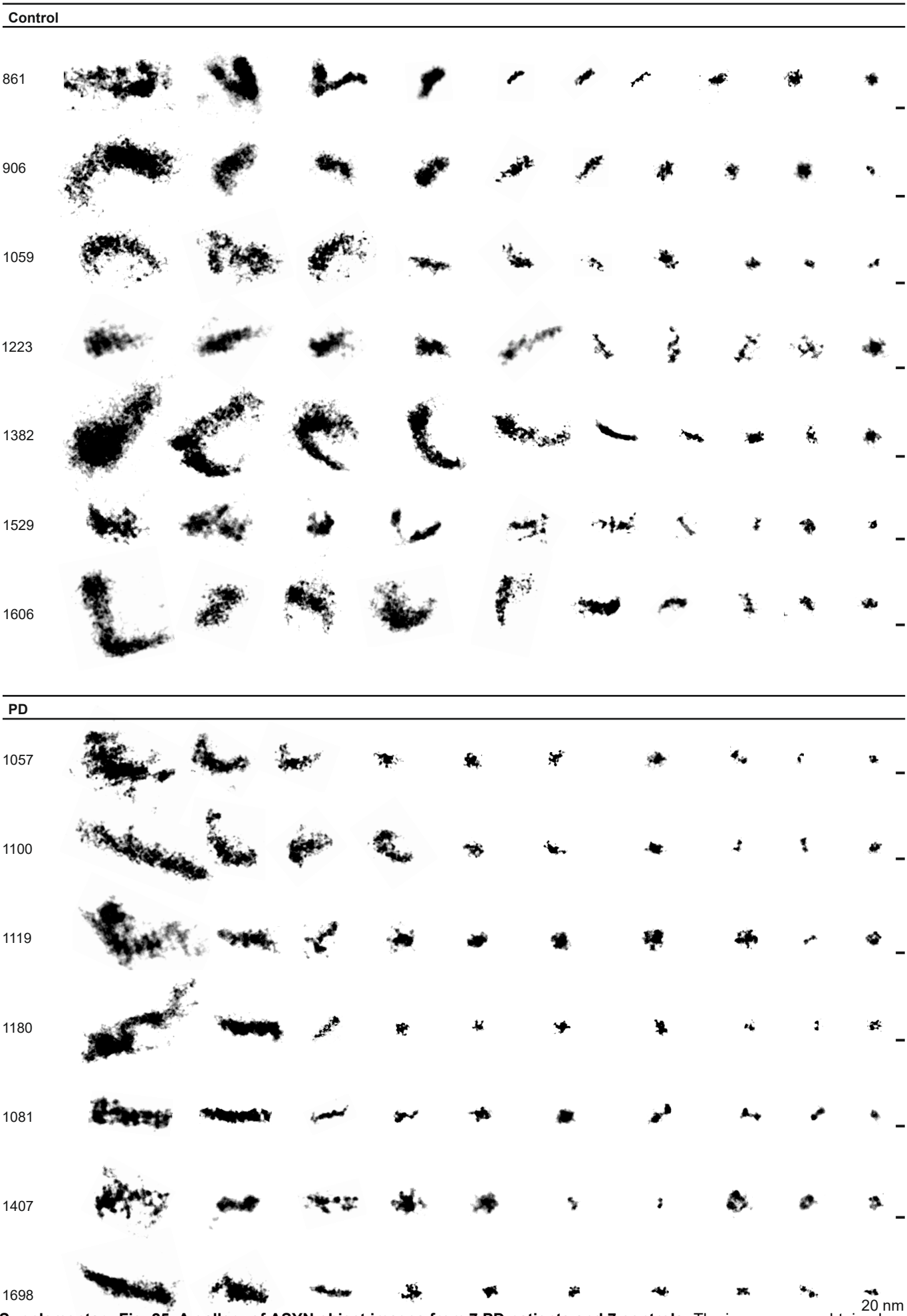

Supplementary Fig. 25. A gallery of ASYN object images from 7 PD patients and 7 controls. The images were obtained following the procedure indicated in Fig. 4a. See Supp. Table 1 for details on the respective patients.

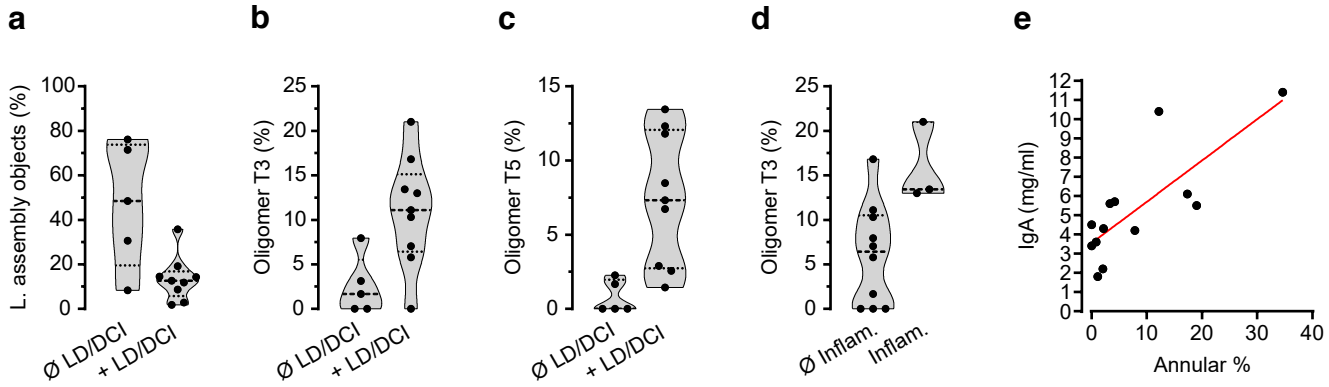

Supplementary Fig. 26. Analysis of ASYN species in relevance to medication status and clinical features. The violin plots (**a**, **b**, & **c**) show large assembly objects, Oligomer T3, and Oligomer T5 in relation to the presence of absence of Levo-DOPA treatment. **d**, Oligomer T3 percentage in the presence or absence of inflammation. **e**, The relation between IgA and Annular ASYN species. Large assemblies correlate inversely with Levo-DOPA and decarboxylase inhibitor (LD/DCI) treatments; oligomer types 3 and 5 correlate positively with these treatments (two-tailed t-tests followed by a Benjamini-Hochberg multiple testing correction with FDR of 5%; $p = 0.0066$ for panel **a**; $p = 0.0166$ for panel **b**; $p = 0.0075$ for panel **c**). Type 3 also correlates significantly with brain inflammation ($p = 0.021$). Annular oligomers correlate well with IgA levels in CSF ($p = 0.0015$, Pearson correlation test; the Pearson's correlation test was calculated using the corr2 function in MATLAB).

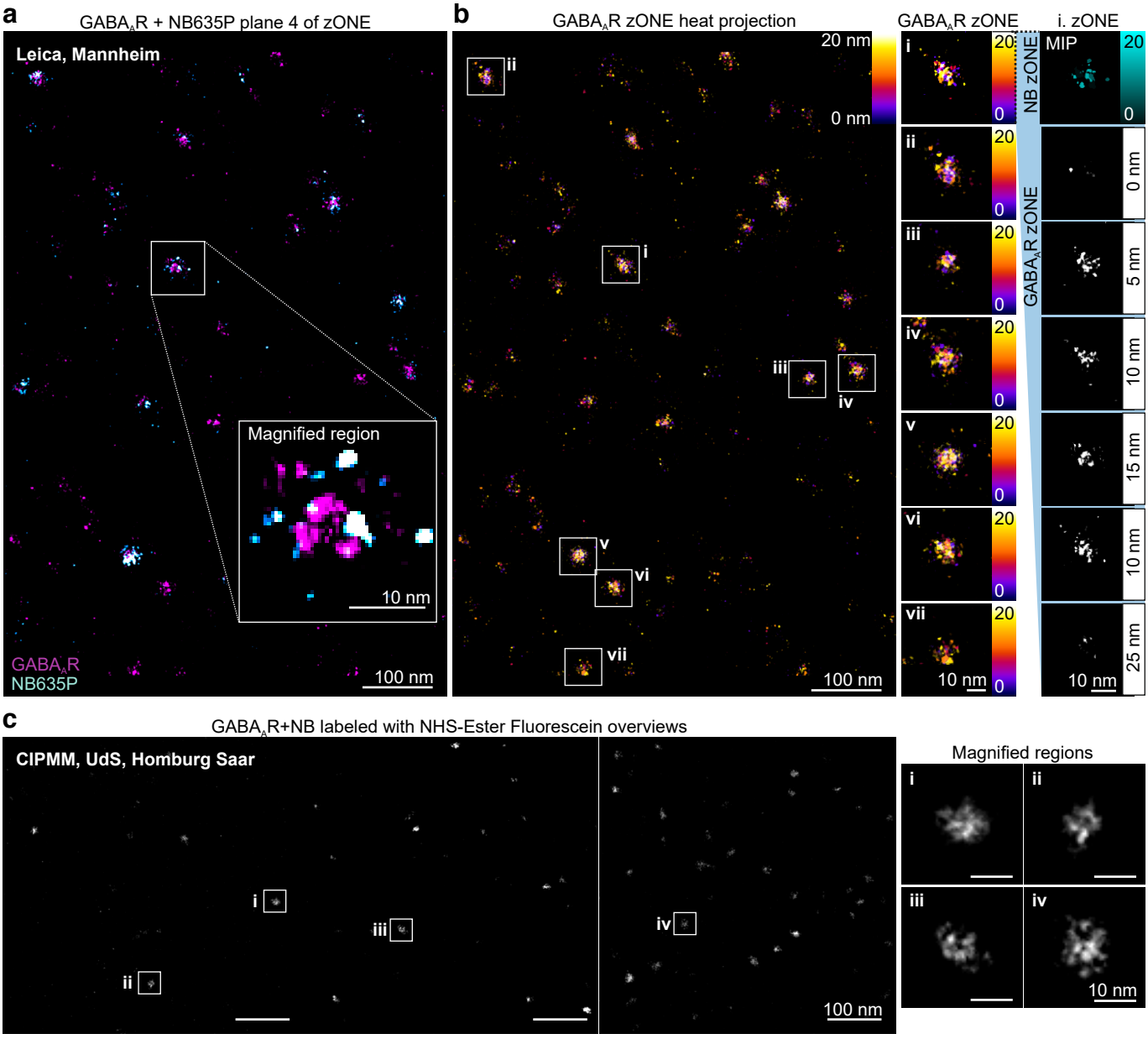

Supplementary Fig. 27. ONE microscopy applied at the confocal headquarters of Leica Microsystems and at the Center for Integrative Physiology and Molecular Medicine (CIPMM) of the Saarland University (UdS). As GABA$_A$R were systematically investigated in this study, we chose them as a reference to evaluate the applicability of ONE technique at different laboratories using different systems. **a**, Using a STELLARIS 8 microscope at Leica Microsystems, we present a snapshot of a plane from a 5-dimension x,y,z,c,t image of GABAAR+NB. **b**, The first panel shows a depth projection of a zONE stack. The second panel shows a set of GABAARs that were magnified. The optical sectioning of the first example is displayed in the rightmost panel. Three independent gels were used for this experiment. **c**, GABA$_A$Rs were also successfully imaged at CIPMM from at least 4 independent gels, Saarland University (UdS), as shown in full 3 full-scale overviews and in their respective magnified regions. Several microscopes were used at the CIPMM, which are presented in the next figure.

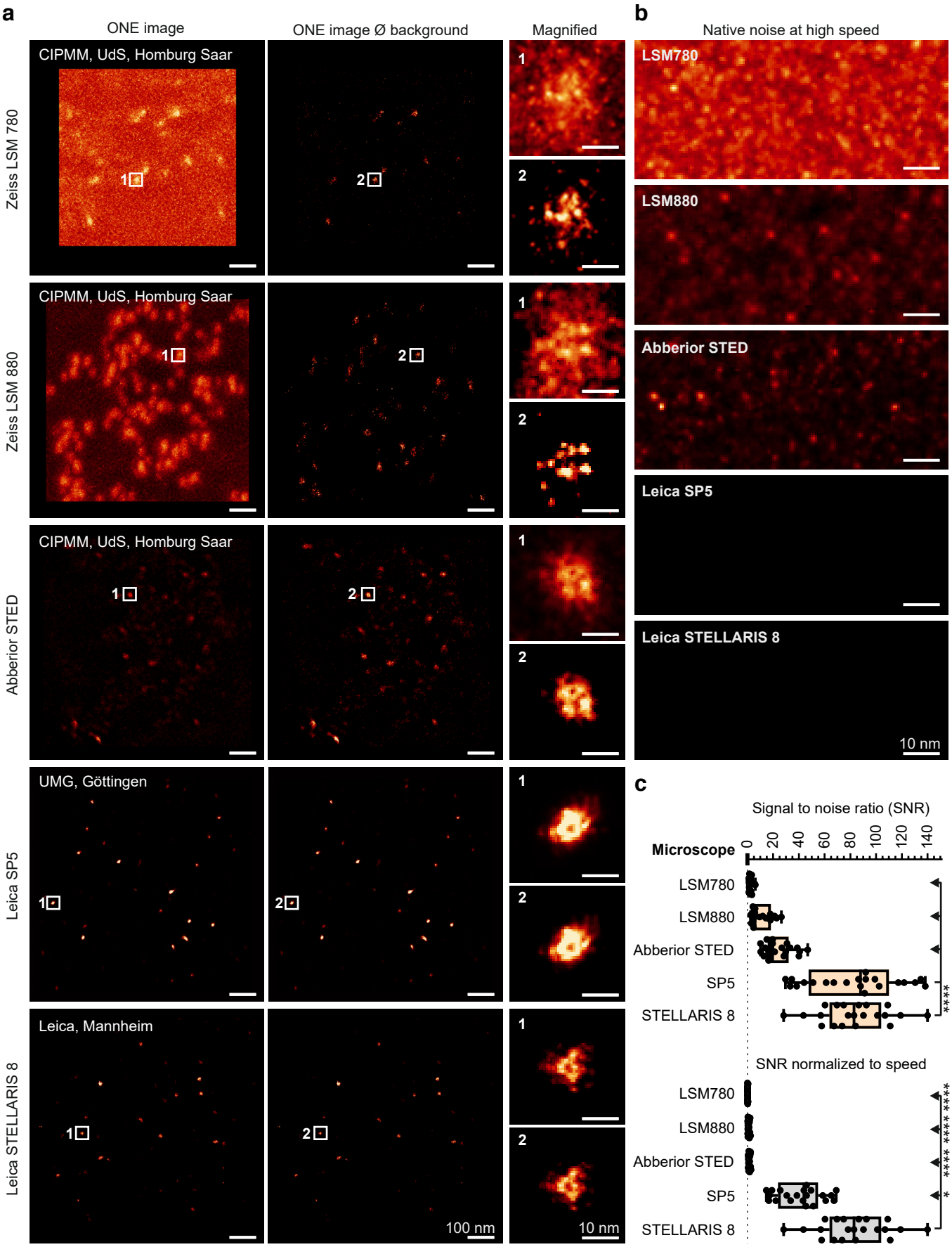

Supplementary Fig. 28. GABAARs could be imaged with different microscopes. Acquisition settings were matched among different systems to the level that each system allowed. The highest achievable speeds were used for each system. This was systematically characterized (data not shown, but can be presented upon request). **a**, Images from the first panel show GABAAR ONE images acquired from different microscopes. As the imaging systems were pushed...

... to their speed limit, background noise was substantially higher on older models. The second panel shows ONE images with background subtraction. The third panel shows a magnified receptor example. **b**, Magnified regions showing the noise readings of each of the used microscopes. **c**, A box plot graph with averages and whiskers displaying the minimum and maximum values showing the achievable signal-to-noise ratio (SNR), as well as the SNR normalized to acquisition speed. Not surprisingly, higher SNRs yielded better ONE images. N = 22, 22, 22, 23, and 23 full region measurement for LSM780, LSM880, Abberior STED, SP5, and STELLAIRS 8, respectively, with each from at least two independent gels. Kruskal-Wallis test was applied. SNR graph *p* values equal to < 0.0001, < 0.0001, 0.0004, and 0.9838 for STELLARIS 8 vs. LSM780, LSM880, Abberior STED and SP5, respectively. SNR normalized to speed graph *p* values equal to < 0.0001, < 0.0001, < 0.0001 and 0.0705 for STELLARIS 8 vs. LSM780, LSM880, Abberior STED and SP5, respectively.

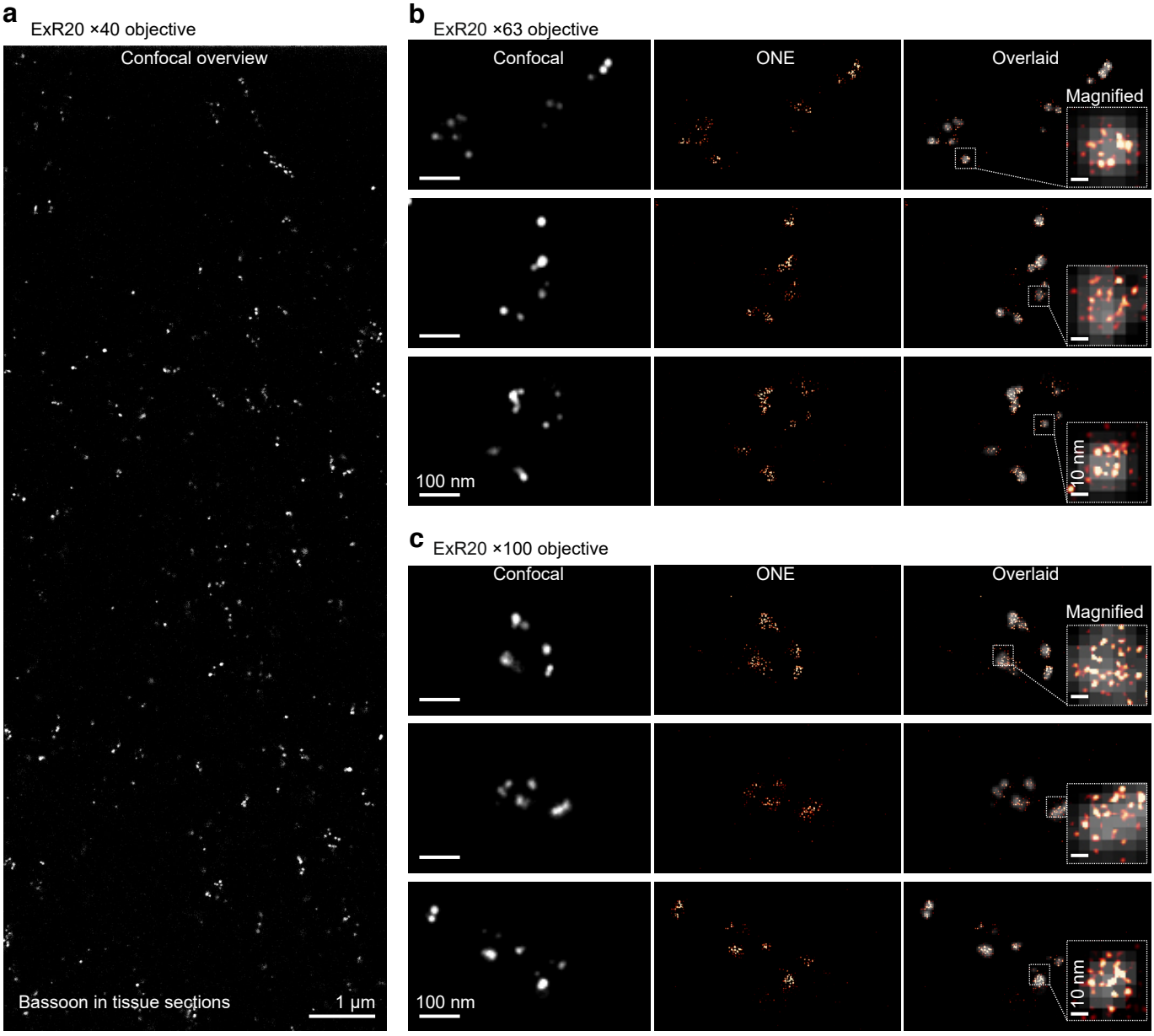

Supplementary Fig. 29. ONE microscopy applied at the MIT, Cambridge, USA. Post-expansion bassoon labeling ONE images from tissue sections that were expanded and then labelled against bassoon following the expansion revealing (ExR) protocol (Sarkar *et al.*, 2022) at the MIT, Cambridge, US. **a**, An ExR20 (X20 expansion) confocal overview imaged with a ×40 objective. **b**, Three different exemplary ONE images of bassoon using a ×63 objective. The first image is a resonant scan MIP of 20 frames, followed by a ONE image, and an overlay with its respective confocal image. The white square indicates the magnified region to the right. **c**, Similar to **b**, but using a ×100 objective. Images were acquired from two independent gels.

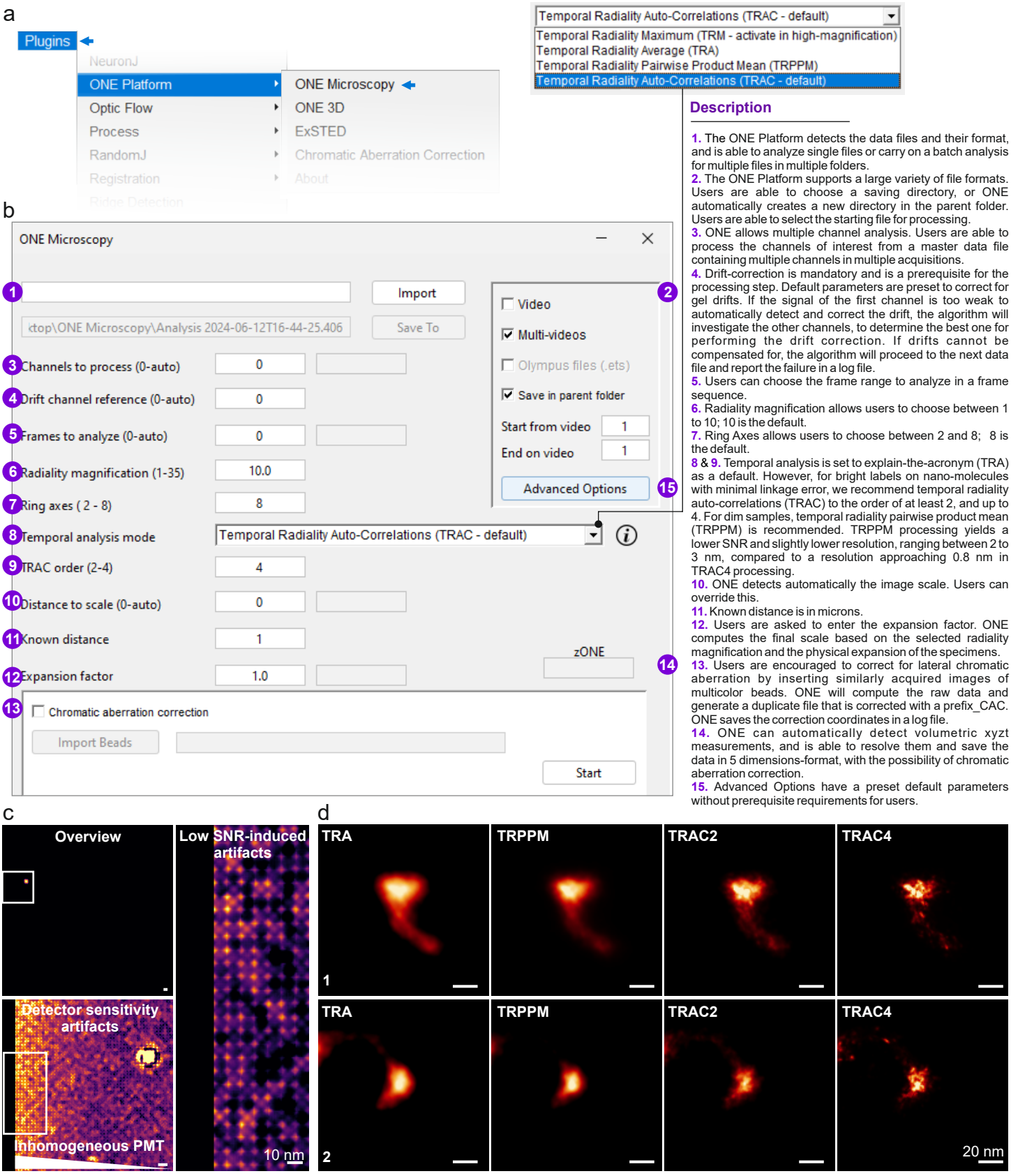

Supplementary Fig. 30. ONE analysis and examples. a & **b**, Several views of the starting interface of the ONE software package. The examples show the intuitive software choices. See also the "Readme/Help" file of the software package. **c**, Examples of different potential artifacts that should be avoided in ONE imaging. **d**, Different potential choices in how to resolve ONE images. We suggest using the temporal radiality pairwise product mean (TRPPM) procedure for dim samples. This reduces the obtainable resolution, but follows much better the potential sample shape. For brightly labelled samples with direct labeling, the temporal radiality auto-correlation (TRAC4) procedure provides the best resolution and SNR, indicating the positions of the individual fluorophores. This is typically observed in the hundreds of acquired ONE images.

Supplementary Tables

Supplementary Table 1. Patient details.

ID	Sex	Age	Diagnosis
1180	m	74	PD
1407	m	82	PD
1698	m	83	PD
1057	f	74	PD
1081	m	69	PD
1100	m	71	PD
1119	f	84	PD
861	f	60	RLS
906	m	73	CBD
1059	m	70	PSP
1223	f	77	PNP
1382	f	75	PNP
1529	m	84	PNP
1606	f	65	PNP

Average ages: 76.7 ± 2.3 years (PD), 72.0 ± 2.9 years (controls); no significant difference (Mann-Whitney Ranksum test).

PD: Parkinson's disease. CDB: Corticobasal degeneration. PNP: Peripheral neuropathy. PSP: Progressive supranuclear palsy. RLS: Restless legs syndrome.

Supplementary Table 2. Image format and analysis technical information.

Figure	Panel	Microscope	Objective	Number of frames	Resonant scanner frequency	Pixel size (nm)	SRRF analysis	Radiality mag.	zONE step size**
1	a	TCS SP5 STED	100× 1.4 NA	2000-3000	8 kHz	0.98	TRAC4	R35*	-
	b	TCS SP5 STED	100× 1.4 NA	1500	8 kHz	0.98	TRAC4	R10	-
2	a	TCS SP5 STED	100× 1.4 NA	1500	8 kHz	0.73	TRPPM	R35	-
	b	TCS SP5 STED & TCS SP8 Lightning	100× 1.4 NA, 63× 1.41 NA	Up to 3000	8 kHz, 12 kHz, & 24 kHz	0.98, 0.48	TRAC4	R35	-
	c	TCS SP5 STED	100× 1.4 NA	2000	8 kHz	0.98	TRAC4	R35	-
	d	TCS SP5 STED	100× 1.4 NA	2000	8 kHz	0.98	TRAC4	R35	-
3	a	TCS SP5 STED	100× 1.4 NA	2000	8 kHz	0.98	TRAC4	R10	-
	b	TCS SP5 STED	100× 1.4 NA	1500-4000	8 kHz	0.98	TRAC4	R35	-
4	a & b	TCS SP5 STED	100× 1.4 NA	1500	8 kHz	0.98	TRPPM, TRAC4	R10	-
Sup. figures	**Panel**	**Microscope**	**Objective**	**Number of frames**	**Resonant scanner frequency**	**Pixel size (nm)**	**SRRF analysis**	**Radiality mag.**	**zONE step size***
1	c	TCS SP5 STED	100× 1.4 NA	2000	8 kHz	0.98	TRAC4	R10	-
	f	TCS SP5 STED	100× 1.4 NA	200-4000	8 kHz	0.98	TRAC4	R10	-
4	a & b	TCS SP5 STED	100× 1.4 NA	2000	8 kHz	0.98	TRAC4, TRA	R10	-
5	a	TCS SP5 STED	100× 1.4 NA	2000	8 kHz	0.98	TRA	R10	-
	b	TCS SP5 STED	100× 1.4 NA	2000	8 kHz	0.48	TRA	R10	-
	c	TCS SP5 STED	100× 1.4 NA	2000	8 kHz	0.98	TRAC4	R10	-
	d	TCS SP5 STED	100× 1.4 NA	2000	8 kHz	0.48	TRAC4	R10	-
6	a & b	TCS SP5 STED	100× 1.4 NA	2000	8 kHz	0.98, 0.48	TRAC4	R10	-
8	a & b	TCS SP5 STED & TCS SP8 Lightning	100× 1.4 NA	Up to 3000	8 kHz	0.98	TRAC4	R10	-
9	d	TCS SP5 STED	100× 1.4 NA	1500	8 kHz	0.73	TRAC4	R10	-
10	a, b, c, g & i	TCS SP5 STED	100× 1.4 NA	Up to 2000	8 kHz	0.73	TRPPM	R10	-
11	a-c	TCS SP5 STED & TCS SP8 Lightning	100× 1.4 NA, 63× 1.41 NA	Up to 3000	8 kHz, 12 kHz, & 24 kHz	0.98, 0.48	TRAC4	R10	-
12	a & c	TCS SP5 STED	100× 1.4 NA	2000	8 kHz	0.98	TRAC4	R10	-
13	a-c	TCS SP5 STED	100× 1.4 NA	2000	8 kHz	0.98	TRAC4	R10	-
14	b, c, f & g	TCS SP5 STED, & TCS SP8 Lightning	100× 1.4 NA	1500-2000	8 kHz, 12 kHz, & 24 kHz	0.98	TRAC4	R10	-
15	b, d, & e	TCS SP5 STED	100× 1.4 NA	1500	8 kHz	0.98, 0.48	TRAC4	R10	-
16	a & c	TCS SP5 STED	100× 1.4 NA	1500	8 kHz	0.98, 0.48	TRAC4	R10	-
17	b, c & g	STELLARIS 8	100× 1.4 NA	2000	12 kHz	0.81	TRAC4	R35	-
18	b & c	TCS SP5 STED	100× 1.4 NA	1500	8 kHz	0.98	TRAC4	R10	-
19	a	TCS SP5 STED	100× 1.4 NA	2000	8 kHz	0.98	TRAC4	R10	-
18	b & c	TCS SP5 STED	100× 1.4 NA	2000	8 kHz	0.98	TRAC4	R10	-
20	a,d & e	TCS SP5 STED	100× 1.4 NA	Up to 4000	8 kHz	0.98, 0.73, 0.36	TRPPM, TRAC4	R10	-
21	a-e	TCS SP5 STED	100× 1.4 NA	Up to 4000	8 kHz	0.73, 0.36, 0.18	TRAC4	R10	-
22	a	TCS SP5 STED	100× 1.4 NA	Up to 4000	8 kHz	0.98, 0.48	TRAC4	R10 & R35	-
24	c	TCS SP5 STED	100× 1.4 NA	1500	8 kHz	0.98, 0.48	TRAC4, TRPPM	R10	-
25	-	TCS SP5 STED	100× 1.4 NA	1500	8 kHz	0.98	TRAC4, TRPPM	R10	-
27	a & b	STELLARIS 8	100× 1.49 NA	Up to 2000	16 kHz	0.73	TRAC4	R10	0.05 µm

	c	Abberior STED	100× 1.4 NA	Up to 2000	1.4 kHz	0.73	TRAC4	R10	-
28	a	LSM780	63× 1.4 NA	Up to 2000	1.2 kHz	0.67	TRAC4	R10	-
	a	LSM880	63× 1.4 NA	Up to 2000	1.2 kHz	0.67	TRAC4	R10	-
	a	Abberior STED	100× 1.4 NA	Up to 2000	1.4 kHz	0.73	TRAC4	R10	-
	a	TCS SP5 STED	100× 1.4 NA	Up to 2000	8 kHz	0.73	TRAC4	R10	-
	a	STELLARIS 8	100× 1.49 NA	Up to 2000	16 kHz	0.73	TRAC4	R10	-
29	b & c	STELLARIS 8	100× 1.4 NA	2000	24 kHz	0.49	TRAC4, TAC2	R10	-
30	d	TCS SP5 STED	100× 1.4 NA	2000	8 kHz	0.98	TRA, TRPPM, TRAC2-4	R10	-

*Referred to in the main text as high radiality magnification ONE images.

** Piezo stage step size (not corrected for expansion factor).

Supplementary Note

Resolution

As presented in the main text, the ONE resolution enhancement relates almost exclusively to the lateral (XY) plane. Resolution along the Z axis depends on the expansion factor of the gel, being equivalent to the axial resolution of the confocal microscope used, divided by the expansion factor. This results in a difference of more than 20-fold between the axial and the lateral resolution, which will have significant effects on the image quality. This situation parallels conventional transmission electron microscopy (TEM), in which the thickness of the specimen limits the axial resolution to a similar 20- to 40-fold above the lateral resolution.

This situation implies that the optimal samples for ONE imaging would have a limited number of objects within the axial imaging volume of 40-60 nm (pre-expansion; volume calculated for a conventional confocal microscope and a 10-15x expansion factor). Denser structures will cause a signal overlap that will confuse the identification of individual structures. The use of purified proteins, which can be diluted to the desired signal density, is an optimal application for ONE microscopy, since the dilution factor avoids the potential issues with axial resolution. We have not encountered any issues relating to the sample density in the lateral (XY) plane: the shape of individual proteins is maintained well, and all measurements we performed provided results within the expected boundaries.

Sample anchoring into the gel

We are currently relying on NHS-ester chemistry to anchor proteins into the gels, using the well-established chemical Acryloyl-X. This molecule reacts to amine groups on lysines and on the N-termini of the proteins in the sample. As lysines make up ~5% of all amino acids in proteins, most proteins should have sufficient anchor points for accurate gel anchoring. The only problem we can envision is the fact that aldehyde fixatives also modify amine groups. If gel anchoring appears faulty in specific samples, possibly due to excessive fixation, we suggest using an epitope retrieval strategy, in which the sample is heated to 95°C in basic buffers (pH 8-9). This strategy should eliminate some of the fixative effects, and should enable accurate gel anchoring. Performing the anchoring in basic buffers, overnight, should also assist with this issue.

Homogenization

The heat-based homogenization is optimal for retaining fluorophores already present in the samples (pre-expansion labeling), since it breaks the proteins, but it does not proceed, in the version we optimized, to the removal of every amino acid. At the same time, it does not rely on the diffusion of an enzyme deep into tissues, so it is optimal for these preparations. In contrast, the proteinase K presumably removes all amino acids that are not anchored into the gel. This approach is optimal for single proteins, since the fluorophore positions become quite precise, being always near the anchor points. However, proteinase K diffusion in thick tissues is poor, and therefore this approach is not suited for tissue slices of over ~10 µm.

SRRF performance

The initial implementation of SRRF resulted in a 50-70 nm resolution[1], leading to the impression that this is the best achievable resolution for this technique, as it is implied by some subsequent works (e.g. [2]). This is not the case, as demonstrated in our work on nanorulers (**Supplementary Fig. 4 & 5**). The name SRRF serves as an umbrella term for a number of different analyses, including the temporal radiality average (**TRA**) and temporal radiality auto-correlation (**TRAC**)[1]. The latter method is a higher-order statistical analysis (following the procedures initially introduced for SOFI[3], whose contrast, accuracy and final resolution are substantially higher than those of the TRA method. The TRA analysis does not consider higher-order temporal correlations, which makes it comfortable to use with limited numbers of frames (*e.g*. 100-300 frames), thus rendering it a method of choice for live-cell SRRF[1, 4]. TRA is heavily dependent on the distance between the fluorophores, and performs best when the different fluorescent objects are separated by more than 70% of the full width at half maximum (FWHM) of the point-spread-function (PSF [2]). This implies that this procedure is not intended to produce a very high resolution, unlike the TRAC analyses. These analyses do produce better resolutions, but require larger numbers of frames for optimal performance, something that does not seem to be clear in the literature; since all SRRF implementations are often performed with as few as 100 frames. Nevertheless, the optimal resolution obtained with TRAC analyses can be pushed towards 20 nm, and maybe even beyond this value, under ideal imaging conditions (**Supplementary Fig. 4 & 5**). We therefore conclude that SRRF should not be considered to be limited to 50-70 nm resolutions, as explained in the Supplementary Notes of the original SRRF publication[1].

As for most other super-resolution approaches, the pixel size limits the resolution to a value of approximately its double[5]. This limitation can be overcome, as indicated in **Supplementary Fig. 4**, by reducing the initial pixel size. This, however, will result in a lower signal-to-noise ratio (SNR), which is an essential parameter for all fluctuation-based analyses. Even when applied to low numbers of frames, SRRF provided excellent images when the signal-to-noise ratio surpassed 10-15[1, 2]. Below these values, SRRF will perform more poorly than many other related methods, as MUSICAL or ESI[2], implying that users should carefully consider the noise levels of their images, as explained in **Supplementary Fig. 6**.

The ONE procedure is designed to alleviate two of the main problems of the TRAC analysis, the fluorophore distance and the SNR. First, the distance between the fluorophores increases in all dimensions, leading to their dilution by the third power of the expansion factor. Second, the SNR increases profoundly (**Supplementary Fig. 3a & b**). This is an important side effect of removing all cellular materials that are not embedded into the gels.

The remaining problem, that of acquiring sufficient frames for optimal performance, depends on 1) sample stability, and 2) fluorophore bleaching. The solutions to these issues come in the form of an improved gel-holding chamber (**Supplementary Fig. 7**) and of rapid resonant scanning, which reduces fluorophore bleaching

(**Supplementary Fig. 3c & d**). The latter effect is known from other super-resolution fields, as STED [6] and is probably due to the fact that rapid scanning lowers the light dose received continuously by every fluorophore, thereby reducing the possibility of excessive excitation and damage.

SRRF radiality magnification

The typical implementation of SRRF relies on splitting the original pixels 10x10, or even 5x5 (in the eSRRF environment). Expansion procedures separate the fluorophores, as discussed in the main text, leading to a potential for higher resolution, which is then limited by these pixel-splitting paradigms. By trial and error, we realized that a radiality magnification of 35 (R35, splitting pixels 35x35) provides substantially more information, and is especially useful for 3D reconstructions (**Fig. 3**). For details of radiality magnification used in each dataset, see Supplementary Table 2. The use of R35 magnification requires more computing time, so that lower values are advised for routine observation of 2D images.

References

1. Gustafsson, N. et al. Fast live-cell conventional fluorophore nanoscopy with ImageJ through super-resolution radial fluctuations. *Nat Commun* **7**, 12471 (2016).
2. Torres-Garcia, E. et al. Extending resolution within a single imaging frame. *Nat Commun* **13**, 7452 (2022).
3. Dertinger, T., Colyer, R., Iyer, G., Weiss, S. & Enderlein, J. Fast, background-free, 3D super-resolution optical fluctuation imaging (SOFI). *Proc Natl Acad Sci U S A* **106**, 22287-22292 (2009).
4. Culley, S., Tosheva, K.L., Matos Pereira, P. & Henriques, R. SRRF: Universal live-cell super-resolution microscopy. *Int J Biochem Cell Biol* **101**, 74-79 (2018).
5. Shannon, C.E. Communication in the Presence of Noise. *Proceedings of the IRE* (1949).
6. Wu, Y. et al. Resonant Scanning with Large Field of View Reduces Photobleaching and Enhances Fluorescence Yield in STED Microscopy. *Sci Rep* **5**, 14766 (2015).